D 2022

U.PORTO
FEUP FACULDADE DE ENGENHARIA
UNIVERSIDADE DO PORTO

Material damping behaviour of critical safety automotive components

Inês Pereira

Thesis submitted for the Doctoral degree in Metallurgical and Materials Engineering at the Faculty of Engineering of the University of Porto

Supervisor
Prof. Luís Filipe Malheiros

Co-Supervisor
Dr. -Ing. Vítor Anjos

Address:

Inês Pereira

FEUP – Faculdade de Engenharia da Universidade do Porto

Departamento de Engenharia Metalúrgica e de Materiais

Rua Dr. Roberto Frias, s/n

4200-465 Porto

Portugal

Copyright © 2022 by Inês Pereira

All rights reserved. No parts of this thesis may be reproduced without written permission from the author.

Acknowledgements

This thesis, developed under the scope of the *Brake Noise* project, was only possible due to the extensive support and collaboration of their partners: *AAPICO Maia S.A.*, *AZTERLAN (BRTA)*, *CENTRE for INNOVATION and TECHNOLOGY N. MAHALINGAM (CITNM)*, *FACULTY of ENGINEERING of the UNIVERSITY of PORTO (FEUP)* and the *UNIVERSITY of AVEIRO (UA)*.

This PhD project has been a long, arduous, but enjoyable experience. Many people have helped me during the journey. I would like to express my sincere gratitude and appreciation to everyone who supported me during its exciting, productive, demanding and frustrating phases. Without their help, I could not have completed my thesis.

First of all, my deepest acknowledgements go to my scientific supervisors, Luís Filipe Malheiros and Vítor Anjos, for all the availability, guidance, and assistance in providing advice to enrich this work, helping me develop as a young professional. It is an honour to work under their supervision.

This project was only possible due to the interest and extensive support of *AAPICO Maia, S.A.* and *AZTERLAN*. Integrating this project and working with distinguished professionals who have given me assistance and knowledge was a privilege. I also sincerely thank Jorge Fesch, Cristina Monteiro, Fernando Vilela, António Pinto, Ana Freitas, Gorka Alonso and Rámon Suarez.

This work would not be possible without the total support and assistance from my employee, *CITNM*. I sincerely thank Inês Frada, João Teixeira and Ana Marques for the long metallurgical and emotional talks.

My thanks also go to *ÁGUEDA SCHOOL of TECHNOLOGY and MANAGEMENT, UNIVERSITY of AVEIRO (ESTGA-UA)*, particularly to my colleagues Miguel Mendonça, Alexandre Pires and Joaquim Sacramento.

My deepest thanks also to Carlos Silva Ribeiro, Manuel Oliveira, José Dias Rodrigues, Rui Moreira, Amílcar Ramalho and Rui Neto for being a great support in guiding me in the scientific fields of this thesis. I would also like to thank the institutions LNEG, CINFU, CEMUP and IMCE for their availability

and support, particularly Fernanda Guimarães, Fernando Barbosa, Carlos Sá, Rui Rocha and Bart Bollen.

I also thank *SinterCast*, *Zanardi Fonderie SpA*, *GF Casting Solutions - Georg Fischer* and *Sonafi* for their interest and collaboration.

I would like to recognize the Department of Metallurgical and Materials Engineering for the assistance and support, particularly Cláudia Lopes, José Ramiro Soares, Cândida Telles and Elsa Sequeiros. A unique and big thank you to my exceptional comrades from room 305.

The friends are the amazing family we choose; mine are proof of that: 8-deitado, Ana, Bubas, Clarissa, Duarte, Gina, Maria, Ricardo, Sofia, Sónia, Tânia and Vera. Thank you all for the support, strength and friendship.

My final and significant grateful mention goes to my family, my parents Adão and Maria, my brothers Ricardo and Pedro, my dear niece Ana and my sister-in-law Eliana. They are my rock and joy through all moments of my life. Last but not least, a big thank you for all the love, support and patience for my David.

Abstract

This thesis is motivated by increased demand for reduction in Noise, Vibration and Harshness induced by the vehicle's braking system. Several solutions might reduce vibration, such as modifying components' design and/or materials selection.

The work explores the damping capacity of spheroidal graphite irons used to produce some components of the braking system. The strategy was to develop spheroidal graphite irons alloyed with Si, Co, and RE elements, among others, influencing the matrix and graphite morphology and aiming to increase the damping capacity without decreasing the tensile and yield strengths.

Chemical and metallographic analysis, damping capacity, hardness, and tensile and elastic properties tests were conducted. Moreover, a step-geometry casting (with five different section thicknesses: 45, 35, 25, 15 and 5 mm) was used to study the influence of the cooling rate on the damping capacity.

The maximum damping capacity improvement was 29%, with tensile strength increasing by 32%. The alloying combinations influenced the cast iron's microstructure by increasing the ferrite's fraction, strengthening it, and slightly decreasing nodularity.

The evaluation of the yield strength/tensile strength ratio showed that specific section thicknesses presented an increase in this ratio and damping capacity without compromising elongation. These results lead to the expectation that these alloyed spheroidal graphite irons might also be a promising lightweight material for some applications since the higher yield strength/tensile strength ratio may allow a decrease in the section thicknesses of the parts, keeping the same level of strength. Moreover, the fully ferritic matrix (*i.e.*, pearlite < 5%), with a uniform hardness, also leads to the expectation of improving machinability.

A multiple linear regression analysis was applied to establish a correlation between the microstructural parameters and damping capacity. The analysis resulted in a statistically significant model, revealing that ferrite's

fraction, convex perimeter and form-III graphite's fraction are the main predictors for the damping capacity of spheroidal graphite irons. The model shows that increasing these predictors will improve the damping capacity; ferrite's fraction significantly influences damping capacity variation.

The industrial validation of the most promising alloying combination displayed an improvement of 54% and 84% of the damping capacity, respectively, to the standard ferritic and pearlitic SGI produced by *AAPICO*. The castings presented a strengthened ferritic matrix with 70% nodularity, a tensile strength of 534 MPa, a yield strength of 432 MPa and an elongation of 8.1%, with an improved damping capacity.

Damping capacity improvement rests on the balance between the graphite nodularity and the fraction of strengthened ferrite to reach the required mechanical properties for the parts.

This thesis may provide information for cast iron foundries longing to improve various materials' properties through chemical composition manipulation in multiple applications.

Keywords: NVH – Noise, Vibration and Harshness; SGI – Spheroidal Graphite Iron; High alloyed; Damping capacity.

Resumo

Esta tese foi motivada pela pressão exercida pelo setor automóvel em reduzir o ruído, vibração e aspereza induzidos pelo sistema de travagem dos veículos. Poderão ser adotadas diferentes soluções com vista a reduzir a vibração, tais como a modificação dos materiais ou o *design* dos componentes.

Este trabalho explora a capacidade de amortecimento de ferros fundidos nodulares utilizados na produção de componentes do sistema de travagem dos automóveis. A estratégia assentou no desenvolvimento de ferros fundidos nodulares ligados ao Si, Co e TR, entre outros, que influenciassem o tipo de matriz e a morfologia da grafite de forma a induzir o aumento da capacidade de amortecimento sem um decréscimo acentuado da resistência à tração.

Foram efetuadas análises químicas e microestruturais, assim como ensaios para determinação da capacidade de amortecimento e outras propriedades mecânicas. Recorreu-se a corpos de prova em escada (com secções de espessura distinta: 45, 35, 25, 15 e 5 mm) para avaliar o impacto da velocidade de arrefecimento sobre a microestrutura e, consequentemente, sobre a capacidade de amortecimento e outras propriedades mecânicas.

Os resultados obtidos apontam para uma melhoria máxima de 29% em termos de capacidade de amortecimento, com um aumento de 32% da resistência à tração. Os elementos de liga utilizados induziram um aumento da fração de ferrite e o seu endurecimento, bem como uma ligeira diminuição da nodularidade da grafite.

A avaliação da relação entre a tensão limite convencional de proporcionalidade a 0,2% e a tensão de rotura mostra que, para secções com espessuras específicas, se regista um aumento desse rácio assim como da capacidade de amortecimento, sem comprometer o alongamento. Estes resultados instigam a expectativa de que estes materiais podem permitir o recurso a estruturas mais leves uma vez que um aumento desse rácio poderá permitir uma diminuição das suas espessuras, para um mesmo nível de resistência à tração. Além disso, uma matriz totalmente ferrítica

(*i.e.*, perlite < 5%), de dureza uniforme, afigura-se promissora em termos de maquinabilidade dos componentes dos veículos automóveis.

Recorreu-se a uma análise de regressão linear múltipla para estabelecer uma relação entre a microestrutura de ferros fundidos nodulares e a sua capacidade de amortecimento. A análise resultou num modelo estatisticamente representativo, revelando que a fração de ferrite, o "perímetro convexo" e a fração de grafite tipo III são os principais preditores da capacidade de amortecimento. O modelo mostra que o aumento desses preditores promove uma melhoria da capacidade de amortecimento; a fração de ferrite aparenta ter o maior impacto sobre a variação da capacidade de amortecimento.

A validação, a nível industrial, do ferro fundido nodular ligado mais promissor revelou um aumento da capacidade de amortecimento de 54% e 84% em relação, respetivamente, aos ferros fundidos ferríticos e perlíticos *standard* atualmente utilizados pela *AAPICO*. As peças produzidas apresentavam uma matriz ferrítica endurecida por solução sólida, grafite com uma nodularidade de 70%, uma tensão de rotura de 534 MPa, uma tensão limite convencional de proporcionalidade a 0,2% de 432 MPa e um alongamento de 8,1%.

A melhoria da capacidade de amortecimento de ferros fundidos nodulares assenta no equilíbrio entre a nodularidade da grafite e o endurecimento da matriz ferrítica de forma a atingir as propriedades mecânicas almejadas.

Os resultados deste trabalho poderão constituir informações relevantes para as fundições de ferro fundido que pretendam promover uma melhoria das propriedades dos seus produtos por manipulação da composição química para uma vasta gama de aplicações.

Palavras-chave: NVH – Ruído, Vibração e Aspereza; SGI – Ferro fundido nodular; Ferro fundido nodular ligado; Capacidade de amortecimento.

Table of Contents

Abstract i

Resumo iii

Table of Contents v

List of Abbreviations ix

List of Figures Caption xi

List of Tables Caption xv

1. Introduction
1.1. Motivation and Strategy 1
1.2. Research Objectives 3

2. Literature Review
2.1. Noise, Vibration and Harshness Control 5
2.2. Damping 7
2.2.1. General phenomena 7
2.2.2. Identification methods 8
2.2.2.1. Impulse Excitation Technique 9
2.3. Cast irons' characterization 14
2.3.1. Spheroidal graphite irons 16
2.3.1.1. Production process 18
2.3.1.1.1. Base iron melt preparation 18
2.3.1.1.2. Nodularizing treatment 18
2.3.1.1.3. Inoculation treatment 19
2.3.1.1.4. Process control 19
2.3.1.2. Solidification mechanisms 20
2.3.1.3. Factors influencing the microstructure of as-cast SGI 22
2.3.1.3.1. Chemical composition 23
2.3.1.3.2. Cooling rate 27
2.3.1.3.3. Inoculation 28
2.3.2. Mechanical properties 30
2.3.2.1. Damping capacity 35
2.3.2.1.1. Impact of the graphite 37
2.3.2.1.2. Impact of the matrix 39
2.4. Research methodology 40

3. Experimental Methodology
3.1. Materials' characterization 41
3.1.1. Strategic approach 41
3.1.2. Development of the castings for the experiments 43
3.1.3. Melting procedure 45
3.1.3.1. First approach experiments 45
3.1.3.2. Fine approach experiments 48
3.1.4. Experimental procedures 51
3.1.4.1. Porosity control and cutting of castings 51
3.1.4.2. Microstructural analysis 51
3.1.4.3. Tensile tests 54
3.1.4.4. Hardness tests 54
3.1.4.5. Impulse Excitation Technique tests 55
3.1.4.6. Results dispersion 57
3.1.4.6.1. Tensile tests 57
3.1.4.6.2. Hardness tests 58
3.1.4.6.3. Damping capacity tests 59
3.1.4.7. Multiple linear regression analysis 61

4. Experimental Results
4.1. Damping capacity of different standard cast alloys 63
4.2. Alloyed spheroidal graphite irons 64
4.2.1. First approach experiments 64
4.2.1.1. Evaluation of the first approach experiments 68
4.2.1.1.1. High Si-alloyed SGI 70
4.2.1.1.2. Co-alloyed SGI 78
4.2.1.1.3. RE-alloyed SGI 88
4.2.1.1.4. High Si + RE-alloyed SGI 95
4.2.2. Fine approach experiments 105
4.2.2.1. Evaluation of the fine approach experiments 108
4.2.2.2. High Si-alloyed SGI combinations 109

5. Discussion of Results
5.1. Overall analysis 115
5.2. Model for estimating the SGI damping capacity 119
5.3. The most promising alloyed SGIs tested 124
5.4. Validation of the experiments at the industrial plant 127

6. Conclusions and Future Works 131
6.1. Future works perspectives 133

References 135

Annexe A: Determination of the casting modulus 145

Annexe B: Complementary results 147
B.1. First Approach Experiments 147
B.1.1. High Si-alloyed SGI 147
B.1.2. Co-alloyed SGI 148
B.1.3. RE-alloyed SGI 149
B.1.4. High Si + RE-alloyed SGI combinations 150
B.1.5. Cu-alloyed SGI 151
B.1.6. Mo-alloyed SGI 153
B.1.7. Al (x1)-alloyed SGI 157
B.2. Fine Approach Experiments 159
B.2.1. Base 1 SGI 159
B.2.2. High Si-alloyed SGI combinations 161
B.2.3. Co + Ce-alloyed SGI 162
B.2.4. Al (x5)-alloyed SGI 166

Annexe C: Model proposed for estimating the damping capacity 169

List of Abbreviations

ADI	Austempered Ductile Iron
C.E.	Carbon Equivalent
CGI	Compacted Graphite Iron
CV	Coefficient of Variation
EDS	Energy Dispersive X-ray Spectroscopy
EPMA	Electron Probe Micro-Analyser
FGI	Flake Graphite Iron
IET	Impulse Excitation Technique
LOM	Light Optical Microscopy
NVH	Noise, Vibration, and Harshness
OEMs	Original Equipment Manufacturers
RFDA	Resonant Frequency and Damping Analyser
SEM	Scanning Electron Microscopy
SGI	Spheroidal Graphite Iron
SPSS	Statistical Package for the Social Sciences software
ST	Section Thickness
TR	Terras Raras
TS	Tensile Strength
VIF	Variance Inflation Factor
WDS	Wavelength Dispersive X-ray Spectroscopy
YS	Yield Strength

List of Figures Caption

Figure 1 - 1. Disc brake assembly; adapted from [13]. 2
Figure 1 - 2. General schematic representation of the investigation paths of the thesis. 4

Figure 2 - 1. Sub-categories of the brake noise; adapted from [15]. 6
Figure 2 - 2. Sinusoidal damped vibration; adapted from [42]. 10
Figure 2 - 3. a) Amplitude of the vibration of the sample *vs.* time. b) A spectrum of the resonance frequencies obtained by using fast Fourier transform from the data shown in a); adapted from [48]. 11
Figure 2 - 4. Positioning of rectangular bars to be tested on the supports for: a) flexural vibration mode, and b) torsional vibration mode; adapted from [31]. 12
Figure 2 - 5. SEM micrographs of deeply etched cast irons with different graphite morphologies: a) flake, b) compacted, c) spheroidal; adapted from [51].....15
Figure 2 - 6. Graphite morphologies in cast irons, according to the EN ISO 945-1: 2008 standard [52]. 16
Figure 2 - 7. SGI microstructures of varying degrees of nodularity: a) 99%, b) 80%, c) 50%. All unetched samples [50]. 17
Figure 2 - 8. SGI microstructures, etched with Nital, with: a) fully ferritic matrix, b) pearlitic-ferritic matrix [54] 17
Figure 2 - 9. The Fe-C phase diagram [55].....21
Figure 2 - 10. Nodular graphite particles count in SGI inoculated with standard foundry grade FeSi (75% Si), added to the ladle or the metal stream, *vs.* section thickness of the casting [50]. 29
Figure 2 - 11. Nodule count *vs.* the Si (%) added as inoculant (addition in the ladle) [50]. 29
Figure 2 - 12. Relationship between the minimum specified values for the tensile strength and elongation in the range of values covered by the ISO, ASTM, and SAE standards [50]. 32
Figure 2 - 13. Tensile strength *vs.* pearlite's fraction of SGI with different nodularity [50, 78]. 33
Figure 2 - 14. SGI tensile and yield strengths *vs.* its nodularity [50]. 34
Figure 2 - 15. Damping capacity *vs.* the tensile strength of cast irons [98]. ..36
Figure 2 - 16. Effect of Al content on the damping capacity of cast irons [73]. 38

Figure 3 - 1. Schematic representation of the three major stages of the experimental approach for the materials characterization. 41
Figure 3 - 2. Dimensions (in mm) of the step-casting. 44

Figure 3 - 3. Step-casting's model and the respective gating and feeding system 44
Figure 3 - 4. Image of a step-casting from the first approach experiments with 45, 35, 25, 15 and 5 mm section thicknesses. 46
Figure 3 - 5. Flowchart relative to the first approach experiments[3]. 47
Figure 3 - 6. Image of a casting from the fine approach experiments with 35 and 15 mm section thicknesses. 49
Figure 3 - 7. Flowchart relative to the fine approach experiments[4]. 50
Figure 3 - 8. Image of one of the step-casting produced, indicating the zones from where the different samples have been removed for: tensile tests (in orange), microstructural analysis, damping and hardness tests (in blue). 51
Figure 3 - 9. Example of estimating the convex perimeter of a graphite particle [121]. 53
Figure 3 - 10. Estimating the length of a graphite particle [121]. 53
Figure 3 - 11. Resonant Frequency and Damping Analyser (RFDA) equipment. 55

Figure 4 - 1. Variation of the damping capacity of different cast alloys relative to the ferritic and pearlitic SGIs produced by *AAPICO*. 64
Figure 4 - 2. LOM micrographs of the Base 0 SGI, for the first approach experiments, for different section thicknesses. 67
Figure 4 - 3. Base methodology for categorizing the results of the mechanical properties of all the SGI castings from the first approach experiments. 69
Figure 4 - 4. LOM micrographs of the High Si-alloyed SGI, for different section thicknesses. 72
Figure 4 - 5. Damping capacity of the High Si-alloyed and Base 0 SGIs *vs.* the section thicknesses of the step-castings. 73
Figure 4 - 6. Ultimate tensile strength of the High Si-alloyed and Base 0 SGIs *vs.* the section thicknesses of the step-castings. 74
Figure 4 - 7. 0.2% offset yield strength of the High Si-alloyed and Base 0 SGIs *vs.* the section thicknesses of the step-castings. 75
Figure 4 - 8. Elongation of the High Si-alloyed and Base 0 SGIs *vs.* the section thicknesses of the step-castings. 76
Figure 4 - 9. Young's modulus of the High Si-alloyed and Base 0 SGIs *vs.* the section thicknesses of the step-castings. 77
Figure 4 - 10. LOM micrographs of the Co (x1)-alloyed SGI, for different section thicknesses. 79
Figure 4 - 11. LOM micrographs of the Co (x2)-alloyed SGI, for different section thicknesses. 80
Figure 4 - 12. EPMA maps for C, Si and Co for the Co (x2)-alloyed SGI, for the 45 mm section thickness. 82
Figure 4 - 13. Damping capacity of the Co-alloyed and Base 0 SGIs *vs.* the section thicknesses of the step-castings. 83

Figure 4 - 14. Ultimate tensile strength of the Co-alloyed and Base 0 SGIs *vs.* the section thicknesses of the step-castings. 84
Figure 4 - 15. 0.2% offset yield strength of the Co-alloyed and Base 0 SGIs *vs.* the section thicknesses of the step-castings. 85
Figure 4 - 16. Elongation of the Co-alloyed and Base 0 SGIs *vs.* the section thicknesses of the step-castings. 86
Figure 4 - 17. Young's modulus of the Co-alloyed and Base 0 SGIs *vs.* the section thicknesses of the step-castings. 87
Figure 4 - 18. LOM micrographs of the RE (x1)-alloyed SGI, for different section thicknesses 89
Figure 4 - 19. Damping capacity of the RE (x1)-alloyed and Base 0 SGIs *vs.* the section thicknesses of the step-castings. 91
Figure 4 - 20. Ultimate tensile strength of the RE (x1)-alloyed and Base 0 SGIs *vs.* the section thicknesses of the step-castings. 92
Figure 4 - 21. 0.2% offset yield strength of the RE (x1)-alloyed and Base 0 SGIs *vs.* the section thicknesses of the step-castings. 92
Figure 4 - 22. Elongation of the RE (x1)-alloyed and Base 0 SGIs *vs.* the section thicknesses of the step-castings. 93
Figure 4 - 23. Young's modulus of the RE (x1)-alloyed and Base 0 SGIs *vs.* the section thicknesses of the step-castings. 94
Figure 4 - 24. LOM micrographs of the High Si + RE (x0.5)-alloyed SGI, for different section thicknesses. 96
Figure 4 - 25. LOM micrographs of the High Si + RE (x1)-alloyed SGI, for different section 97
Figure 4 - 26. Damping capacity of the High Si + RE-alloyed and Base 0 SGIs *vs.* the section thicknesses of the step-castings. 99
Figure 4 - 27. Ultimate tensile strength of the High Si + RE-alloyed and Base 0 SGIs *vs.* the section thicknesses of the step-castings. 100
Figure 4 - 28. 0.2% offset yield strength of the High Si + RE-alloyed and Base 0 SGIs *vs.* the section thicknesses of the step-castings. 101
Figure 4 - 29. Elongation of the High Si + RE-alloyed and Base 0 SGIs *vs.* the section thicknesses of the step-castings. 102
Figure 4 - 30. Young's modulus of the High Si + RE-alloyed and Base 0 SGIs *vs.* the section thicknesses of the step-castings. 103
Figure 4 - 31. LOM micrographs of the Base 2 SGI, for the 35 mm section thickness. 107
Figure 4 - 32. Damping capacity *vs.* the YS/TS ratio for the samples with 35 mm section 109
Figure 4 - 33. LOM micrographs of the High Si-alloyed SGI, for the sample with 35 mm section thickness. 110
Figure 4 - 34. LOM micrographs of the High Si + Ce (x0.5)-alloyed SGI, for the sample with 35 mm section thickness. 110

Figure 4 - 35. LOM micrographs of the High Si + Ce (x0.5) + Co-alloyed SGI, for the sample with 35 mm section thickness. 110

Figure 5 - 1. Residuals' histogram. 122
Figure 5 - 2. Plot of the predicted probability (P-P) for residuals.....122
Figure 5 - 3. Residuals' scattering. 123
Figure 5 - 4. Damping capacity *vs.* the YS/TS ratio for the samples with 35 mm section thickness from the most promising alloyed SGIs. 125
Figure 5 - 5. Variation of the damping capacity of the most promising alloying combinations relative to the ferritic and pearlitic SGIs produced by *AAPICO*. 126
Figure 5 - 6. LOM micrographs of the High Si-alloyed SGI, with degenerated graphite.....128

Figure A. 1. Images of the simulation of the solidification of the step-casting by the QuikCAST software. 146

Figure B. 1. LOM micrographs of the Cu-alloyed SGI, for different section thicknesses. 152
Figure B. 2. LOM micrographs of the Mo (x1)-alloyed SGI, for different section thicknesses. 154
Figure B. 3. LOM micrographs of the Mo (x2)-alloyed SGI, for different section thicknesses. 156
Figure B. 4. LOM micrographs of the Al (x1)-alloyed SGI, for the 45 mm section thickness. 158
Figure B. 5. LOM micrographs of the Base 1 SGI, for the 35 and 15 mm section thicknesses. 160
Figure B. 6. LOM micrographs of the Co + Ce (x0.5)-alloyed SGI, for the 35 and 15 mm section thicknesses. 163
Figure B. 7. LOM micrographs of the Co + Ce (x1)-alloyed SGI, for the 15 and 35 mm section thicknesses. 165
Figure B. 8. LOM micrographs of the Al (x5)-alloyed SGI, for the 15 mm section thickness. 166
Figure B. 9. a) SEM micrograph of the Al (x5)-alloyed SGI, for the 15 mm section thickness; b) and c) X-ray spectra of Z1 and Z2 zones, respectively; d) EDS semi-quantitative analysis of Z1 and Z2 zones. 167

Figure C. 1. Residuals' histogram. 169
Figure C. 2. Plot of the predicted probability (P-P) for residuals. 170
Figure C. 3. Residuals' scattering. 170

List of Tables Caption

Table 2 - 1. Mechanical properties measured on test pieces machined from cast samples of ferritic to pearlitic grades [58] 31
Table 2 - 2. Mechanical properties measured on test pieces machined from cast samples of solid solution strengthened ferritic grades [58] 32
Table 2 - 3. Damping capacity of cast irons at room temperature; adapted from [99] and presented in [30] 37
Table 2 - 4. List of the alloying elements selected for the preliminary trials .. 40

Table 3 - 1. Step-casting thicknesses and alloying elements tested in the first and fine approaches experiments performed on alloyed SGI 43
Table 3 - 2. Procedures for the metallographic preparation of the samples .. 52
Table 3 - 3. Methodology for the Impulse Excitation Technique tests 56
Table 3 - 4. Coefficient of variation for each of the mechanical properties obtained from the tensile tests 57
Table 3 - 5. Results from the tensile tests for two samples with different geometries 57
Table 3 - 6. Coefficient of variation calculated for the hardness tests 58
Table 3 - 7. Coefficient of variation of the results for the damping capacity tests 59
Table 3 - 8. Coefficient of variation of the results for the fundamental flexural frequency 60
Table 3 - 9. Coefficient of variation of the results for the Poisson's ratio 60

Table 4 - 1. Chemical composition of the SGI melts produced for the first approach experiments 66
Table 4 - 2. Results of the tests performed on the Base 0 SGI samples for the first approach experiments 68
Table 4 - 3. Comparative evaluation of the mechanical properties of the SGI castings from the first approach experiments 70
Table 4 - 4. Microstructural parameters of the High Si-alloyed SGI, for different section thicknesses 73
Table 4 - 5. Variation of the damping capacity of the High Si-alloyed SGI 73
Table 4 - 6. Variation of the ultimate tensile strength of the High Si-alloyed SGI 74
Table 4 - 7. Variation of the 0.2% offset yield strength of the High Si-alloyed SGI 75
Table 4 - 8. Variation of the elongation of the High Si-alloyed SGI 76
Table 4 - 9. Variation of the Young's modulus of the High Si-alloyed SGI 77
Table 4 - 10. Variation of the hardness of the High Si-alloyed SGI 77

Table 4 - 11. Microstructural parameters of the Co (x1)-alloyed SGI, for different section thicknesses.....81
Table 4 - 12. Microstructural parameters of the Co (x2)-alloyed SGI, for different section thicknesses.....81
Table 4 - 13. Variation of the damping capacity of the Co-alloyed SGIs.....83
Table 4 - 14. Variation of the ultimate tensile strength of the Co-alloyed SGIs 84
Table 4 - 15. Variation of the 0.2% offset yield strength of the Co-alloyed SGIs 85
Table 4 - 16. Variation of the elongation of the Co-alloyed SGIs.....86
Table 4 - 17. Variation of the Young's modulus of the Co-alloyed SGIs.....87
Table 4 - 18. Variation of the hardness of the Co-alloyed SGIs.....88
Table 4 - 19. Microstructural parameters of the RE (x1)-alloyed SGI, for different section thicknesses.....90
Table 4 - 20. Variation of the damping capacity of the RE (x1)-alloyed SGI.91
Table 4 - 21. Variation of the ultimate tensile strength of the RE (x1)-alloyed SGI 92
Table 4 - 22. Variation of the 0.2% offset yield strength of the RE (x1)-alloyed SGI 93
Table 4 - 23. Variation of the elongation of the RE (x1)-alloyed SGI 93
Table 4 - 24**.** Variation of the Young's modulus of the RE (x1)-alloyed SGI .94
Table 4 - 25. Variation of the hardness of the RE (x1)-alloyed SGI 95
Table 4 - 26. Microstructural parameters of the High Si + RE (x0.5)-alloyed SGI, for different section thicknesses 98
Table 4 - 27. Microstructural parameters of the High Si + RE (x1)-alloyed SGI, for different section thicknesses.....98
Table 4 - 28. Variation of the damping capacity of the High Si + RE-alloyed SGIs.....99
Table 4 - 29. Variation of the ultimate tensile strength of the High Si + RE-alloyed SGIs 100
Table 4 - 30. Variation of the 0.2% offset yield strength of the High Si + RE-alloyed SGIs 101
Table 4 - 31. Variation of the elongation of the High Si + RE-alloyed SGIs 102
Table 4 - 32. Variation of the Young's modulus of the High Si + RE-alloyed SGIs.....103
Table 4 - 33. Variation of the hardness of the High Si + RE-alloyed SGIs, for different section thicknesses.....104
Table 4 - 34. Chemical composition of the SGI melts produced for the fine approach experiments 106
Table 4 - 35. Results of the tests performed on the Base 2 SGI sample for the fine approach experiments 107
Table 4 - 36. Comparative evaluation of the mechanical properties of the SGI castings from the fine approach experiments 108

Table 4 - 37. Microstructural parameters of the different alloyed SGIs of the fine approach trials, for the 35 mm section thickness 111
Table 4 - 38. Variation of the damping capacity of the alloyed SGIs from the fine approach experiments 112
Table 4 - 39. Variation of the ultimate tensile strength of the alloyed SGIs from the fine approach experiments 112
Table 4 - 40. Variation of the 0.2% offset yield strength of the alloyed SGIs from the fine approach experiments 113
Table 4 - 41. Variation of the elongation of the alloyed SGIs from the fine approach experiments 113
Table 4 - 42. Variation of the Young's modulus of the alloyed SGIs from the fine approach experiments 114
Table 4 - 43. Variation of the hardness of the alloyed SGIs from the fine approach experiments 114

Table 5 - 1. Analysis of the assumptions of the multiple linear regression..121
Table 5 - 2. Results of the industrial validation of the High Si SGI with degenerated graphite.....129

Table A. 1. Parameters used for the simulation of the solidification of the step-casting by the QuikCAST software 145

Table B. 1. Fundamental flexural frequency and elastic properties of the High Si-alloyed SGI, for different section thicknesses.....147
Table B. 2. Fundamental flexural frequency and elastic properties of the Co (x1)-alloyed SGI, for different section thicknesses.....148
Table B. 3. Fundamental flexural frequency and elastic properties of the Co (x2)-alloyed SGI, for different section thicknesses.....148
Table B. 4. Fundamental flexural frequency and elastic properties of the RE (x1)-alloyed SGI, for different section thicknesses.....149
Table B. 5. Fundamental flexural frequency and elastic properties of the High Si + RE (x0.5)-alloyed SGI, for different section thicknesses.....150
Table B. 6. Fundamental flexural frequency and elastic properties of the High Si + RE (x1)-alloyed SGI, for different section thicknesses.....150
Table B. 7. Results of tests performed on the Cu-alloyed SGI samples from the first approach experiments.....151
Table B. 8. Results of tests performed on Mo(x1)-alloyed SGI samples from the first approach experiments.....153
Table B. 9**.** Results of tests performed on the Mo (x2)-alloyed SGI samples from the first approach experiments 155
Table B. 10. Results of tests performed on the Al (x1)-alloyed SGI sample from the first approach experiments.....157

Table B. 11. Results of the tests performed on the Base 1 SGI samples from the fine approach experiments 159
Table B. 12. Fundamental flexural frequency and elastic properties of the High Si-alloyed SGI combinations from the fine approach experiments.....161
Table B. 13. Results of the tests performed on the Co + Ce (x0.5)-alloyed SGI samples from the fine approach experiments 162
Table B. 14. Results of the tests performed on the Co + Ce (x1)-alloyed SGI samples from the fine approach experiments 164
Table B. 15. Results of the tests performed on the Al (x5)-alloyed SGI sample from the fine approach experiments 166

Table C. 1. Analysis of the multiple linear regression assumptions 169

1. Introduction

Chapter 1 outlines the motivation and strategy for this thesis and the potential impact of this research on the industry.

1.1. Motivation and Strategy

In recent years, noise emissions have been one of the environmental pollution issues. New demands from consumers and environmental authorities have led to increased burdensome regulations concerning noise emissions, thus originating a continuous search and, therefore, interest in its reduction [1-3].

Considering the noise emission pollution originated from vehicles, one of its sources is the braking system. With the improvement of the vehicle's comfort and soundproofing, the brake noise contribution as a noise source has increased customers' concerns, making them believe that a given braking system presents a defect, although, in all other issues, the component is fulfilling its assigned functions. The brake noise constitutes one of the highest incidences of customers' complaints, as dissatisfaction, and warranty costs [4-6].

During the last few years, the automotive industry has also been aiming to decrease vehicles' weight to reduce fuel consumption and CO_2 emissions without, at the very least, compromising the vehicle's performance. However, this may create conflicting requirements since lightweight structures can be more susceptible to vibration and thus emit higher levels of noise pollution [3, 7].

Noise prevision remains an impasse since not all the mechanisms and interactions are known due to the highly effusive, transient, and often non-repeatable nature. Such features result from the complex nature of the interaction of the braking system components and the interdependence of parameters, such as operating and contact conditions, and material properties, among others [4, 5, 8-10].

In a communication presented at an international congress [11], *CONTINENTAL Teves AG* ranked the zero noise of the braking system as one of the primary five goals to be achieved by OEMs (Original Equipment Manufacturers) on braking systems. Hence, to investigate and understand the Noise, Vibration, and Harshness (NVH) problems of the braking system, the *Brake Noise* project was launched, involving the following partners: *AAPICO Maia S.A., AZTERLAN (BRTA)*, *CENTRE for INNOVATION and TECHNOLOGY N. MAHALINGAM*, *FACULTY of ENGINEERING of the UNIVERSITY of PORTO* and the *UNIVERSITY of AVEIRO*. This thesis was developed under the scope of this project.

High damping materials are used for vibration and noise reduction [12]. Hence, the thesis's strategy was to block or reduce the noise originating from brakes focusing on the effect, not the vibration source. It should be stressed that this thesis has not considered the flake graphite iron used in producing the brake discs (the source of the vibration).

This strategy is accomplished by influencing how the brake disc vibration is dissipated through the other brake's components, more precisely, the anchor and the calliper (Figure 1 - 1). The research focused on the damping potential of spheroidal graphite iron used to produce these two components of the braking system.

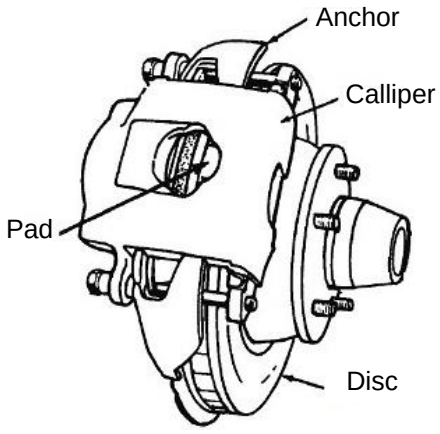


Figure 1 - 1. Disc brake assembly; adapted from [13].

1.2. Research Objectives

The research involved studying the damping capacity of SGI used to produce critical safety components, anchor and calliper, by *AAPICO*. Essentially, it explored how the damping capacity of cast iron can be enhanced without compromising strength requirements.

The first objective was to verify the influence of adding different alloying elements on the damping capacity and the impact of the cooling rate. Secondly, it aimed to forecast the SGI damping capacity through a fitting model that correlates with its microstructure. Moreover, other mechanical properties of the materials, such as tensile strength, hardness and elasticity, were also evaluated.

This thesis aims to contribute to scientific knowledge and provide information for cast iron foundries in a wide range of applications, which are longing to improve several materials' properties through chemical composition manipulation.

Figure 1 - 2 shows a general schematic representation of the investigation focus.

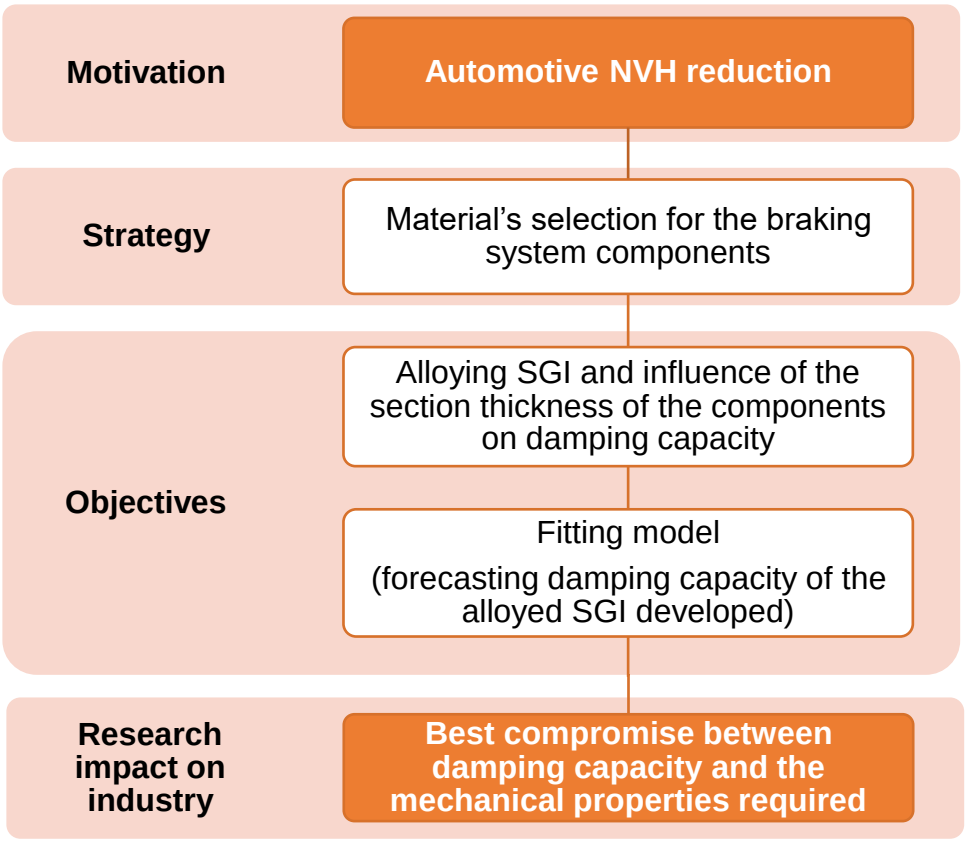


Figure 1 - 2. General schematic representation of the investigation paths of the thesis.

2. Literature Review

Chapter 2 presents the current state of knowledge on the damping capacity of cast irons. Firstly, it describes the general damping phenomena, their identification methods, a literature overview on cast irons, and studies regarding their damping capacity. Finally, the selected alloying elements studied under the scope of this thesis are listed.

2.1. Noise, Vibration and Harshness Control

The overall perception of a vehicle can be influenced by its noise and vibration performance since it is an issue closely related to reliability and quality. An audible noise causes environmental pollution and is regarded by drivers and passengers as a braking system failure. Therefore, developing a vehicle involves reducing noise and vibration to confer comfort and security to the occupants. Given the increased demand for this refinement, the NVH development of a vehicle becomes increasingly important.

The NVH is the field of measuring and modifying the noise and vibration characteristics of the vehicles' components. The noise and vibration sources can be from the engine, wheels, tyres, brakes, *etc.* On the other hand, harshness is related to the transient nature of this noise and vibrations and is a more subjective assessment [14, 15].

The audible noise emanating from a brake during a vehicle's run (which can occur even when the brakes are not being used – "off-brake") may be defined by the generic term "brake noise".

The noise originating from brakes can be considered a secondary source of noise in a vehicle. This noise occurs over a wide range of frequencies, typically from 100 Hz to above 20 kHz (the upper limit of human audibility). The brake squeal noise is often in the range of 1-6 kHz, where the human ear is most sensitive and is considered very annoying [14, 15].

In its turn, the judder from the braking system is also a significant concern to manufacturers and users. While the judder may also originate

audible noise, the main issue is the mechanical vibration sensed, for example, at the brake pedal [15].

There are many sub-categories within the brake noise and judder phenomena, which vary, for example, with their frequency. The following sub-categories are presented in ascending order of frequency: judder, groan, hum, moan, “low-frequency” squeal, high-frequency squeak and wire brush (Figure 2 - 1). Nevertheless, it is widely accepted that most brake noise originates from frictionally induced dynamic instabilities in the brake that create vibrations of the components, such as the disc or drum, which amplifies the signal and radiates as a sound that is heard [15].

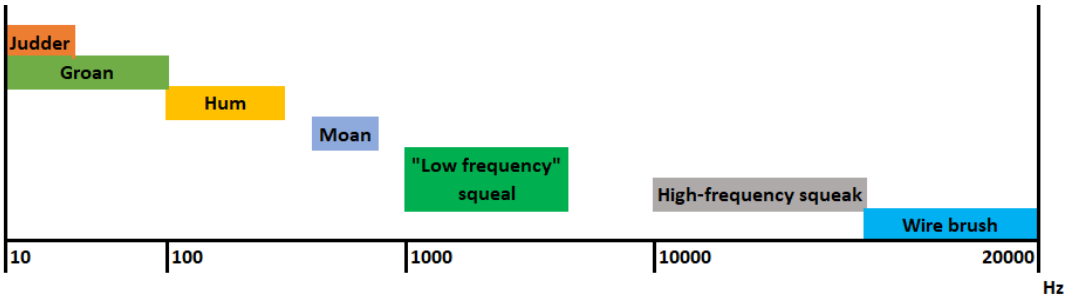


Figure 2 - 1. Sub-categories of the brake noise; adapted from [15].

In general, two factors can influence the vibration in a structure (which can create noise): the excitation applied and/or the structure response to this excitation, which depends on the dynamic characteristics of the structure (*e.g.*, by changing its mass or stiffness, or by increasing the inherent damping capacity of the structure) [16].

Therefore, several solutions can reduce vibration by modifying the vibration origin, vibration isolation, vibration damping, structural modification, and materials selection [17].

The vibration suppression, aiming to control noise and the stability of the systems, can be achieved by using high-damping components’ materials that passively attenuate the undesirable noise and vibration, which are transferred to the surroundings as heat. Therefore, a material capable of

dissipating energy from vibrations has the potential to minimize noise problems in the braking system [4, 16, 18].

2.2. Damping

2.2.1. General phenomena

Damping relates to converting the mechanical energy associated with vibration into heat or sound, which becomes unavailable for the vibration. Thus, over time, *i.e.*, in each vibration cycle, the energy of free oscillations of a structure is absorbed [19-22]. Damping is inherently present in a mechanical system through different damping mechanisms and originates the dissipation of dynamic energy. There are three primary damping mechanisms: internal damping (damping inherent to the material), structural damping (joints and interfaces) and fluidic damping (fluid-structure interactions) [16, 23, 24]. The damping inherent to the material, or internal friction, is the main focus of this thesis.

Internal friction is the dissipation of mechanical energy within materials due to deformation. This dissipation is related to microstructural defects, such as grain boundaries and impurities, thermoelastic effects from local thermal gradients, Eddy current effects (ferromagnetic materials), and movement of dislocations and vacancies to positions energetically more favourable (metallic materials) [16, 23-26]. So, for metallic materials, the main damping mechanisms are the displacement of the dislocations and the rearrangement of defects in the crystal structure of the material induced by stresses [22]. Once it reaches a state of mechanical equilibrium, the energy will be dissipated as heat and sound, denominated by damping or mechanical loss. This friction between the microstructural interfaces results from a complex intramolecular relationship that depends on several characteristics, mainly the material and the processing and finishing methods [23, 25-27].

Several mathematical models have been developed to represent the energy dissipation caused by internal damping; the variety of models is a natural consequence of the wide range of materials, and, therefore, no single model can be used to cover all the materials [23, 28].

Various equivalent damping parameters can characterize the damping capacity of a material; the most common are loss factor (η), specific damping capacity (ψ), damping factor (ζ), logarithmic decrement (δ), and internal friction (Q^{-1}).

When the materials present a low damping factor ($\zeta < 0.1$), like the majority of metals, a relation between all damping parameters can be established [20, 23, 26, 27, 29-34]:

$$\eta = \psi/(2\pi) = 2\zeta = \delta/(\pi) = Q^{-1} \quad (1)$$

The damping capacity of a material translates into its ability to dissipate elastic energy during mechanical vibration (or wave propagation) by passively attenuating and removing it to the surroundings as energy [19, 20, 35]. The materials are usually categorized into low or high damping capacity, the last being applied to suppress vibration for noise control [30].

The damping capacity depends on the speed of the sound propagation through the material, being the length and fraction of the waves dependent on the material's structure. So, a material capable of disturbing long waves' propagation and forming many waves, with shorter wavelengths, presents a higher damping capacity. The same effect is registered for materials with precipitates in the matrix, acting as waves' disturbers [2].

2.2.2. Identification methods

Determining the damping capacity of metals is very sensitive to experimental conditions, such as strain amplitude, frequency, temperature and humidity. It represents a challenge as the comparison between the values obtained from different tests is difficult to ascertain due to the wide range of techniques and parameters. The values from the literature can present a significant variation for each type of material since they depend on the internal structure of the materials (due to potential differences in alloying) and the accuracy of the different methods used [23, 29, 30].

The technique used in this thesis for the damping characterization belongs to the resonance group, fitting in the free decay method subgroup. Free decay methods induce free damped vibrations after turning-off the excitation [28].

This thesis will particularly deal with the Impulse Excitation Technique, an experimental technique that uses a time response record and, therefore, belongs to a time-domain analysis. It is advantageous essentially for low damping capacity values [26].

2.2.2.1. Impulse Excitation Technique

The Impulse Excitation Technique (IET) is a method that allows the determination of the damping parameters of vibration, such as the internal friction. It presents some advantages: essentially non-destructive method, simplicity, more effectiveness in cost and time, minimal specimen preparation, small quantities of material to be tested, and data accuracy. Furthermore, this technique can be used at a wide range of temperatures, from cryogenic to high temperatures, and is thus helpful for a broader scope of potential implementations. The analytical equations for determining the properties are modified for high temperatures to account for the materials' expansion.

Some factors may negatively interfere with these tests, inducing a higher error probability. For example, materials with a high damping capacity may be difficult to test with this technique if the vibration has been damped before measuring the signal (commonly within three to five cycles). On the other hand, porosities, cracks, rough surfaces, and discontinuities may cause additional measurement errors [24, 29, 31, 33, 36-41].

The test specimens are mechanically excited through a single-elastic strike using an impulse tool to make them vibrate at one or more of the expected resonant frequencies. A transducer, as a microphone with an adequate frequency range, detects the sound produced by the vibration of the specimen, being the signals then analysed. The acoustic signal is recorded in the time domain; then, the software transforms this signal to the frequency

domain and determines the first set of approximate resonant frequencies (f_r) by Fourier analysis.

The damped vibration (Figure 2 - 2), for each f_r, is determined from the equation:

$$x(t) = A\, e^{-kt} \sin(2\pi f_r\, t + \phi) \qquad (2)$$

where:

A – initial amplitude;

k – exponential damping;

ϕ – phase angle.

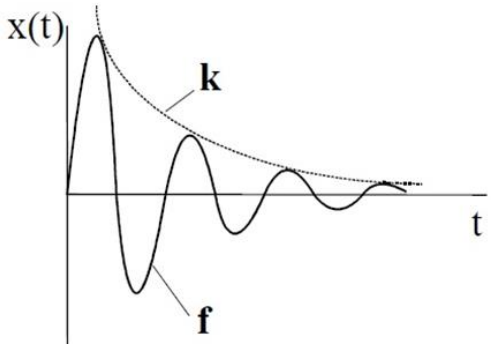


Figure 2 - 2. Sinusoidal damped vibration; adapted from [42].

The software performs an iterative simulation of the measured time-domain signal as a sum of exponentially damped sinusoidal functions (transient sinusoidal waves – Equation (3)); the parameters A, k, f_r and ϕ are optimized by an iterative process. When a pre-determined convergence criterion is reached, the final f_r is presented. For each, a value k represents the exponential decay parameter of the vibration component of frequency [24, 25, 29, 31, 33, 37-47]:

$$x(t) = \sum A_i\, e^{-k_i t} \sin\left(2\pi f_r\, t + \phi_i\right) \qquad (3)$$

The internal friction (Q^{-1}) is obtained, for each corresponding k and f_r, from the equation:

$$Q^{-1} = k/(\pi f_r) \quad (4)$$

As the energy dissipates (Figure 2 - 3), it is possible to calculate the amplitude decay of the free vibration and, consequently, deduce the internal friction of the system that represents the energy absorption by the material.

In conclusion, this method determines the material's damping capacity from its acoustic response attenuation after an impulse excitation [24, 25, 29, 31, 33, 37-47].

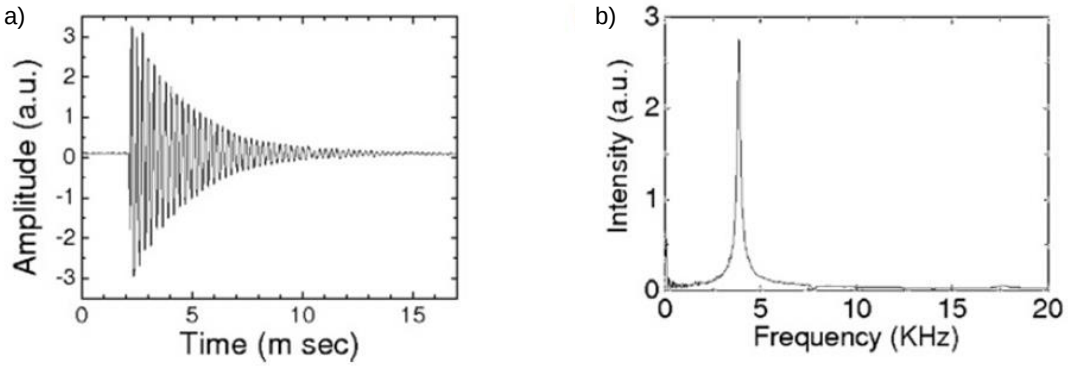


Figure 2 - 3. a) Amplitude of the vibration of the sample *vs.* time. b) A spectrum of the resonance frequencies obtained by using fast Fourier transform from the data shown in a); adapted from [48].

The vibration modes (flexure, torsion or longitudinal) excited during the test depend on the geometry of the sample, the point of impact and the type of support. As these modes are well established for simple shapes (bars, discs, *etc.*), the supports can be placed on the respective nodes to reach the specific modes of vibration and minimize the frictional losses on supports; in turn, the impact is applied on the anti-node (Figure 2 - 4) [31, 36].

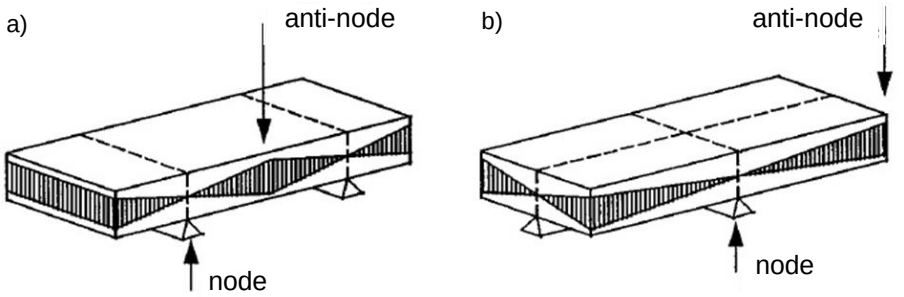


Figure 2 - 4. Positioning of rectangular bars to be tested on the supports for: a) flexural vibration mode, and b) torsional vibration mode; adapted from [31].

It is possible to determine the elastic properties (Young's modulus, shear modulus and Poisson's ratio) when fundamental vibration modes are reached because they are interrelated.

The fundamental flexural and longitudinal modes are correlated to Young's modulus in the longitudinal direction. They can be determined by identifying the fundamental flexure resonant frequency, while the fundamental torsion mode is correlated with the shear modulus. On the other hand, Poisson's ratio can be calculated from an analytical equation that correlates Young's and shear modulus for isotropic materials.

For well-established shapes, several international standards (the most general one is the ASTM E 1876) establish correlations between the elastic properties (dynamic Young's modulus, shear modulus and Poisson's ratio) and the resonant frequency identified [25, 31, 33, 36, 43, 44].

For a rectangular bar, the dynamic Young's modulus, the dynamic shear modulus and the Poisson's ratio are obtained from Equations (5), (6) and (7), respectively.

For the dynamic Young's modulus:

$$E = 0.9465\ (m\ f_f^2/b)\ (L^3/t^3)\ T_1 \qquad (5)$$

where:

E – dynamic Young's modulus (Pa);

m – bar mass (g);

f_f – fundamental resonant frequency of the bar in flexure (Hz);

b – bar width (mm);

L – bar length (mm);

t – bar thickness (mm);

T_1 – correction factor for the fundamental flexural mode to account for finite bar's thickness, Poisson's ratio, and so forth.

$$[T_1 = 1 + 6.585\ (1 + 0.0752\ \mu + 0.8109\ \mu^2)\ (t/L)^2 - 0.868\ (t/L)^4 - \left(\frac{8.340\ (1 + 0.2023\ \mu + 2.173\ \mu^2)\left(\frac{t}{L}\right)^4}{1.000 + 6.338\left(1 + 0.1408\ \mu + 1.536\ \mu^2\right)\left(\frac{t}{L}\right)^2}\right)]$$

with:

μ – Poisson's ratio.

On the other hand, concerning the dynamic shear modulus:

$$G = \frac{(4\ L\ m\ f_t^{\ 2})}{b\ t}\ (B/(1 + A)) \qquad (6)$$

with:

G – dynamic shear modulus (Pa);

f_t – fundamental resonant frequency of the bar in torsion (Hz);

B – an empirical correction factor $[B = \frac{b/t + t/b}{4\ (t/b) - 2.52\left(t/b^2\right) + 0.21\ (t/b^6)}]$;

A – an empirical correction factor, which can be omitted for accuracy < 2%.

$$[A = \frac{0.5062 - 0.8776\ (b/t) + 0.3504\ (b/t)^2 - 0.0078\ (b/t)^3}{12.03\ (b/t) + 9.892\ (b/t)^2}]$$

Finally, the Poisson's ratio is calculated from:

$$\mu = (E/2G) - 1 \qquad (7)$$

In this work, the internal friction and the fundamental frequency on flexural mode were determined. The elastic properties (Young's modulus, shear modulus and Poisson's ratio) were also characterized.

As aforementioned, this work is focused on how to increase the damping capacity of spheroidal graphite iron used to produce some braking system components. The reason is that with higher damping capacity, a more significant fraction of vibrational energy might be dissipated in each cycle, and the total energy radiated in the form of sound can be reduced [49].

2.3. Cast irons' characterization

Cast irons are ferrous alloys composed primarily of Fe, C and Si. Other alloying elements can be added to manipulate some of their properties, such as Cu, Sn, Ni, Cr, and Mn, among others.

At the eutectic reaction, the C content exceeds the maximum content retained in austenite, precipitating as graphite or cementite (Fe_3C). This occurrence led to cast irons being classified into two main classes: white and grey cast irons.

In white cast irons, C precipitates as cementite by a metastable solidification; in turn, in grey cast irons, it precipitates in the form of graphite by a stable solidification [50].

It should be stated that, within the grey cast irons class, the different shapes of the graphite's precipitates led to a complementary classification [50]:

- Flake Graphite Iron (FGI);
- Compacted Graphite Iron (CGI);
- Malleable Iron;
- Spheroidal Graphite Iron (SGI).

Figure 2 - 5 presents the microstructures of cast irons, with different graphite morphologies, observed by Scanning Electron Microscopy (SEM).

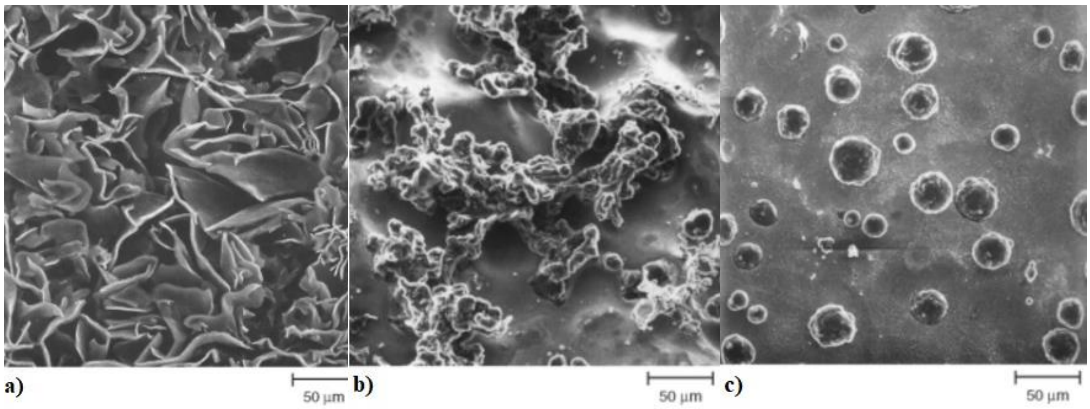


Figure 2 - 5. SEM micrographs of deeply etched cast irons with different graphite morphologies: a) flake, b) compacted, c) spheroidal; adapted from [51].

The classification of the graphite morphology follows the EN ISO 945-1 standard, comprising six groups. The correspondence between the graphite forms, patent in Figure 2 - 6, and the different types of cast irons is the following [50, 52]:

- Forms I and II correspond to flake graphite iron, with graphite precipitating in the form of lamellae;
- Form III corresponds to compacted graphite iron;
- Form-IV corresponds to malleable cast iron;
- Forms V and VI correspond to spheroidal graphite iron, with graphite precipitating as nodules.

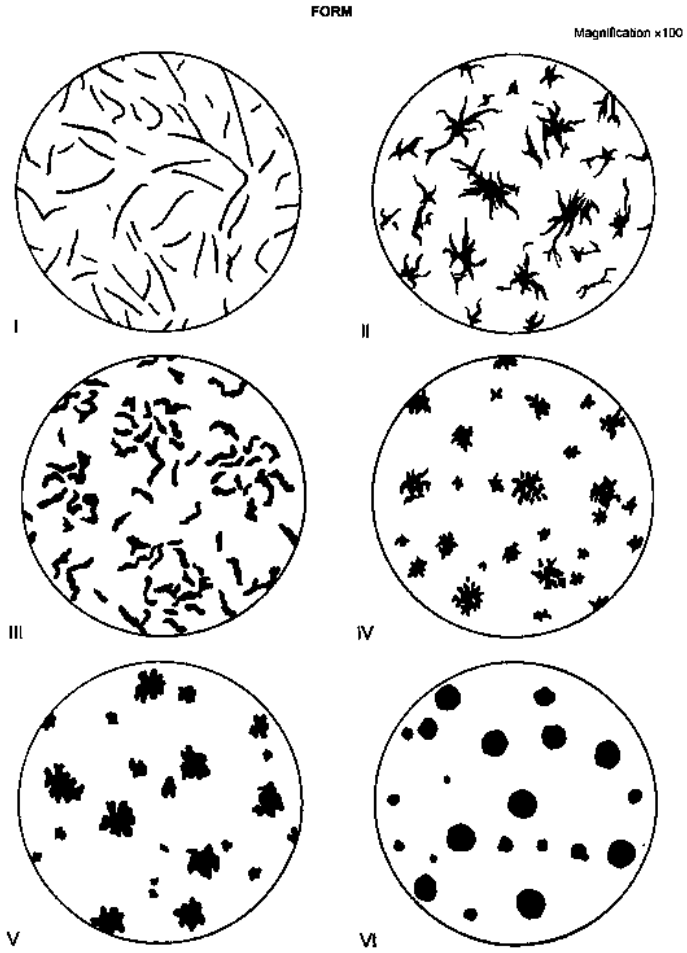


Figure 2 - 6. Graphite morphologies in cast irons, according to the EN ISO 945-1: 2008 standard [52].

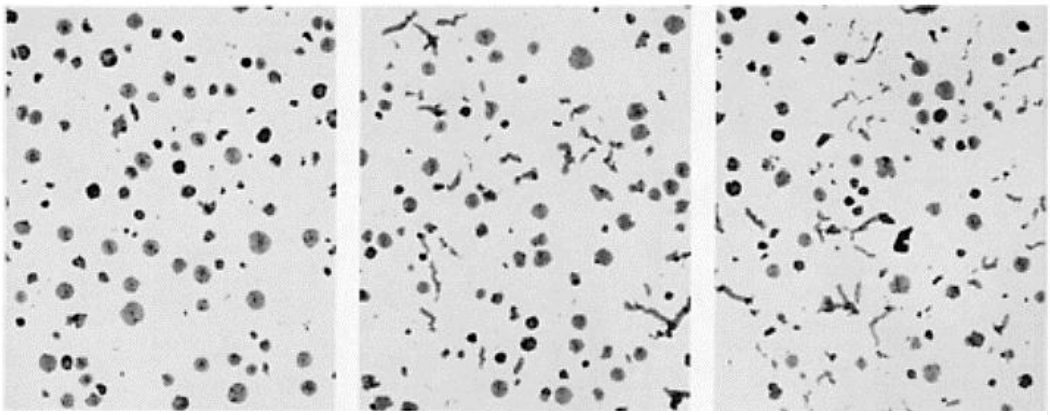
Due to the involvement and interest of the project's partner *AAPICO* in developing an SGI with higher damping capacity, the characterization of this cast iron will now be presented.

2.3.1. Spheroidal graphite irons

SGIs are characterized by the precipitation of C in the form of graphite spheroids, known as nodules, distributed within a matrix rich in Fe. The extent to which graphite particles present a spherical shape (Figure 2 - 7) can be evaluated by their nodularity, established from Equation (8). For SGI, a structure with a nodularity between 80 and 100% is acceptable [53].

The factors influencing the graphite shape and fraction will be described later (*sub-chapter 2.3.1.3.*).

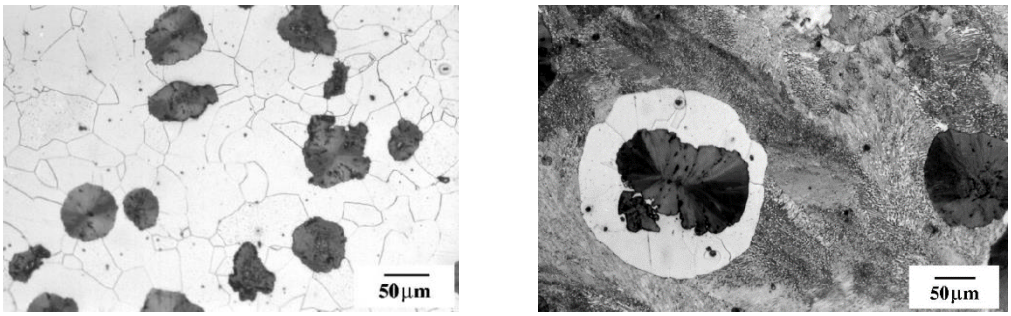
$$\text{Nodularity (\%)} = \frac{(0.9*\text{area of graphite form-V} + \text{area of graphite form-VI})}{\text{Total area of the graphite particles}} \times 100 \qquad (8)$$



a) b) c)

Figure 2 - 7. SGI microstructures of varying degrees of nodularity: a) 99%, b) 80%, c) 50%. All unetched samples [50].

In turn, the matrix can be fully ferritic, fully pearlitic, or ferritic/pearlitic (Figure 2 - 8). The matrix will depend on the alloying elements (promoters either of pearlite or ferrite formation), the cooling rate of the different casting's sections and the nodule count per square millimetre, as will be described later [50, 51].



a) b)

Figure 2 - 8. SGI microstructures, etched with Nital, with: a) fully ferritic matrix, b) pearlitic-ferritic matrix [54].

2.3.1.1. Production process

The SGI's production can be performed using different melting and pouring techniques.

2.3.1.1.1. Base iron melt preparation

Melting is usually performed using medium frequency electrical induction furnaces for medium to low volumes, whereas, for high production volumes, cupola melting furnaces can also be used.

The base iron charge composition is typically steel scrap, special-quality pig iron for SGI production, and SGI returns. The chemical composition of the base iron melt is adjusted by adding alloying elements, such as C, Si, Cu, Sn, and Mn, among others. For instance, if the desired grade is an SGI with a ferritic matrix, low Cu and Sn contents are necessary, whereas grades that should present a fully pearlitic matrix have a high Cu content (up to 0.9%) and, potentially, Sn (up to 0.09%) [55].

After the preparation of the base iron melt, it follows the modification treatments, which are performed to produce SGI, involving the addition of Mg to change the graphite shape (nodularizing treatment), followed by or combined with the inoculation by a Fe-Si alloy to guarantee a graphitic structure with no carbides (inoculation treatment).

2.3.1.1.2. Nodularizing treatment

The production of SGI requires a nodularizing treatment; it increases the Mg content of the melt to 0.04-0.06%, usually by adding a Fe-Si-Mg alloy with 5-8% Mg.

There are different techniques for performing the nodularizing treatment; the well-established sandwich method was used in this work. In this method, a special Fe-Si-Mg alloy is placed in a pit at the bottom of the transport or pouring ladle before pouring the melt into the ladle [50, 55].

2.3.1.1.3. Inoculation treatment

The inoculation treatment promotes the heterogeneous nucleation of graphite particles, *i.e.*, a stable solidification; inoculants, usually Fe-Si alloys, containing some active elements such as Ca, Al, Sr and Ce, are added.

This treatment can involve multiple additions of inoculant at different stages of the production process. In this work, two types of inoculation techniques were used: mould inoculation, where the inoculant is added in a compartment designed explicitly in the gating system, and ladle inoculation, being the inoculant added simultaneously with the Fe-Si-Mg alloy used for the nodularizing treatment [50, 55].

2.3.1.1.4. Process control

During the production of SGI, different techniques can be used to control the process; the following are the most common [55]:

- Chemical analysis is used in the base iron melt preparation and after the modification treatments and pouring (spectrometer and combustion analyser for the determination of the C and S contents);
- Thermal analysis is used to fast estimate the Carbon Equivalent (C.E.) and C and Si contents during the preparation of the base iron melt. In most advanced processes, this technique is also used after treatment or at pouring to replace more traditional methods such as the metallographic analysis and the wedge sample. Samples are collected during the process and selected to allow an active and effective correction of the melt composition before pouring. The technique is used to estimate metallographic characteristics (nodularity, nodule count, tendency to form iron carbides, and fractions of pearlite and ferrite);
- Temperature measurement in base iron melt preparation and after treatment or at pouring;

- Microstructural analysis, after treatment or at pouring, comprises the pouring of a sample from the melt into a small sand mould for a quick analysis of the microstructure;
- Wedge sample after treatment or pouring to evaluate the inoculation treatment efficiency.

To ensure that castings meet the specified requirements, mechanical properties and microstructural analysis may be conducted periodically on test specimens machined from the castings. The selected tests depend on the customer's requirements for a given casting. For instance, tensile tests might be performed to determine tensile and yield strengths and elongation, hardness tests and microstructural analysis to evaluate the nodularity and nodule count as well as the type of matrix.

Concerning the soundness and integrity of the castings, an X-ray inspection is commonly used to verify the presence of internal defects.

In addition, complete control of critical safety castings is usually carried out using ultrasonic testing to verify their nodularity.

2.3.1.2. Solidification mechanisms

Solidification is an important step in material processing, especially in cast irons that will not be further manipulated (by heat treatment, for example) to change their microstructure. Therefore, solidification constitutes the step where the as-cast microstructure is defined. As described later, the microstructure determines the material's mechanical properties.

Either grey or white, cast iron follows the solidification steps deducible from the analysis of the Fe-C phase diagram presented in Figure 2 - 9. Cast irons solidify with a eutectic transformation of a liquid in austenite and graphite (or Fe_3C in the case of the metastable solidification); the melt presents a C content higher than the upper C content in austenite [50, 55].

In the cases where C precipitates as graphite, the eutectic transformation is stable and occurs at 1152ºC (dotted line at the eutectic transformation stage in Figure 2 - 9). When C precipitates as iron carbide

(Fe_3C), the transformation occurs at 1145ºC (solid line at the eutectic transformation stage in Figure 2 - 9).

For C > ~4.3 wt.% (the eutectic point), there are also two liquidus curves corresponding to the stable solidification (dotted curve) and the metastable solidification (solid curve) [50, 55].

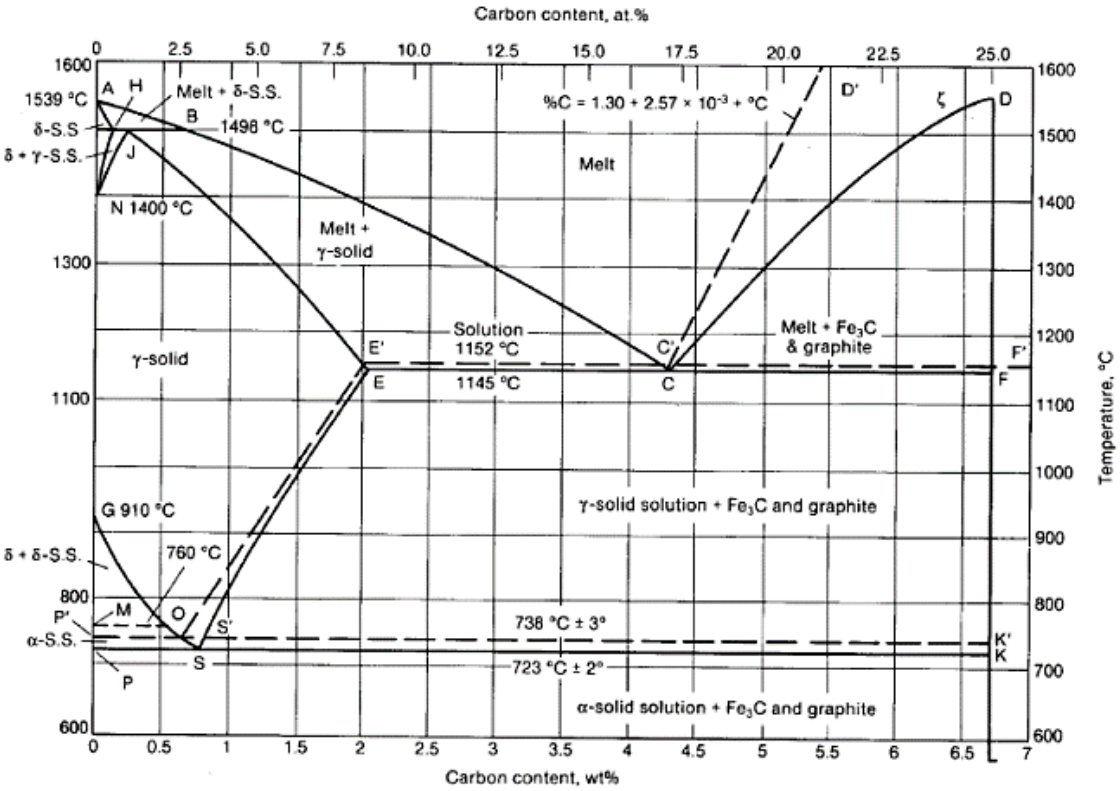


Figure 2 - 9. The Fe-C phase diagram [55].

The melts are classified based on their C content as: hypoeutectic, C < 4.3 wt.%; hypereutectic, C > 4.3 wt.% and eutectic, C ~4.3 wt.%. The primary phase to solidify differs with the C content of the melt: austenite for hypoeutectic melts, and graphite for hypereutectic melts, in the case of stable solidification. For eutectic melts, no primary phase will precipitate [55].

However, cast irons are more complex alloys with a significant Si content. The presence of Si on cast iron induces changes in the Fe-C diagram, imposing to consider the ternary phase diagram Fe-C-Si; so, a variable known as Carbon Equivalent (C.E.) has been defined. This represents a fictional C content in the Fe-C phase diagram, considering that the presence of Si in the

melt acts as additional C. There are several C.E. formulas, but the one considered in this thesis is represented by Equation (9); it includes the influence of P that acts similarly to Si [50, 55, 56].

$$\text{C.E. (\%)} = \text{C (\%)} + \frac{\text{Si (\%)} + \text{P (\%)}}{3} \quad (9)$$

Using this C.E. value in the X-axis, instead of the effective C content of the melt, it is possible to use the binary Fe-C phase diagram to determine if the melt is hypoeutectic, eutectic or hypereutectic. The eutectic point is considered for a C.E. of 4.3 wt.% [50, 55, 56].

Apart from Si, other elements can influence the cast irons' solidification. They can be classified as graphitizing elements such as Ni, Cu and Co (which increase the stable eutectic temperature and decrease the metastable eutectic temperature, like Si) and non-graphitizing elements such as Cr and V that will have an opposite effect on the eutectic temperature [55].

The next sub-topic summarizes the influence of chemical composition, cooling rate, and modification treatments on the SGI microstructure.

2.3.1.3. Factors influencing the microstructure of as-cast SGI

Several factors can influence the microstructure of as-cast SGI, like chemical composition, the cooling rate, and the modification treatments performed on the molten metal (inoculation and nodularization). The following sections will discuss factors influencing the graphite morphology and its fraction, as well as the type of matrix. It is worth noticing that this thesis will not consider any heat treatment.

2.3.1.3.1. Chemical composition

All elements in the chemical composition of SGI need to be duly controlled to guarantee compliance with the standards. This section describes the most common ones and their influence on the microstructure and, consequently, on the SGI mechanical properties.

Carbon

C derives from pig iron, cast iron scrap and carburizers. C is the primary element of all cast irons since it has the highest graphitizing potential; additionally, it has the most substantial influence on the melt's castability. The standard range for C in SGI is 3.0-4.0 wt.%, depending on the Si content.

C contents higher than 4.0% might induce irregular graphite forms and graphite flotation, particularly in heavy casting's sections. Moreover, it increases the casting expansion during solidification, leading to casting unsoundness.

C contents lower than 3.0% might lead to a lack of feeding (enhancing solidification shrinkage), and unsoundness of the casting is also observed. Also, carbides may appear at very low C contents, particularly in thin casting's sections [50, 57].

Silicon

This element is derived from cast iron scrap, pig iron, and ferroalloys used in the modification treatments (inoculation and nodularization). Si is a graphitizing element, increasing the C activity in the molten metal, forcing C out of solution and forming graphite; its standard range is 1.8-2.8 wt.% Si.

Lower Si contents in thin sections might lead to iron carbide formation since metastable solidification would be promoted; higher Si contents accelerate annealing (being a strong ferritizer) and help avoid carbides' precipitation [50, 55, 56].

To avoid graphite's flotation for high C.E. contents, C should be in the range of 3.2-3.5 wt.%, depending on the section thickness.

Hypereutectic melts in thicker sections are prone to promote graphite flotation since primary graphite (lower density) will be able to emerge to the surface (slow cooling rate) [50, 55, 56]. Moreover, the presence of some degenerated graphite, such as chunky graphite, is related to Si contents above 4.2 wt.%; meanwhile, Sb addition has proven to be effective in decreasing its formation, even at Si contents higher than 6 wt.%. This implies that the critical Si content might increase when Sb is added. The literature reports that the critical Si content at which solution embrittlement starts is 4.2-4.4 wt.% [58-66].

Manganese

The primary source of this element is steel scrap of the charge. In as-cast ferritic irons, it should be ≤ 0.2 wt.%, while, in the as-cast pearlitic irons, it can reach 1 wt.% since it is a pearlitizer. However, its content should be limited since it can segregate to grain boundaries, particularly in thick sections, resulting in the precipitation of carbides [50].

Phosphorus

The common source of this element is pig iron and steel scrap. Although it increases the fluidity of the melt, it is usually kept as low as possible (< 0.03 wt.%) since it promotes microporosity, forming a low melting eutectic phosphide at the grain boundaries, and the formation of pearlite [50, 57].

Sulphur

This element derives from carburizers, pig iron, steel scrap, and mould sand. The S content of SGI is usually < 0.01 wt.%.

This element is essential for graphite nucleation, and a minimum content of 0.005 wt.% is recommended. However, flake graphite formation will occur, if not neutralized, instead of nodular graphite. Higher S contents at the base iron will increase the Mg consumption and, consequently, might originate slag and dross and reduce the consistency of the nodularizing treatment [50, 57].

Magnesium

Mg is essential in producing SGI; so, it is used in the nodularizing treatment. This element is a deoxidizer and desulphurizer, *i.e.*, it neutralizes the S and the O by forming MgS and MgO, allowing the growth of graphite with spheroidal form.

An Mg content in the range of 0.04-0.06 wt.% is required, and its common sources are Mg and its alloys (nodularizers used for nodularizing treatment). Compacted graphite structures might be formed for lower Mg contents, while higher Mg contents may promote dross defects [50, 57].

Rare-Earth elements

RE elements, like Ce, might be added as minor components through nodularizer and inoculant alloys to increase the inoculation efficiency and improve graphite morphology and its growth. Moreover, Ce is also a deoxidizer and desulphurizer, promoting the precipitation of nodular graphite. Additionally, it might be added to neutralize undesirable trace elements that could interfere with spheroids' formation, such as Ti, Al and Sb. However, Ce at high contents can promote the precipitation of carbides in thin sections and chunky graphite in thick sections; the latter might be counteracted by controlled additions of Sb and Sn [50, 57].

La, another RE element, presents a similar influence on microstructure as Ce. In several reported works [67-71], these elements increase the nodule count, either individually or combined.

Moreover, adding RE elements significantly minimizes nodularity variation with thickness and increases the ferrite layer's fraction around the nodules [71].

Copper

This element is commonly used to produce pearlitic SGI grades. For instance, Cu up to 0.9 wt.% can be added to the ladle when fully pearlitic structures are required. On the other hand, higher contents (> 1 wt.%) might induce the degeneration of the graphite form.

The common source of addition is Cu metal (wrought and wire) and its alloys; the selection of the source is essential as it may also contain trace elements that would be harmful, such as As, Pb and Te [50, 55, 57].

Aluminium

The presence of even trace amounts of Al in SGI may promote pinhole porosity, dross formation and the precipitation of non-spheroidal graphite; therefore, its presence is usually avoided. The most common sources are steel and cast iron scrap and Al-containing inoculants [50, 56].

Nevertheless, some research has been carried out on SGI alloyed with Al; the alloys were divided into two groups: the first for contents up to 6% and the second for contents in the range of 18-25% Al [72].

More recently, Ibrahim *et al.* [73] observed that the graphite transforms from spheroidal to compacted with Al addition up to 4 wt.%, while, for Al contents in the range of 5.8-13.8 wt.%, they registered a reduction of the fraction of ferrite, the volume fraction and nodule count of graphite, and the precipitation of intermetallic compounds (FeAl, $AlFe_3C$ and Fe_3Al). For the samples with 16 wt.% Al, the authors verified a microstructural change from a hard matrix (carbides and ferrite) to a soft one (“ferrite”, a non-magnetic phase with Al in solution, and graphite).

Chromium

It is a pearlitizing element; its content is maintained very low since it is a strong carbide promoter [57].

Titanium

It is a pearlite promoter; it should be kept low in SGI since it induces nodule count reduction and, at high contents, might impair the formation of nodular graphite [57].

Molybdenum

This element might be added as a pearlitizer; at high contents, it segregates strongly, forming stable carbides at the grain boundaries. It is usually used up to 0.1 wt.% [57].

Tin

It is a strong pearlite promoter and can be used in combination with Cu to stabilize the pearlite fraction for castings with thick sections. Sn, up to 0.1 wt.%, can be added to the ladle when fully pearlitic structures are required [50, 57].

Antimony

It is also a strong pearlitizer and can be added for castings with thick sections to counteract the formation of chunky graphite. Moreover, as previously mentioned, Sb can be used to offset the influence of RE elements in promoting chunky graphite occurrence in thick sections. If RE elements are not present, Sb might promote the formation of spiky and lamellar graphite, decreasing nodularity [57].

Cobalt

The impact of Co on SGI was studied by Hsu *et al.* [74]. They concluded that 4 wt.% Co originates a higher graphite nodule count than non-alloyed SGI. It was also verified that Co is homogenously dissolved into the matrix and is a ferrite stabilizer [74].

2.3.1.3.2. Cooling rate

The cooling rate is the one at which the temperature of the melt decreases with time, being significantly impacted by the section thicknesses of the castings; thin sections promote higher cooling rates. The cooling rate might influence the nodule size, nodularity, and type of matrix.

As the section thickness decreases, a fine grain structure will be obtained, and a higher nodule count (smaller nodules) will be achieved (Figure 2 - 10) [50, 51].

As already described, low cooling rates and high Si contents usually promote the obtainment of a ferritic matrix. On the other hand, high cooling rates increase pearlite's fraction.

It is worth noticing that carbides formation might be promoted with a fast cooling rate, *i.e.*, in thinner sections. Therefore, it is necessary to balance an efficient inoculation to prevent their precipitation and promote a graphitic structure, as discussed in the next section [50, 51].

2.3.1.3.3. Inoculation

As previously seen, the size and nodule count strongly depend on the casting section thicknesses and the inoculation potential of the melt.

An efficient inoculation promotes graphite precipitation, avoiding the presence of carbides in the microstructure, particularly in thin sections. If no inoculation treatment is performed, the melt will present a substantially low potential to precipitate graphite [50].

A correct inoculation induces a high nodule count, increasing the fraction of ferrite in the as-cast microstructure [50].

Moreover, the moment of adding the inoculant and its mass also influence the nodule count (which, as already described, might affect the fraction of ferrite).

Figure 2 - 10 shows that a late inoculation (addition to the metal stream during the pouring to the mould) has a higher impact in increasing nodule count than the inoculation in the ladle; this advantage is more relevant for thinner castings' sections. Moreover, the nodule count increases with the Si added by the inoculant (Figure 2 - 11) [50, 51, 75].

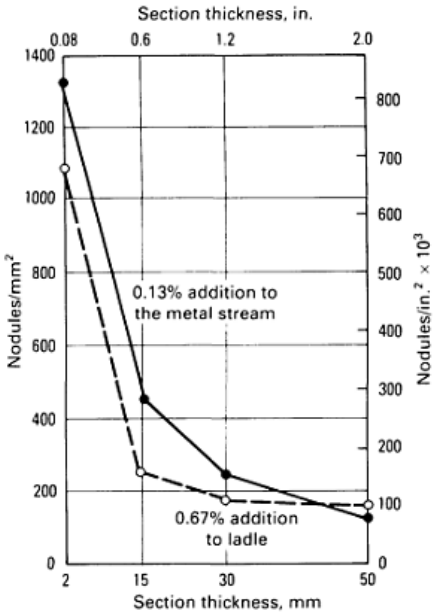


Figure 2 - 10. Nodular graphite particles count in SGI inoculated with standard foundry grade FeSi (75% Si), added to the ladle or the metal stream, *vs.* section thickness of the casting [50].

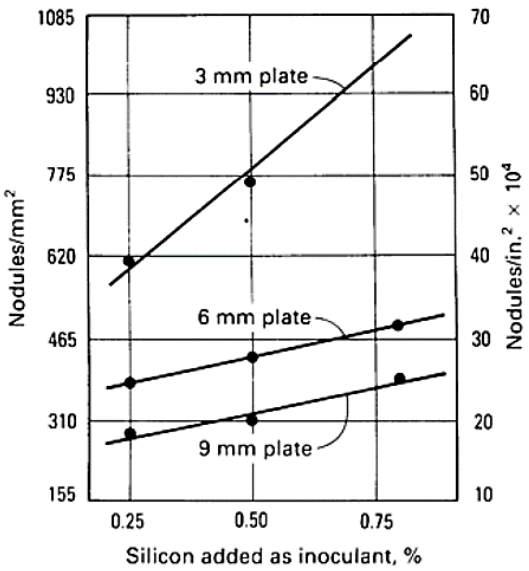


Figure 2 - 11. Nodule count *vs.* the Si (%) added as inoculant (addition in the ladle) [50].

In this sub-chapter, the main factors that might influence the as-cast microstructure were verified. In the following section, the influence of the microstructure on the SGI mechanical properties, particularly the damping capacity, will be presented.

2.3.2. Mechanical properties

The microstructure of an alloy, and particularly of an SGI, will determine its mechanical properties. This alloy is particularly interesting when high strength and ductility are required for a specific application. As already described, its microstructure might vary in graphite form or its fraction and/or matrix type; consequently, different SGI grades might be produced.

According to the DIN EN-1563:2011 standard [58], the spheroidal graphite iron with the lower tensile strength is GJS-350-22 (350 MPa for the tensile strength and 22% for elongation), with a ferritic matrix. In turn, the class with the highest tensile strength is GJS-900-2 (900 MPa for the tensile strength and 2% for elongation), presenting a fully pearlitic matrix (Table 2 - 1).

Table 2 - 1. Mechanical properties measured on test pieces machined from cast samples of ferritic to pearlitic grades [58]

Material designation		Relevant wall thickness	0.2 % proof strength	Tensile strength	Elongation
		t	$R_{p0,2}$	R_m	A
		mm	MPa	MPa	%
Symbol	Number		min	min	min
EN-GJS-350-22-LT [a]	5.3100	$t \leq 30$	220	350	22
		$30 < t \leq 60$	210	330	18
		$60 < t \leq 200$	200	320	15
EN-GJS-350-22-RT [b]	5.3101	$t \leq 30$	220	350	22
		$30 < t \leq 60$	220	330	18
		$60 < t \leq 200$	210	320	15
EN-GJS-350-22	5.3102	$t \leq 30$	220	350	22
		$30 < t \leq 60$	220	330	18
		$60 < t \leq 200$	210	320	15
EN-GJS-400-18-LT [a]	5.3103	$t \leq 30$	240	400	18
		$30 < t \leq 60$	230	380	15
		$60 < t \leq 200$	220	360	12
EN-GJS-400-18-RT [b]	5.3104	$t \leq 30$	250	400	18
		$30 < t \leq 60$	250	390	15
		$60 < t \leq 200$	240	370	12
EN-GJS-400-18	5.3105	$t \leq 30$	250	400	18
		$30 < t \leq 60$	250	390	15
		$60 < t \leq 200$	240	370	12
EN-GJS-400-15	5.3106	$t \leq 30$	250	400	15
		$30 < t \leq 60$	250	390	14
		$60 < t \leq 200$	240	370	11
EN-GJS-450-10	5.3107	$t \leq 30$	310	450	10
		$30 < t \leq 60$	to be agreed upon between the manufacturer and the purchaser		
		$60 < t \leq 200$			
EN-GJS-500-7	5.3200	$t \leq 30$	320	500	7
		$30 < t \leq 60$	300	450	7
		$60 < t \leq 200$	290	420	5
EN-GJS-600-3	5.3201	$t \leq 30$	370	600	3
		$30 < t \leq 60$	360	600	2
		$60 < t \leq 200$	340	550	1
EN-GJS-700-2	5.3300	$t \leq 30$	420	700	2
		$30 < t \leq 60$	400	700	2
		$60 < t \leq 200$	380	650	1
EN-GJS-800-2	5.3301	$t \leq 30$	480	800	2
		$30 < t \leq 60$	to be agreed upon between the manufacturer and the purchaser		
		$60 < t \leq 200$			
EN-GJS-900-2	5.3302	$t \leq 30$	600	900	2
		$30 < t \leq 60$	to be agreed upon between the manufacturer and the purchaser		
		$60 < t \leq 200$			

NOTE The mechanical properties of test pieces machined from cast samples may not reflect exactly the properties of the casting itself.

[a] LT for low temperature.

[b] RT for room temperature.

Tensile strength is usually inversely proportional to elongation, and, in turn, hardness is generally proportional to the tensile strength (Figure 2 - 12) [50]. However, in addition to the standard ferritic and pearlitic SGIs already presented, new high Si solid solution strengthened grades have been developed (Table 2 - 2). Despite the higher tensile strength, these new grades present elongation values that are still considerably high, for instance,

comparing the 600-3 grade (pearlite-ferrite matrix) with the 600-10 grade (ferritic matrix). [58].

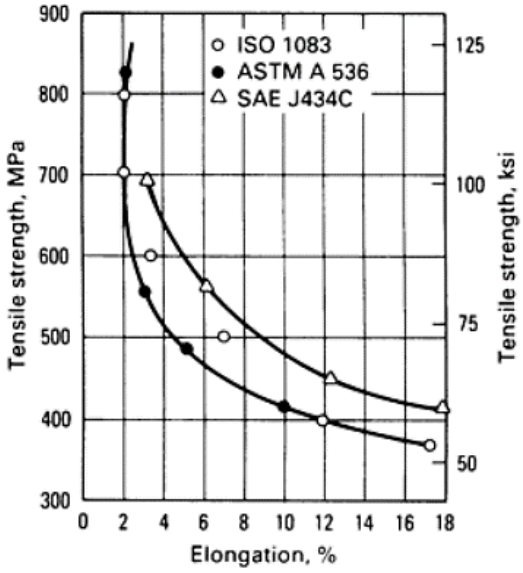


Figure 2 - 12. Relationship between the minimum specified values for the tensile strength and elongation in the range of values covered by the ISO, ASTM, and SAE standards [50].

Table 2 - 2. Mechanical properties measured on test pieces machined from cast samples of solid solution strengthened ferritic grades [58]

Material designation		Relevant wall thickness	0.2% proof strength	Tensile strength	Elongation
Symbol	Number	t mm	$R_{p0,2}$ MPa min	R_m MPa min	A % min
EN-GJS-450-18	5.3108	$t \leq 30$	350	450	18
		$30 \leq t \leq 60$	340	430	14
		$t > 60$	to be agreed upon between the manufacturer and the purchaser		
EN-GJS-500-14	5.3109	$t \leq 30$	400	500	14
		$30 \leq t \leq 60$	390	480	12
		$t > 60$	to be agreed upon between the manufacturer and the purchaser		
EN-GJS-600-10	5.3110	$t \leq 30$	470	600	10
		$30 \leq t \leq 60$	450	580	8
		$t > 60$	to be agreed upon between the manufacturer and the purchaser		
NOTE The mechanical properties of test pieces machined from cast samples may not reflect exactly the properties of the casting itself.					

The starting point for developing these SGIs was an improvement in machinability, maintaining or even increasing the mechanical properties of the ferritic-pearlitic SGI [76, 77]. One of the characteristic properties of these alloys is the high ratio of 0.2% offset yield strength/tensile strength (75% to 85%) compared to ferritic and pearlitic SGI (55% to 65%).

Concerning hardness, an increase was observed with Si content. An extension of the machining tool lives, in 50-60%, was achieved by using a solid solution strengthened SGI since a ferritic matrix can be easily machined compared to a ferritic-pearlitic one [62].

The type of matrix is the main factor in SGI mechanical properties, determining the different grades. The tensile strength will increase with the pearlite's fraction (Figure 2 - 13). However, as previously shown, new high Si grades, which present a full ferrite matrix (*i.e.*, pearlite < 5%[1]), can achieve similar tensile strength values to those of a pearlitic grade.

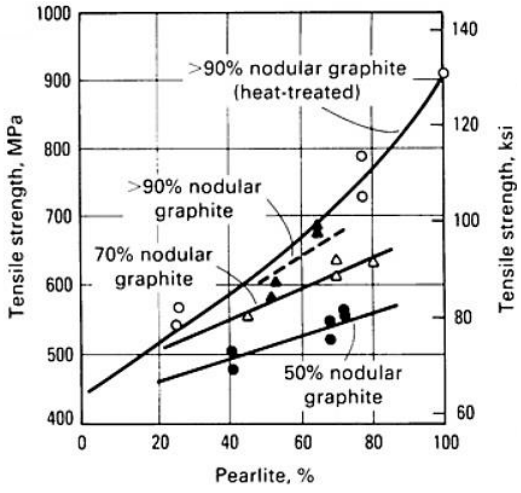


Figure 2 - 13. Tensile strength *vs.* pearlite's fraction of SGI with different nodularity [50, 78].

[1] According to DIN EN 1563:2012 standard [58], the matrix should be predominantly ferrite with a maximum pearlite content of 5%. The amount of free cementite should not exceed 1%.

The SGI's strength depends on the matrix type (ferritic/pearlitic); yet, the morphology of the graphite particles also has a strong impact. As nodularity decreases and the graphite starts getting irregular (for example, higher fractions of V and III forms), the tensile strength starts to decrease (Figure 2 - 14) since sharp edges (as for graphite flakes) have a more negative impact on the strength than rounded ends [50].

The degenerated graphite, as chunky graphite, can reduce the mechanical properties of spheroidal graphite irons, namely the ultimate tensile strength and elongation. It is reported that in SGI with %Si > 4.6 wt.%, chunky graphite is less influent on the ultimate tensile and yield strengths, suggesting that Si promotes the matrix's strengthening, overtaking the detrimental effect of the chunky graphite, except in terms of elongation [64, 66, 79-93].

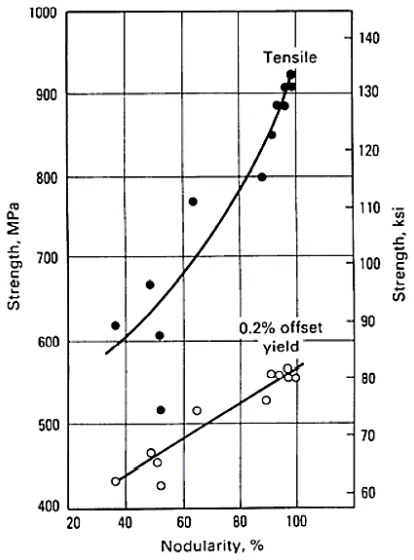


Figure 2 - 14. SGI tensile and yield strengths *vs.* its nodularity [50].

The fraction of graphite is generally not a significant variable since the C.E. is usually maintained close to the eutectic value (~4.3 wt.% C), which results in slight variations in the cast irons' mechanical properties. However, it is worth noticing that there will be a relative decrease in the tensile strength and elongation for higher fractions of graphite [50].

In the meantime, concerning defects' impact on SGI mechanical properties, carbides and non-metallic inclusions are known to decrease elongation.

As the primary objective of this project was developing an SGI with higher damping capacity, its characterization will now follow.

2.3.2.1. Damping capacity

The comparative analysis of the damping capacity[2] of SGI and FGI shows that the latter dissipates more energy of vibration due to its graphite morphology, the stresses being concentrated at the flake graphite edges during vibration. As the flakes disturb the propagation of long waves, many waves with shorter wavelengths are formed (precipitates in the matrix induce a similar phenomenon). Moreover, the interconnected and coherent three-dimensional structure presented by the graphite flakes imparts the excellent damping of vibrations. Thus, FGI presents a higher damping capacity than SGI [2, 72, 94].

On the other hand, CGI presents an intermediate damping capacity, namely by the presence of a still large surface area of the graphite precipitates despite the interruption of the three-dimensional coherent structure (which is favourable in terms of ductility) [2, 95-97]. Fox and Adams [98] observed that, as the shape of the graphite progressively transforms from flake to spheroidal, the damping capacity decreases. Hence, they concluded that, for cast irons, a high damping capacity could only be obtained at the expense of reducing its strength and ductility (Figure 2 - 15). Additionally, they observed that the matrix impact on damping was much smaller than the graphite morphology.

[2] As there are various parameters for characterizing the damping capacity, from now on, all damping parameters will be referred to as damping capacity.

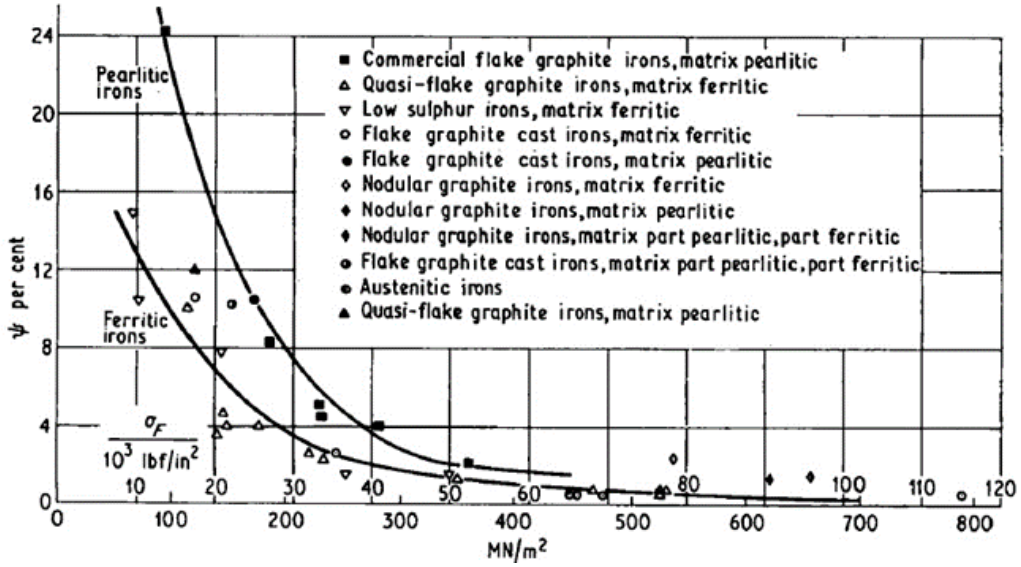


Figure 2 - 15. Damping capacity *vs.* the tensile strength of cast irons [98].

Table 2 - 3 presents the ranges of the loss factors (damping parameter to characterize the material damping capacity) of some cast irons [26, 30].

On the other hand, Al alloys present a lower damping capacity than cast irons [26], as also reported by Crăciun *et al.* [22] for high-purity Al (99.7%).

As reported before, the dominant factor of vibrational energy absorption and dissipation can be assigned to the movement of the dislocations. Therefore, a more effortless movement of the dislocations will result in a higher damping capacity since the vibrational energy can be absorbed and dissipated.

Specifically, in the case of cast irons, the damping capacity is attributed to the combined effect of graphite and matrix microconstituents, with particular relevance for the high intrinsic damping capacity of graphite, which seems to be more related to the morphology of the graphite precipitates than their fraction in the matrix [100-106].

In the meantime, the movement of the dislocations in the zones around the nodules of graphite, which is related to the matrix strength, is predominant regarding the SGI damping capacity [107].

Table 2 - 3. Damping capacity of cast irons at room temperature; adapted from [99] and presented in [30]

Cast irons	Composition (wt. %)	η (10^{-3})
Inoculated FGI	2.5 C; 1.9 Si; 1.0 Mn; 20.7 Ni; 1.9 Cr; 0.13 P	30.7
Non-inoculated FGI	3.3 C; 2.2 Si; 0.5 Mn; 0.14 P; 0.03 S	13.5
Inoculated FGI	3.3 C; 2.2 Si; 0.5 Mn; 0.14 P; 0.03 S	11.6
Austenitic FGI	2.5 C; 1.9 Si; 1.0 Mn; 20.7 Ni; 1.9 Cr; 0.03 P; 0.03 S	11.3
Alloyed FGI	3.14 C; 2.0 Si; 0.6 Mn; 0.7 Ni; 0.4 Mo; 0.14 P; 0.03 S	8.4
Ni-Cu austenitic FGI	2.55 C; 1.9 Si; 1.25 Mn; 15.2 Ni; 7.3 Cu; 2.0 Cr; 0.03 P; 0.04 S	6.2
Annealed ferritic SGI	3.7 C; 1.8 Si; 0.4 Mn; 0.76 Ni; 0.06 Mg; 0.03 P; 0.01 S; 0.003 Ce	4.5
Pearlitic malleable	BS 333/1961 grade B.33/4	2.5
Blackheart malleable	BS310/1958 grade B.22/14	2.4
As-cast pearlitic SGI	3.66 C; 1.8 Si; 0.4 Mn; 0.76 Ni; 0.06 Mg; 0.03 P; 0.01 S; 0.003 Ce	2.2

2.3.2.1.1. Impact of the graphite

The shape and fraction of graphite have a higher impact on the damping capacity of cast irons than the matrix or its interface with the graphite [108].

The damping capacity is higher for cast irons with lower nodularity; therefore, as already described, it decreases in the following order: FGI $\rightarrow$ CGI $\rightarrow$ SGI [50, 109].

Figure 2 - 16 shows that the addition of alloying elements, like Al, which influence the graphite structure, will, consequently, affect the damping capacity, which increases as the graphite transforms from spheroidal to compacted due to the increase of the graphite's surface area [73].

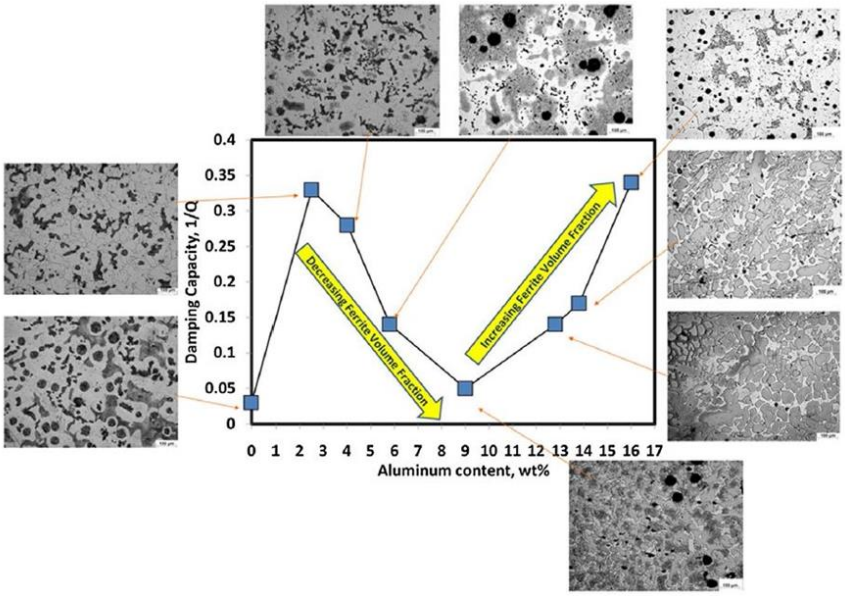


Figure 2 - 16. Effect of Al content on the damping capacity of cast irons [73].

In its turn, a reduction of the graphite fraction will induce a damping capacity decrease. Effectively, a higher C content slightly increases the damping capacity of SGI, potentially due to the increase of the fraction of graphite. Thus, when vibration causes an undesirable noise level and a high damping capacity is requested, it is better to use cast irons with high C content [19, 72, 73, 110].

Moreover, it is reported that the damping capacity increases with the graphite fraction and the size of the eutectic cells [109].

Different statements are listed in the literature concerning the influence of the nodule count on the damping capacity. Lin *et al.* [111, 112] observed a slight decrease in damping capacity with the increase in the nodule count. In contrast, studies by Damir *et al.* [113] point out the reverse, having registered an increase in the damping capacity with the decrease of the nodules size (*i.e.*, a higher nodule count). In the meantime, the studies of Carpenter *et al.* [114] pointed out that damping was essentially similar even for significant changes in the size of the graphite nodules.

As a final note, concerning the graphite impact on the damping capacity of cast irons, it should be stated that brake rotors are preferentially produced in FGI, presenting high fraction and long graphite flakes [98, 115-117].

2.3.2.1.2. Impact of the matrix

As already mentioned, graphite morphology strongly influences the damping capacity of cast irons, either by its shape, size, count, or fraction in the matrix. Moreover, the literature shows different statements regarding the matrix impact on the damping capacity for different graphite morphologies.

Regarding FGI, the matrix does not influence the damping capacity significantly. However, it could be optimized to obtain an FGI with high damping capacity and good mechanical properties since the matrix significantly affects the elastic modulus [119].

For an SGI, the highest damping capacity was obtained with a fully ferritic matrix in which the dislocations' movement is facilitated, improving the vibrational energy's dissipation [100, 107].

The impact of the fraction of ferrite in the matrix on the damping capacity can also be observed in Figure 2 - 16; it decreases due to the reduction of the fraction of ferrite and the precipitation of intermetallic compounds (FeAl, $AlFe_3C$ and Fe_3Al). The increase of the matrix hardness restrains its plastic flow. Consequently, a drastic decrease in the damping capacity is observed [73].

Moreover, it is also reported that a microstructural change, from a hard matrix (carbides and ferrite) to a soft matrix ("ferrite" - which the authors classified as a non-magnetic phase with Al in solution, and graphite) also increases the damping capacity (Figure 2 - 16) [73]. Takamori *et al.* [118] also reported that an increase in damping capacity might result from the magnetic transition, which occurred in the ferrite with 16% Al.

As a final comment relative to the microstructure impact on the damping capacity of cast irons, although Fox and Adams [98] have concluded that a high damping capacity can only be obtained at the expense of a loss in the tensile strength and ductility, Fujimoto and Hareyama [120] could produce SGI with high tensile strength as well as high vibration damping capacity. The authors have used Al as an alloying element; heat treatment and the alloying with Si, Sb or Sn also improved the vibration damping capacity.

2.4. Research methodology

As aforementioned, the main objective of this thesis was to develop an alloyed-SGI presenting a high damping capacity. However, keeping the tensile properties for the automotive components considered was mandatory.

The literature indicates that the impact of graphite morphology on damping capacity is higher than the matrix type; therefore, in the trials' plan, the alloying elements with influence either in the graphite shape and/or the matrix type were selected.

If a ferritic matrix induces a higher damping capacity and a CGI has a higher damping capacity than an SGI, then the most promising SGI should present a lower nodularity and a solution-hardened ferritic matrix to ensure the required mechanical properties. Therefore, the research involved developing and studying alloyed-SGI with slightly lower nodularity and solution-hardened ferritic matrix.

The selection of the alloying elements that were first tested was based on a literature survey (Table 2 - 4).

Table 2 - 4. List of the alloying elements selected for the preliminary trials

Element	**Impact**		
	Promotes non-spheroidal graphite	**Promotes an increase of ferrite fraction**	**Promotes an increase in strength**
Si	At high contents	Yes	Yes
Co	–	Yes	Yes
RE elements	At high contents	Yes	–
Al	Yes	–	–
Mo	To compare different types of matrices		
Cu			

– *unknown effect*

3. Experimental Methodology

Chapter 3 presents the experimental procedures followed in this work.

3.1. Materials' characterization

3.1.1. Strategic approach

The experimental approach for the materials' characterization was split into three major phases (Figure 3 - 1).

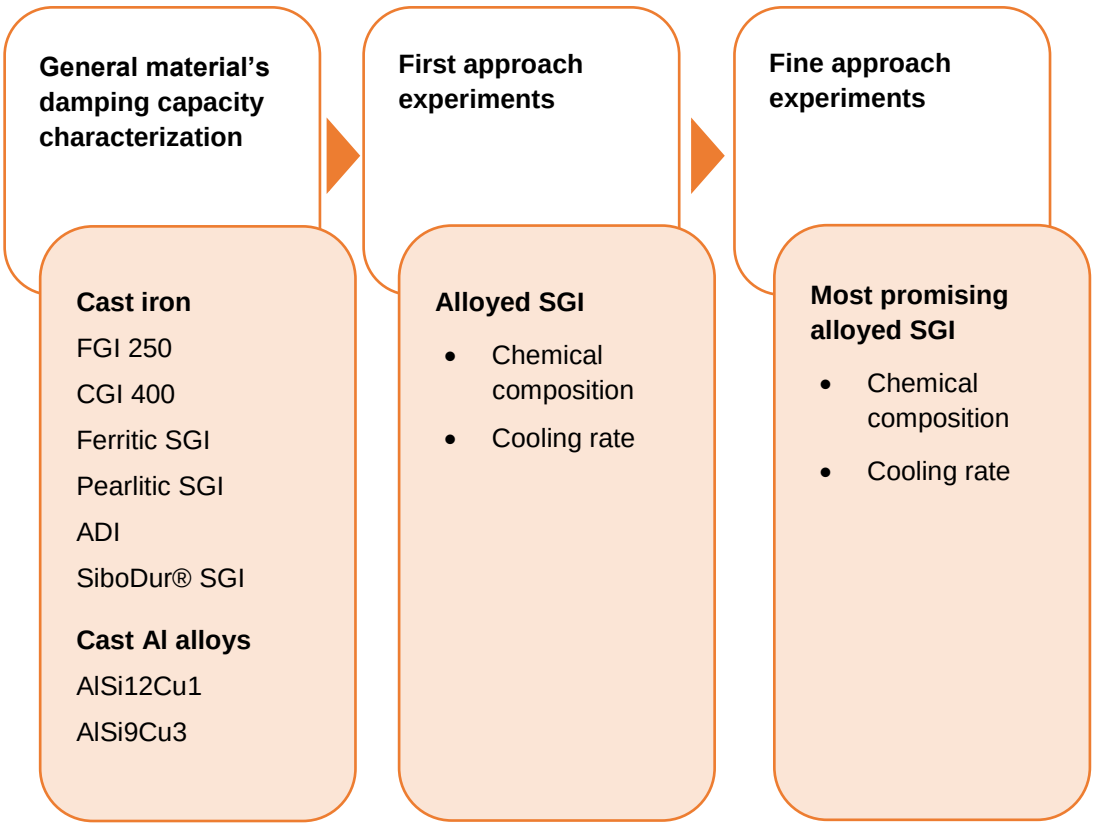


Figure 3 - 1. Schematic representation of the three major stages of the experimental approach for the materials characterization.

A general characterization of the material's damping capacity was first performed to evaluate the damping behaviour of different cast alloys with industrial application, namely: ferritic Spheroidal Graphite Iron (ferritic SGI: pearlite < 25%), pearlitic Spheroidal Graphite Iron (pearlitic SGI: 25 < pearlite < 100%), Flake Graphite Iron (FGI), Compacted Graphite Iron (CGI), Austempered Ductile Iron (ADI), SiboDur® alloyed SGI (Alloyed SGI-1: SiboDur® 450-17 (pearlite ≤ 20%) and Alloyed SGI-2: SiboDur® 700 (60 < pearlite ≤ 90%)) and two cast Al alloys (AlSi12Cu1 and AlSi9Cu3); these alloys were kindly supplied by industrial partners of CITNM.

Considering that this study focused on improving the damping capacity of SGI, the experiments (first and fine approaches) were developed only for this class of materials.

Alloyed SGI will be used to produce brake components (calliper and anchor). From evaluating the actual range of thicknesses of these components, the 45, 35, 25, 15 and 5 mm thicknesses were chosen for the step-castings used in the experiments. Their length and width (200 and 60 mm, respectively) were selected to machine, from each step, the test samples (for the dynamic, tensile and hardness tests, and microstructural analysis). The step-casting geometry (*see sub-chapter 3.1.2*) allowed us to study the impact of different cooling rates on those properties, especially the damping capacity.

Table 3 - 1 presents the step-casting thicknesses and the list of the alloying elements tested on the first and fine approaches experiments.

In the first approach, experiments have been planned based on the literature (*Chapter 2 – State of Knowledge*) and preliminary studies from the *Brake Noise* project. A group of alloying elements was selected to evaluate their influence on the SGI mechanical properties.

On the other hand, the selection of the alloying elements for the fine approach experiments was based on the most promising results from the first approach trials, as presented in sub-chapter 4.2.1.

Moreover, as realized in sub-chapter 4.2.1.1., the results show that the damping capacity is similar for the 45, 35 and 25 mm section thicknesses; therefore, only the samples from the 35 mm and 15 mm section thicknesses were considered for the fine approach experiments.

Table 3 - 1. Step-casting thicknesses and alloying elements tested in the first and fine approaches experiments performed on alloyed SGIs

	Step-casting thickness (mm)	Alloying elements	Trial's identification
First approach trials	45 35 25 15 5	Silicon	High Si
		Copper	Cu
		Molybdenum	Mo (x1*)
			Mo (x2*)
		Cobalt	Co (x1*)
			Co (x2*)
		Rare-Earth elements	RE (x1*)
		Aluminium	Al (x1*)
		Silicon, combined with Rare-Earth elements	High Si + RE (x0.5*)
			High Si + RE (x1*)
Alloying elements discarded		Cu, Mo	
Most promising alloying elements and combinations		Si, Co, RE, Al, Si + RE	
Fine approach trials	35 15	Cobalt combined with Cerium	Co + Ce (x0.5*)
			Co + Ce (x1*)
		Aluminium	Al (x5*)
	35	Silicon	High Si
		Silicon combined with Cerium	High Si + Ce (x0.5*)
		Silicon combined with Cerium and Cobalt	High Si + Ce (x0.5*) + Co

** Multiplicative factor*

3.1.2. Development of the castings for the experiments

The step-casting was developed by using *SolidWorks* and *SOLIDCAST* softwares. Several attempts were set in the models' design and simulation parameters to reduce the risk of shrinkage formation.

The dimensions of the step-castings can be seen in Figure 3 - 2; the gating and feeding system model is illustrated in Figure 3 - 3.

The step-castings (Figure 3 - 4) were only used for the first approach trials.

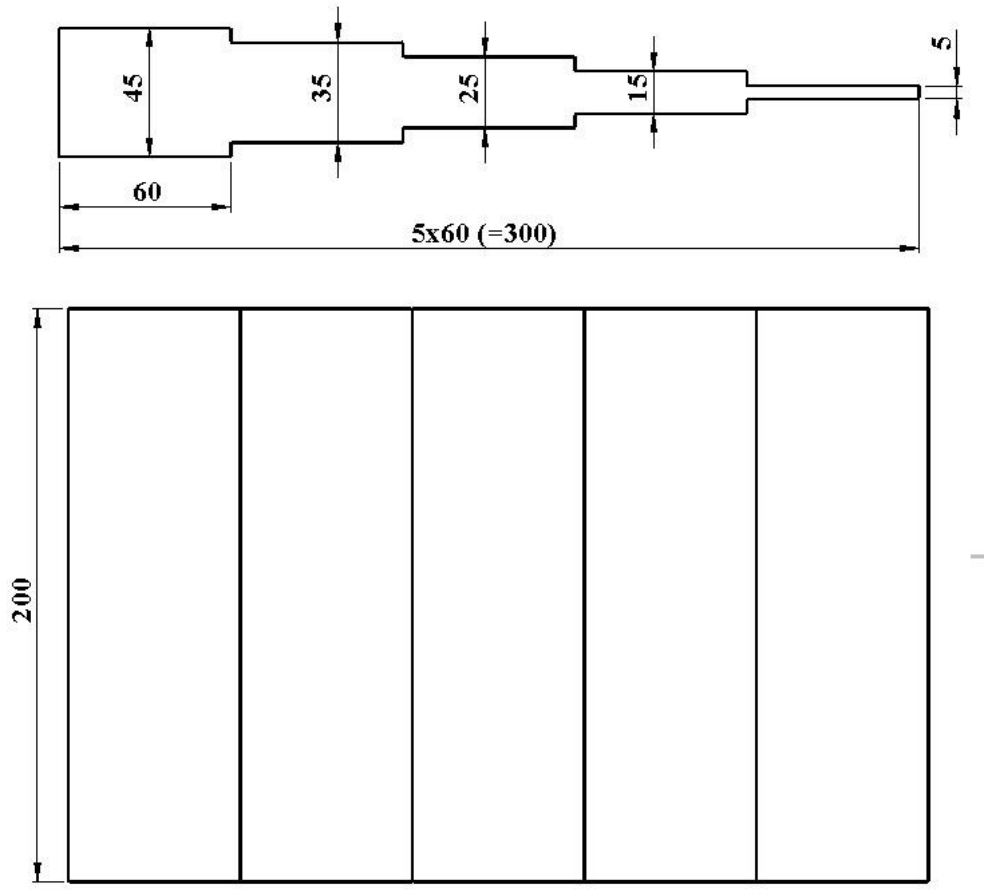


Figure 3 - 2. Dimensions (in mm) of the step-casting.

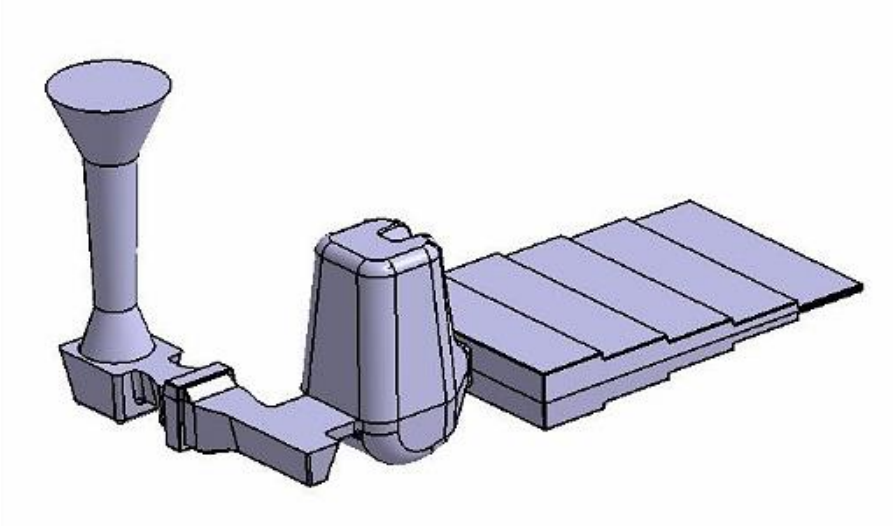


Figure 3 - 3. Step-casting's model and the respective gating and feeding system used for casting the different test samples.

Regarding fine approach trials, two prismatic samples (Figure 3 - 6) were used, whose dimensions were 35 x 60 x 200 mm and 15 x 60 x 200 mm.

It should be noted that it was attempted to determine the step-casting modulus (Annexe A). However, it was decided to use only the section thickness (ST) for all the comparative analyses.

A keel block was used for the Al-alloyed SGI since it was difficult to pour the step-casting due to problems related to the viscosity of the melt.

3.1.3. Melting procedure

3.1.3.1. First approach experiments

All the melts for the first approach experiments were prepared, at the laboratories of *AZTERLAN*, in a medium frequency induction furnace (250 Hz, 100 kW), with a maximum capacity of 100 kg. The charge for each heat (approximately 50 kg) comprised 22 kg of SGI returns and 28 kg of high-grade pig iron. Predetermined masses of a commercial graphite (98.9% C, 0.03% S) and FeSi alloy (74.6% Si, 0.3% Ca, 0.7% Al) were also added to the metallic charge.

After melting, the chemical composition of the metal was controlled by emission spectrometry and adjusted according to the final target. After being superheated to 1500ºC, the melt was transferred into the pouring ladle for the nodularizing treatment with 0.55 kg (1.1 wt.% of the mass of the melt) of a FeSiMg alloy (47.2% Si, 6.02% Mg, 1.15% Ca, 0.24% Al, 0.3% Mn and 0.88% RE) by the sandwich process. The FeSiMg alloy was placed at the bottom of the ladle and then covered with steel scrap before tapping the melt from the furnace.

The melts were poured into self-setting sand moulds and directly inoculated in the mould by adding 0.2 wt.% (of the mass of the melt) of a FeSi inoculant block (71.7% Si, 3.93% Al and 0.99% Ca).

For the first approach experiments, only one base SGI melt was produced for all heats; it was assumed that the chemical composition of the

base charge was the same since the raw materials and respective masses were always the same.

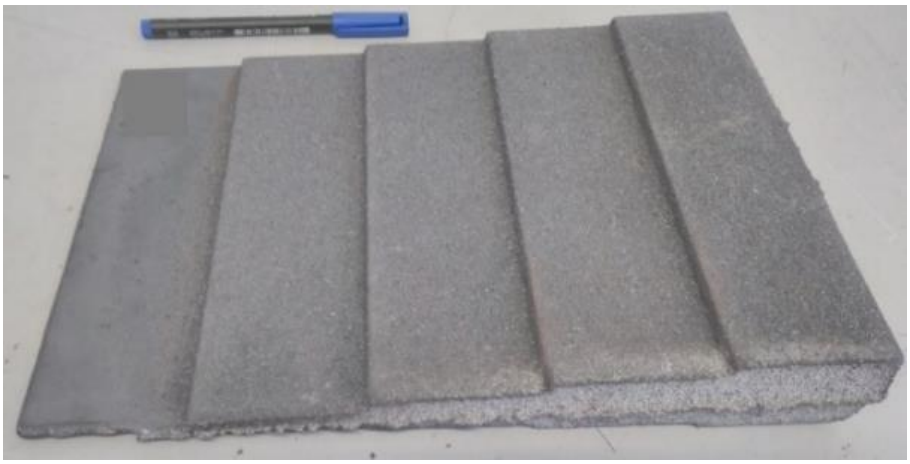


Figure 3 - 4. Image of a step-casting from the first approach experiments with 45, 35, 25, 15 and 5 mm section thicknesses.

The flowchart for the first approach experiments is presented in Figure 3 - 5.

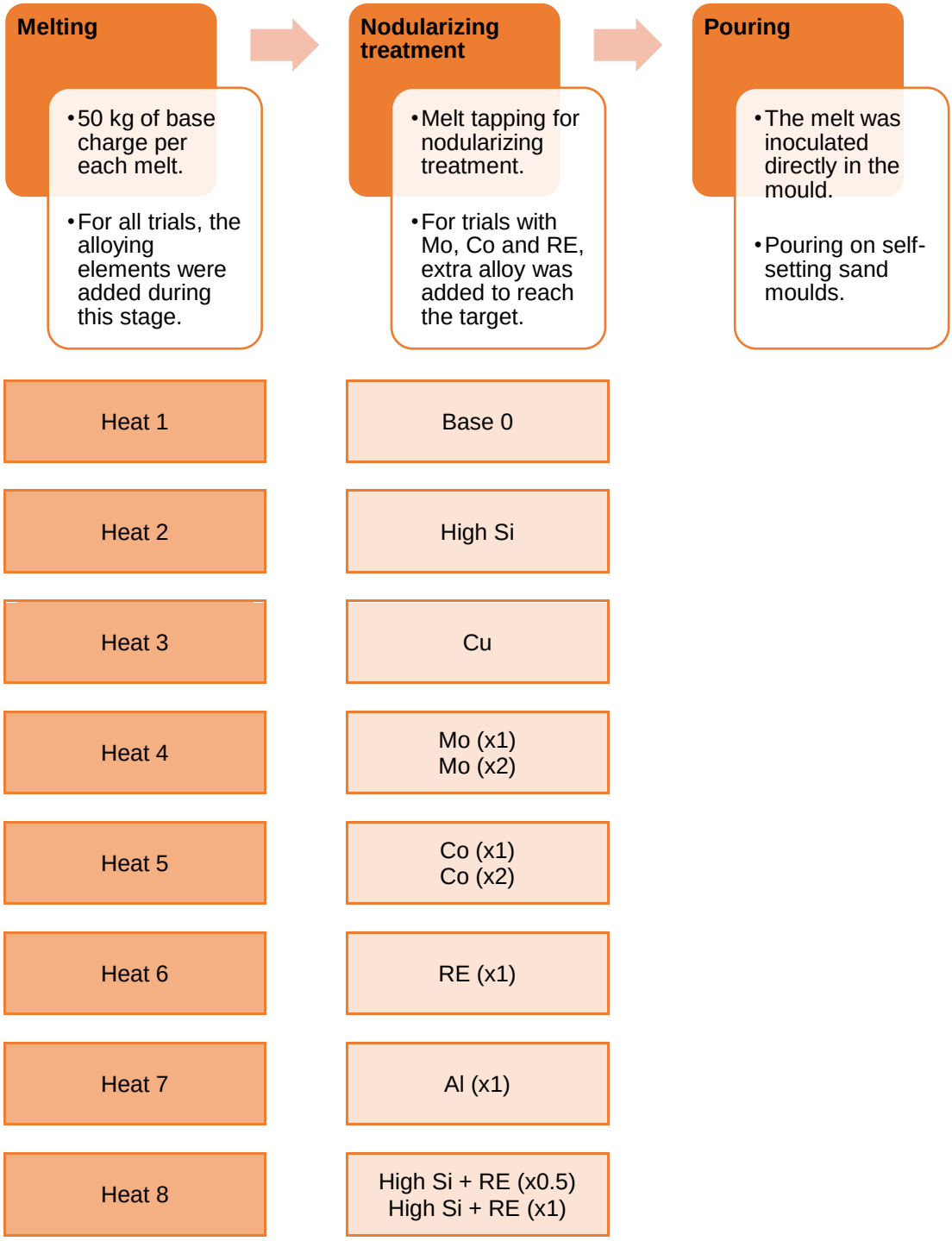


Figure 3 - 5. Flowchart relative to the first approach experiments[3].

[3] The chemical compositions of the melts from the first approach experiments are presented in Table 4 - 1 (*sub-chapter 4.2.1*).

3.1.3.2. Fine approach experiments

In turn, the melts for the fine approach experiments were prepared, at the laboratories of CINFU, in a 100 kg induction furnace (3200 Hz, 75 kW). The charge for each heat consisted of 45 kg of SGI returns and 50 kg of steel scrap. Predefined masses of commercial graphite and FeSi alloy were also added to the metallic charge.

After melting, the chemical composition of the metal was also controlled and adjusted according to the final target. After being superheated to approximately 1460ºC, the melt was transferred into the pouring ladle for the nodularizing treatment with 0.8 kg (1.6 wt.% of the mass of the melt) of a FeSiMg alloy (45.44% Si, 6.57% Mg, 1.64% Ca, 0.65% Al, 0.8% Ce and 1.38% RE) by the sandwich process.

The nodularizer was deposited at the bottom of the ladle and then covered with steel scrap before tapping the melt from the furnace. FeSi inoculant (63.1% Si, 1.21% Ca, and 0.99% Al) was also placed at the bottom of the ladle; 0.2 kg (0.5 wt.% of the mass of the melt) of inoculant was added. All additions to the melt were adjusted, from batch to batch, to ensure the chemical composition envisaged.

The melts were poured into green sand moulds with prismatic geometry (Figure 3 - 6). These castings were used only for the fine approach experiments.



Figure 3 - 6. Image of a casting from the fine approach experiments with 35 and 15 mm section thicknesses.

As previously mentioned, the procedure was slightly different from the first approach experiments; the flowchart for the trials is presented in Figure 3 - 7.

In this approach, for each heat, one base sample was produced.

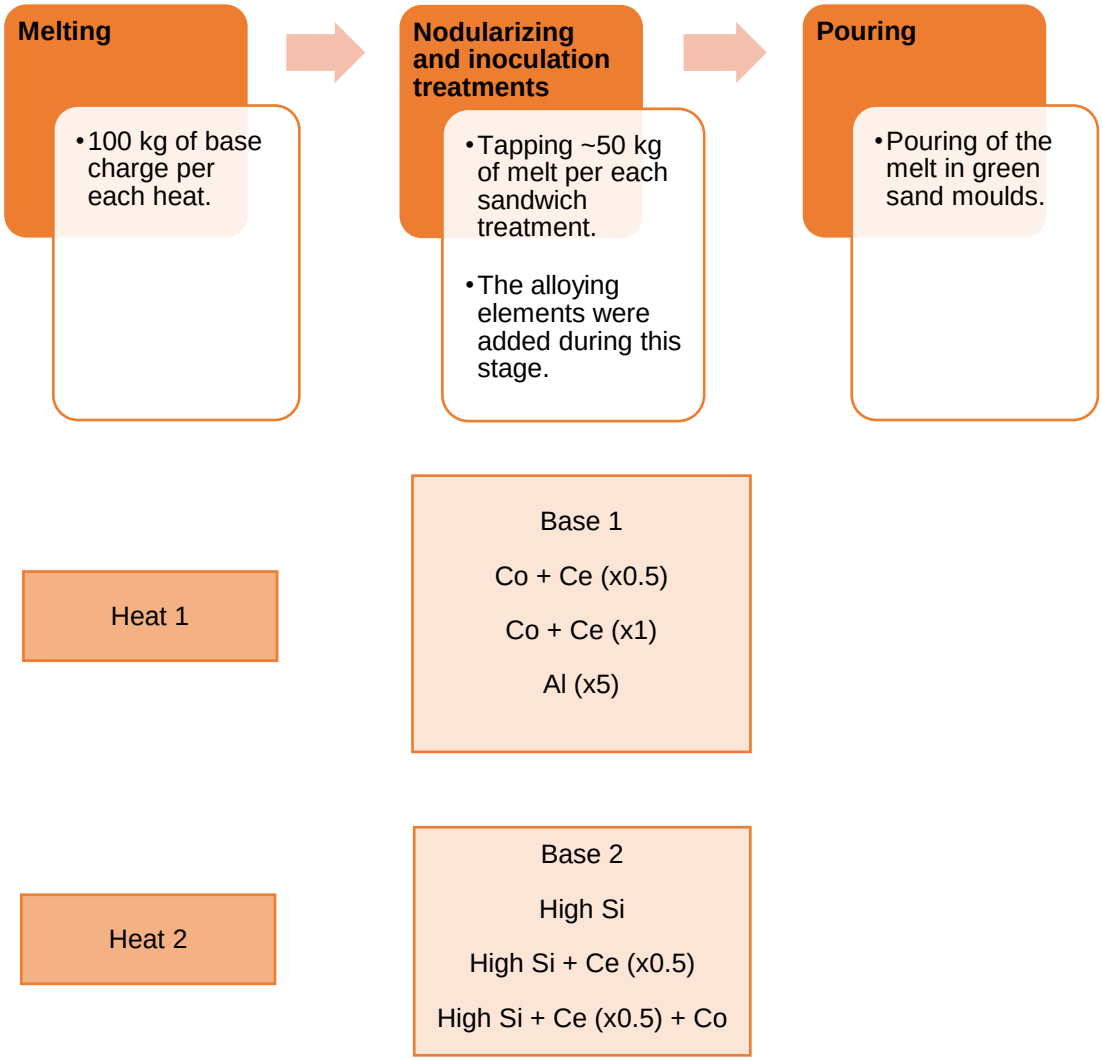


Figure 3 - 7. Flowchart relative to the fine approach experiments[4].

[4] The chemical compositions of the melts from the fine approach experiments are presented in Table 4 - 34 (*sub-chapter 4.2.2*).

3.1.4. Experimental procedures

3.1.4.1. Porosity control and cutting of castings

All castings were analysed by X-ray to verify the eventual presence of porosity that could influence the experimental results.

Figure 3 - 8 shows a schematic representation of the methodology used to get the samples from the different steps of the castings.

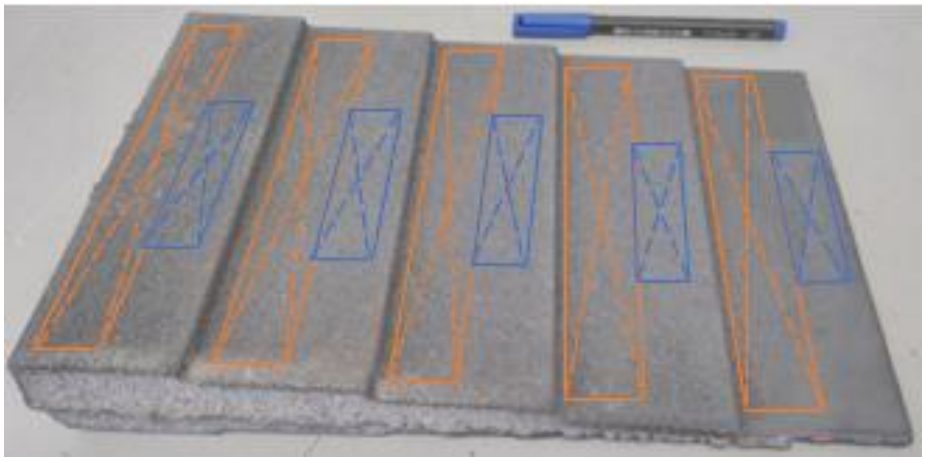


Figure 3 - 8. Image of one of the step-casting produced, indicating the zones from where the different samples have been removed for: tensile tests (in orange), microstructural analysis, damping and hardness tests (in blue).

3.1.4.2. Microstructural analysis

The metallographic preparation of the samples used for the microstructure characterization is presented in Table 3 - 2.

Table 3 - 2. Procedures for the metallographic preparation of the samples

Grinding	
SiC papers	**Time of preparation (s)**
120/180 mesh	10-30
320 mesh	
600 mesh	
1000 mesh	
Intermediate cleaning	
Washed in a water stream with soap and dried with paper	
Polishing	
Cloths	**Time of preparation (min.)**
6 μm diamond suspension	1-7
1 μm diamond suspension	1-3
Finishing cleaning	
Washed in a water stream with soap, dried with hot air, and, finally, surface's cleaning with ethanol	

The analysis of the graphite particles was performed on unetched samples. To analyse the other microconstituents, such as ferrite, pearlite and potentially carbides, the samples were previously etched with Nital 2% (98% ethanol and 2% nitric acid); the etching time varied between 5 and 10 s.

The samples were observed by Light Optical Microscopy (LOM) using a *Leica DM 4000M* microscope.

The *Automatic* (from *LAS – Leica Application Suite*) software was used to analyse the graphite precipitates, which allowed us to determine the following parameters:

- particles fraction;
- nodularity, which was determined based on Equation 8 (*sub-chapter 2.3.1.*);
- particles count per unit area, taking into account the graphite particles with all forms;

- convex perimeter, which is derived from the Feret diameter and approaches the perimeter of the enclosing polygon (Figure 3 - 9).

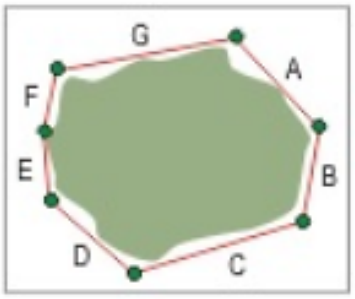


Figure 3 - 9. Example of estimating the convex perimeter of a graphite particle [121].

Considering the ISO 945-2 standard [122], only the particles with area ≥ 25 μm^2 and length > 5 μm were considered to initiate the data treatment. Figure 3 - 10 presents an example of estimating the length of a graphite's particle.



Figure 3 - 10. Estimating the length of a graphite particle [121].

The fraction of pearlite was determined by visual comparison with reference images from ISO 945-3 standard [123]. All the microstructural data correspond to an average of the results from 10 fields, at 100x magnification.

Additionally, Scanning Electron Microscopy with Energy Dispersive Spectroscopy (SEM/EDS), and Electron Probe Micro-Analyser (EPMA) were used to perform an in-depth study of some samples.

SEM consists of focusing an electron beam into a fine probe and scanning it over a rectangular area of the sample's surface. The beam interacts with the sample, creating various signals that characterize the sample in terms of chemical composition, the morphology of the constituents, and surface

topography. X-rays are of significant interest in SEM, allowing the semi-quantitative analysis of the sample [124, 125].

The technique EPMA allows an elemental analysis by bombarding a sample with a focused beam of energetic electrons, which will induce the emission of characteristic X-rays. The analysis of the X-ray spectra will allow quantitative and qualitative chemical analysis. EPMA enables the visualization of the spatial distribution of the different components by X-ray area scans (qualitatively) and by digital compositional maps (quantitatively) [124, 125].

3.1.4.3. Tensile tests

To evaluate the mechanical properties, two geometries of samples had to be considered due to the restrictions of machining the different sections of the step-castings.

Cylindrical samples were machined from each section with 45 to 15 mm thickness, with dimensions according to DIN EN 1563: 2011. On the other hand, for the 5 mm thick section, as it was impossible to prepare samples with cylindrical geometry, prismatic ones were machined, according to NP EN ISO 6892-1: 2009. The tensile tests were performed according to EN ISO 6892-1: 2016 B.

For section thicknesses from 45 to 15 mm, all the results correspond to an average from two tensile tests, while, regarding the 5 mm thick section, only one trial was considered.

3.1.4.4. Hardness tests

Brinell hardness tests were performed with a cemented carbide ball of 2.5 mm diameter on a *DuraVison 20* equipment. A load of 62.5 kgf was used for hardness values up to 140 HBW and 187.5 kgf for those above 140 HBW. The Brinell hardness tests were performed according to EN ISO 6506-1: 2009.

The hardness values correspond to an average from seven indentations performed in each sample.

3.1.4.5. Impulse Excitation Technique tests

Damping capacity was determined using a Resonant Frequency and Damping Analyser (RFDA), Figure 3 - 11, based on the Impulse Excitation Technique. This equipment allows the determination of the internal friction and natural frequencies and the calculation of the elastic properties (Young's modulus, shear modulus and Poisson's ratio).

In this work, the damping capacity was characterized by internal friction in flexural mode.

One prismatic test sample was machined, from each section thickness, with dimensions of 3 x 20 x 60 mm, according to ASTM E1876-15 and the recommendations of the equipment's manufacturer.

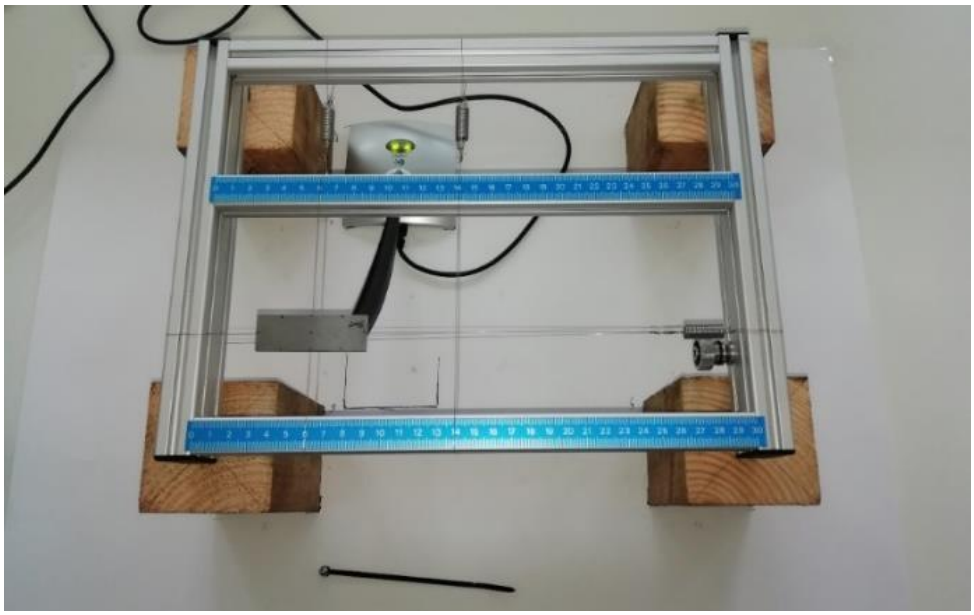


Figure 3 - 11. Resonant Frequency and Damping Analyser (RFDA) equipment.

The tests were performed at room temperature, according to ASTM E1876-15 (Table 3 - 3). All the fundamental frequencies and internal friction results correspond to an average of fifteen tests performed over each sample. This number of trials was selected based on the study of the dispersion of the results (*sub-chapter 3.1.4.6.3*). On the other hand, the results

average three tests for the elastic properties (Young's modulus, shear modulus and Poisson's ratio).

It is worth noting that the damping values obtained in this work were used for comparative analysis between samples tested on the same equipment; values may change if a different technique is used.

Table 3 - 3. Methodology for the Impulse Excitation Technique tests

Sample's preparation	
Step 1	Cleaning of the surface with ethanol
Step 2	Determination of the dimensions (length, width and thickness) of the samples at three different points using a digital pachymeter
Step 3	Identification of the nodes' guidelines
Step 4	Determination of the samples' weight in a digital balance
Step 5	Poisson's ratio was estimated using the *GRANTA EduPack* software

Tests	
Step 6	Introduction of the dimensions and weight of each sample, an estimated Poisson's ratio, and their variations in the RFDA basic software
Step 7	The test specimen is mechanically excited through a single-elastic strike, using an impulse tool to promote its vibration in each of the selected modes
Step 8	The transducer (a microphone) detects the sound produced by the vibration of the specimen, and then the signals are analysed
Step 9	The software analyses the signals and presents the results

Selected mode	Methodology	Results
Flexural & Torsion	A first test is performed to obtain the effective Poisson's ratio to be reintroduced in the RFDA basic software	Young's modulus, E (GPa) Shear modulus, G (GPa) Poisson's ratio, σ_1
Flexural	Tests are performed until five consecutive readings are obtained, which lie within a 1% variation	Fundamental frequency (Hz) Internal friction, Q^{-1}
Flexural & Torsion	Tests are performed until $\frac{\sigma_2 - \sigma_1}{\sigma_2} < 0.02$	Young's modulus, E (GPa) Shear modulus, G (GPa) Poisson's ratio, σ_2

3.1.4.6. Results dispersion

A study of the variation of the technique was conducted to evaluate the dispersion associated with the tensile, hardness and damping tests. The coefficient of variation (CV) was used as the dispersion measurement to perform this assessment.

3.1.4.6.1. Tensile tests

The coefficient of variation for each mechanical property (ultimate tensile strength, 0.2% offset yield strength and elongation) evaluated corresponds to an average of the coefficient of variation obtained from the tensile tests performed with cylindrical samples produced by the project's partner *AAPICO* (Table 3 - 4).

Table 3 - 4. Coefficient of variation for each of the mechanical properties obtained from the tensile tests

	Ultimate tensile strength (MPa)	**0.2% offset yield strength (MPa)**	**Elongation (%)**
CV estimated (%)	*± 7*	*± 6*	*± 6*

To evaluate the influence of their geometry on the results, two samples were machined from the same step-casting (produced from the base SGI); the results from the tensile tests are presented in Table 3 - 5.

Table 3 - 5. Results from the tensile tests for two samples with different geometries

	Prismatic sample (from a section with 5 mm thickness)	**Cylindrical sample** (from sections with 15-45 mm thickness)
Tensile strength (MPa)	391	385
CV estimated (%)	*± 1*	
0.2% offset yield strength (MPa)	263	254
CV estimated (%)	*± 2*	
Elongation (%)	17.2	23.7
CV estimated (%)	*± 16*	

Taking into account the data from Table 3 - 5, the tensile and the 0.2% offset yield strengths of the test samples with different geometries were considered analogous. This was assumed since, in both cases, the coefficients of variation of the results for different geometries are lower than the coefficients of variation obtained from a deep study of the results compiled from the regular production from *AAPICO* (7% for the ultimate tensile strength and 6% for the 0.2% offset yield strength).

Regarding elongation, the coefficient of variation for the results obtained for different geometries was relatively high (16%). After an analysis of the data, all the results for the 5 mm section thickness were discarded, and a new and more reasonable coefficient of variation was obtained (6%).

Concluding, the coefficient of variation for each of the mechanical properties evaluated in this thesis will be:

- ultimate tensile strength: ± *7%*;
- 0.2% offset yield strength: ± *6%*;
- elongation: ± *6%*.

3.1.4.6.2. Hardness tests

The coefficient of variation for the hardness tests was obtained from the experiments performed with castings from *AAPICO*; the value ±*5%* was assumed (Table 3 - 6).

Table 3 - 6. Coefficient of variation calculated for the hardness tests

	Hardness (HBW)
CV estimated (%)	*± 5*

3.1.4.6.3. Damping capacity tests

Three approaches were used to determine the coefficient of variation for the damping capacity tests:

1. All tests were repeated three times
   Objective: Verify the deviation from different experiments.
   Fifteen tests were carried on for each sample (repeated three times multiplied by the five consecutive damping readings considered in each test);
2. Six samples were machined from different section thicknesses of the base SGI
   Objective: Analyse the variation of the damping values for the same material.
3. Two samples with higher dimensions were machined (prismatic test samples with dimensions of 5 x 25 x 80 mm)
   Objective: Examine the influence of the variation of the samples' dimensions.

The coefficients of variation for the results of the damping capacity, fundamental flexural frequency and Poisson's ratio are presented in Table 3 - 7 through Table 3 - 9.

Table 3 - 7. Coefficient of variation of the results for the damping capacity tests

	Section with 45 mm thickness			
	Sample with lower dimensions			**Sample with higher dimensions**
	Sample I	**Sample II**	**Sample III**	
CV estimated (%)	± *1*			
	Section with 35 mm thickness			
	Sample with lower dimensions			**Sample with higher dimensions**
	Sample I	**Sample II**	**Sample III**	
CV estimated (%)	± *1*			

Obs: the results are relative to eight samples analysed three times each

Table 3 - 8. Coefficient of variation of the results for the fundamental flexural frequency

	Section with 45 mm thickness			
	Sample with lower dimensions			Sample with higher dimensions
	Sample I	Sample II	Sample III	
CV estimated (%)	± *0.004*			
	Section with 35 mm thickness			
	Sample with lower dimensions			**Sample with higher dimensions**
	Sample I	**Sample II**	**Sample III**	
CV estimated (%)	± *0.004*			

Obs: the results are relative to eight samples analysed three times each

Table 3 - 9. Coefficient of variation of the results for the Poisson's ratio

	Section with 45 mm thickness			
	Sample with lower dimensions			Sample with higher dimensions
	Sample I	Sample II	Sample III	
CV estimated (%)	± *0.04*			
	Section with 35 mm thickness			
	Sample with lower dimensions			**Sample with higher dimensions**
	Sample I	**Sample II**	**Sample III**	
CV estimated (%)	± *0.06*			

Obs: the results are relative to eight samples analysed three times each

Concluding, the coefficients of variation that will be considered for the results of the IET tests are:

- ± *1%* for the damping capacity;
- ± *0.004%* for the fundamental flexural frequency;
- ± *0.06%* for the Poisson's ratio.

For the Young's and shear modulus results, the variance values assumed by the software (only possible for these properties) will be used.

3.1.4.7. Multiple linear regression analysis

Multiple linear regression analysis was applied to establish an empirical formula correlating the damping capacity (dependent variable or outcome) with the significant microstructural features expected to affect it (independent variables or predictors). A simple linear regression was not used as more than one microstructural feature is expected to influence damping capacity.

The Statistical Package for the Social Sciences software (SPSS Statistics) was used to develop the model for estimating the SGI damping capacity.

Multiple linear regression analysis is based on several assumptions that need to be fulfilled, namely:

1. Sample size rule – At least ten cases per independent variable;
2. No multicollinearity – independent variables are not highly correlated with each other. Tolerance > 0.1 or Variance Inflation Factor (VIF) < 10;
3. No outliers – Standard predicted and standard residual values between -3 and +3;
4. Multivariate normality – residuals are normally distributed;
5. Homoscedasticity – the variance of error terms is similar across the values of the independent variables;
6. Linear relationship – between the dependent and independent variables.

After analysing the fulfilment of several assumptions, it is necessary to examine the significance of the model; in this thesis, a correlation higher than 70% ($R^2 > 0.7$) was considered strong.

Then, a model was developed with the constants associated with each predictor variable, and an empirical formula was established. It is essential to verify if a predictor influences (negatively or positively) the dependent variable.

The standardized coefficient (β) was evaluated to verify the influence of each predictor in the dependent variable. For instance, if a predictor presents a higher standardized coefficient than another, a variation of its values will have a higher impact on the dependent variable.

4. Experimental Results

Chapter 4 presents the relevant results obtained in this work.

4.1. Damping capacity of different standard cast alloys

The damping capacity of different standard cast alloys was determined to set a comparative analysis with the SGI produced by *AAPICO*, the industrial partner of the *Brake Noise* project, and benchmark the alloys under development.

As already mentioned, the alloys involved in this study were: ferritic and pearlitic Spheroidal Graphite Iron (SGI), Flake Graphite Iron (FGI 250), Compacted Graphite Iron (CGI 400), Austempered Ductile Iron (ADI), two SiboDur® alloyed SGIs (450-17 and 700), and two Al alloys (AlSi12Cu1 and AlSi9Cu3); as previously mentioned, these alloys were kindly supplied by industrial partners of CITNM.

Figure 4 - 1 presents the variation of the damping capacity for these alloys relatively to the ferritic and pearlitic SGIs produced by *AAPICO*. The highest damping capacity was obtained for FGI, whereas the lowest was for AlSi12Cu1.

A deeper analysis of the results will be presented in Chapter 5.

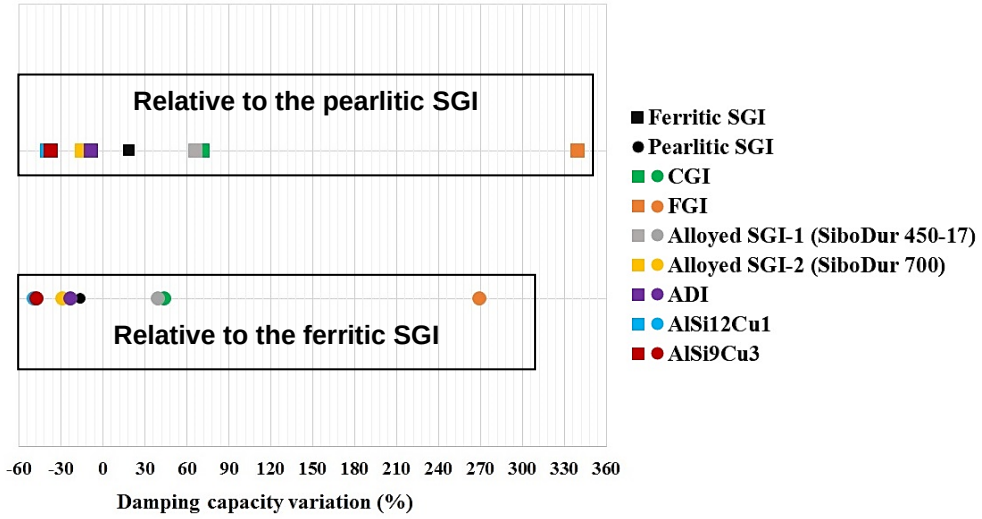


Figure 4 - 1. Variation of the damping capacity of different cast alloys relative to the ferritic and pearlitic SGIs produced by *AAPICO*.

4.2. Alloyed spheroidal graphite irons

4.2.1. First approach experiments

From the analysis of the variation of the damping capacity for different cast alloys relatively to the SGI produced by *AAPICO* (Figure 4 - 1), we conclude that the ferritic SGI presents a higher damping capacity than the pearlitic SGI, and that compacted or flake graphite enhances damping capacity.

As already described, the literature also states that both graphite morphology and their matrix influence the damping capacity of cast irons, which increases with the fraction of ferrite and the decrease of nodularity.

As presented in the research methodology (*sub-chapter 2.4.*), the main goal of the work was to develop an SGI with higher damping capacity by decreasing the nodularity and strengthening the ferritic matrix to keep, as much as possible, the other mechanical properties. Hence, a set of alloyed SGIs was developed by adding alloying elements that would increase the fraction of ferrite (Si or Co) or decrease the nodularity (Si and RE elements). Moreover, pearlitic SGIs (Cu or Mo) were studied for relative comparison.

Table 4 - 1 presents the chemical composition of the SGI melts produced for the first approach experiments; Carbon Equivalent (C.E.) was calculated from Equation 9 (*sub-chapter 2.3.1.2.*).

The chemical composition identified as Base 0 (Table 4 - 1) corresponds to a standard ferritic-pearlitic SGI, which was used as a reference to analyse the impact of the alloying elements on the damping capacity of the different SGIs produced.

The microstructures, and the mechanical properties and the data relative to the microstructural analysis of this reference are presented in Figure 4 - 2 and Table 4 - 2, respectively.

Table 4 - 1. Chemical composition of the SGI melts produced for the first approach experiments

	Chemical composition (wt.%)										
	Base 0	**High Si**	**Cu**	**Mo (x1)**	**Mo (x2)**	**Co (x1)**	**Co (x2)**	**RE (x1)**	**Al**	**High Si + RE (x0.5)**	**High Si + RE (x1)**
C	3.79	3.48	3.71	3.79	3.76	3.77	3.74	3.69	3.64	3.38	3.37
Si	2.04	**3.64**	2.18	2.23	2.26	2.27	2.3	2.25	2.29	**3.38**	**3.37**
Mn	0.14	0.16	0.15	0.15	0.18	0.16	0.18	0.16	0.17	0.2	0.2
P	0.007	0.014	0.013	0.012	0.013	0.019	0.015	0.014	0.023	0.022	0.016
S	0.005	0.007	0.006	0.007	0.007	< 0.005	0.005	0.007	< 0.005	< 0.005	0.005
Mg	0.036	0.041	0.043	0.042	0.044	0.044	0.042	0.047	0.041	0.047	0.046
Cu	0.02	0.03	**0.39**	< 0.02	< 0.02	< 0.02	< 0.02	< 0.02	0.024	< 0.02	< 0.02
Mo	0.01	0.01	0.01	**0.29**	**0.57**	0.042	0.028	< 0.01	<0.01	< 0.01	< 0.01
Co	0.006	–	–	0.045	0.044	**2.38**	**4.26**	0.009	0.006	< 0.005	0.005
Ce	–	–	–	–	–	–	–	**0.032**	–	**0.016**	**0.030**
La	–	–	–	–	–	–	–	**0.016**	–	**0.008**	**0.015**
Cr	0.02	0.03	0.03	< 0.03	0.04	< 0.03	0.03	0.03	< 0.03	0.03	0.04
Al	< 0.01	< 0.01	< 0.01	< 0.01	< 0.01	–	–	< 0.01	**3.32**	< 0.01	< 0.01
C.E.	*4.5*	*4.7*	*4.4*	*4.5*	*4.5*	*4.5*	*4.5*	*4.4*	*4.4*	*4.5*	*4.5*

Obs: C.E. calculated from Equation (9) (sub-chapter 2.3.1.2.)

The content of the alloying element(s) that qualify each trial is highlighted in bold

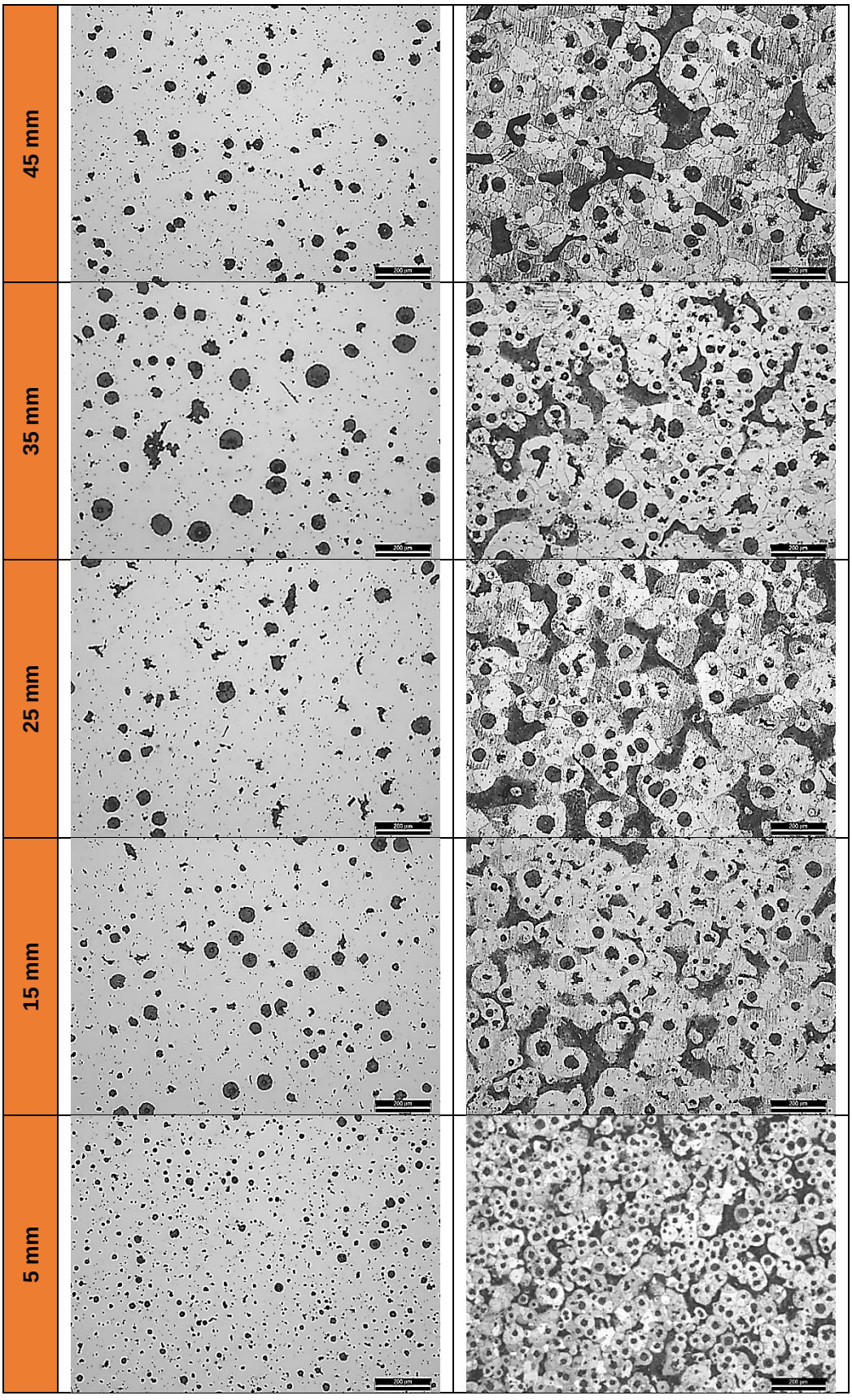


Figure 4 - 2. LOM micrographs of the Base 0 SGI, for the first approach experiments, for different section thicknesses.

Table 4 - 2. Results of the tests performed on the Base 0 SGI samples for the first approach experiments

Section thickness (mm)	5	15	25	35	45
Damping capacity	0.000265	0.000338	0.000376	0.000394	0.000421
CV estimated (%)	*± 1*				
Fundamental flexural frequency (Hz)	4250	4226	4235	4223	4225
CV estimated (%)	*± 0.004*				
Young's modulus (GPa)	178	178	177	175	175
CV estimated (%)	*± 1.2*	*± 1.3*	*± 1.1*	*± 1.2*	*± 1.2*
Shear modulus (GPa)	70	70	69	69	69
CV estimated (%)	*± 0.5*	*± 0.5*	*± 0.4*	*± 0.5*	*± 0.5*
Poisson's ratio	0.269	0.276	0.272	0.271	0.270
CV estimated (%)	*± 0.06*				
Ultimate tensile strength (MPa)	529	432	402	389	387
CV estimated (%)	*± 7*				
0.2% offset yield strength (MPa)	333	288	274	258	260
CV estimated (%)	*± 6*				
Elongation (%)	11.3	18.3	18.8	20.4	20.0
CV estimated (%)	*± 6*				
Hardness (HBW 2.5/*) *62.5: ≤ 140 HBW or 187.5: > 140 HBW	159	138	149	131	131
CV estimated (%)	*± 5*				
Pearlite (%)	25	25	25	25	20
Graphite (%)	5.3	7.2	7.4	9.6	7.3
Nodularity (%)	86	80	75	84	79
Nodule count (particles/mm^2)	373	164	204	194	130
Convex perimeter (µm)	40	66	55	64	72
Graphite form-III (%)	1.9	7.0	10.7	5.6	7.2

4.2.1.1. Evaluation of the first approach experiments

A first evaluation of the mechanical properties of all the SGI castings produced for the first approach experiments was developed based on the mean value of the results obtained, independently of the section thickness of the step-castings produced.

It should be noted that, although a casting usually presents different section thicknesses, it was relevant to evaluate, in the first approach analysis, the overall impact of the melt composition on the SGIs' mechanical properties.

The results were categorized as improved (+), decreased (–), or unaltered (=), according to the values of the Coefficient of Variation (CV) obtained and those estimated (*sub-chapters 3.1.4.6.1. and 3.1.4.6.3.*), as sketched in Figure 4 - 3.

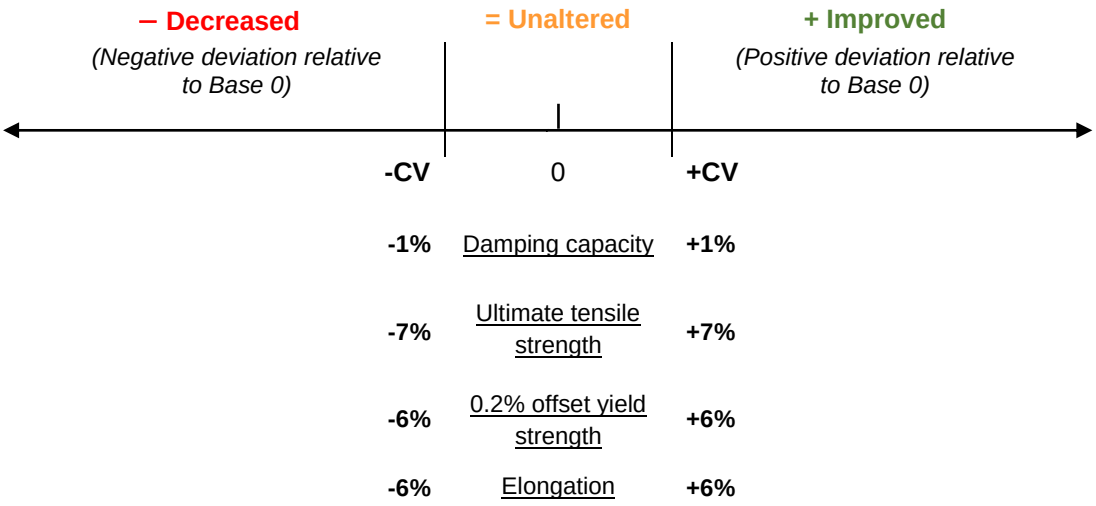


Figure 4 - 3. Base methodology for categorizing the results of the mechanical properties of all the SGI castings from the first approach experiments.

Table 4 - 3 synthesizes the comparative evaluation of the mechanical properties of all the SGI castings produced for the first approach experiments.

An overall improvement of the damping capacity was registered, without a significant decrease in the tensile properties, for the following compositions: High Si, Co (x1), Co (x2), High Si + RE (x0.5) and High Si + RE (x1).

The next four sub-chapters present all the results associated with damping capacity improvement; the results of the remaining trials, for which no improvement was registered, are set out in Annexe B.

Table 4 - 3. Comparative evaluation of the mechanical properties of the SGI castings from the first approach experiments

	Damping capacity	Young's modulus	Ultimate tensile strength	0.2% offset yield strength	Elongation
High Si	+	–	+	+	+
Co (x1)	+	=	+	+	+
Co (x2)	+	=	+	+	=
High Si + RE (x0.5)	+	–	+	+	+
High Si + RE (x1)	+	–	+	+	+
RE (x1)	=	=	=	=	+
Mo (x1)	–	=	+	+	–
Mo (x2)	–	=	+	+	–
Al	–	–	+	+	–
Cu	–	=	+	+	–

– Decreased *= Unaltered* *+ Improved*

4.2.1.1.1. High Si-alloyed SGI

High Si-alloyed SGI was tested since the literature establishes that Si is a strong ferritizer and promotes a solid solution strengthening of the ferrite, allowing it to attain hardness and strength similar to the SGI ferritic-pearlitic grades [58]. High Si contents also promote the formation of degenerated graphite, such as chunky graphite.

Figure 4 - 4 shows the microstructures of the High Si-alloyed SGI; the nodules of graphite are distributed in a fully ferritic matrix (*i.e.*, pearlite < 5%) for all the section thicknesses, confirming the ferritizing effect of Si (the microstructures presented in Figure 4 - 4 should be confronted with those in Figure 4 - 2, from the Base 0 SGI). Besides, the samples present a higher fraction of graphite, nodularity and nodule count (Table 4 - 4) than the Base 0 SGI (Table 4 - 2).

Now, it will be relevant to analyse the impact of the increase of the fraction of ferrite and nodularity on the damping capacity of these samples; an improvement was registered for the section thicknesses between 5 and 25 mm (Figure 4 - 5 and Table 4 - 5).

Considering the results obtained, it is interesting to notice that, for fully ferritic matrices, the damping capacity is mainly dependent on graphite morphology variations. However, it is essential to emphasize that the damping capacity relies not only on one microstructural feature, such as nodularity, which will be confirmed later in the model developed to estimate the damping capacity (sub-chapter 5.2).

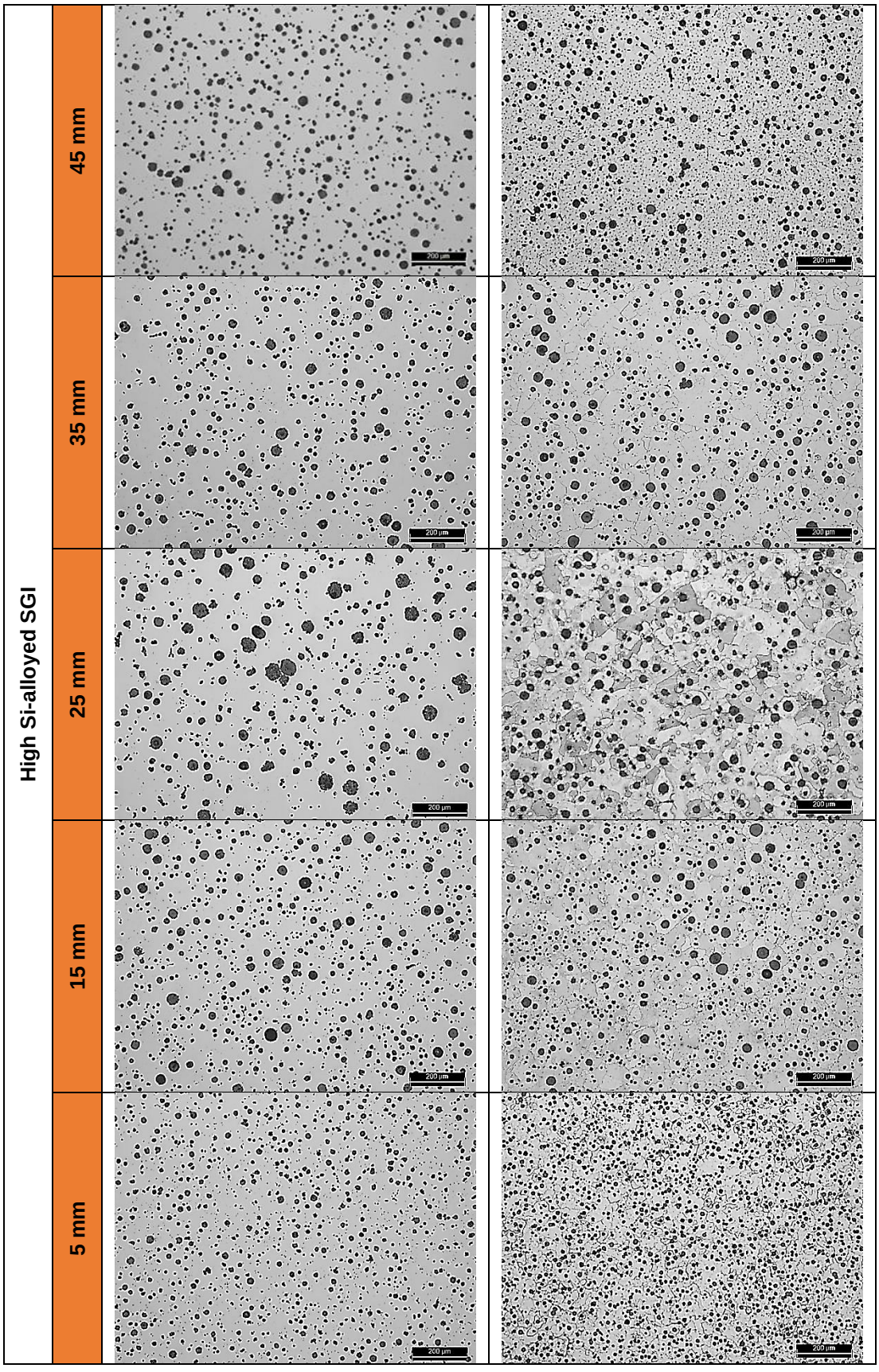


Figure 4 - 4. LOM micrographs of the High Si-alloyed SGI, for different section thicknesses.

Table 4 - 4. Microstructural parameters of the High Si-alloyed SGI, for different section thicknesses

High Si-alloyed SGI	Section thickness (mm)	5	15	25	35	45
	Graphite (%)	8.3	12.0	11.1	11.4	12.4
	Nodularity (%)	91	92	92	92	91
	Nodule count (particles/mm^2)	762	698	514	482	594
	Convex perimeter (µm)	35	42	48	50	47
	Graphite form-III (%)	1.1	1.1	2.0	2.0	1.8

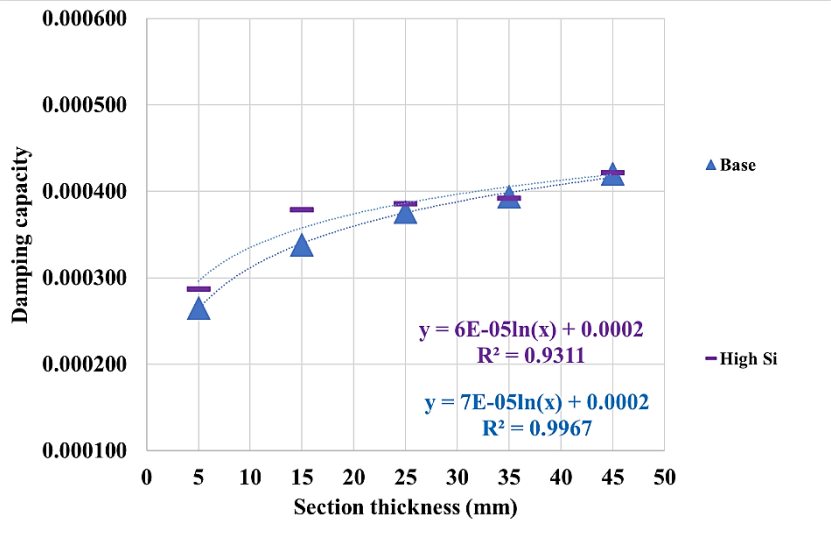


Figure 4 - 5. Damping capacity of the High Si-alloyed and Base 0 SGIs *vs.* the section thicknesses of the step-castings.

Table 4 - 5. Variation of the damping capacity of the High Si-alloyed SGI

High Si	Section thickness (mm)	5	15	25	35	45
	Relative variation (%)	9	12	2	-1	0
	CV estimated (%)	*± 1*				

As already mentioned, Si alloying is well stated in the literature for promoting the solid solution strengthening of the ferrite, which can be corroborated, at a first look, by the results of the ultimate tensile strength obtained (Figure 4 - 6 and Table 4 - 6). Its increase was registered in samples

with section thicknesses between 45 and 15 mm, although without a significant variation for this thicknesses range.

For the 5 mm section thickness, a decrease in the ultimate tensile strength was registered, which might have been due to some sample heterogeneity. Effectively, as will be seen later (Figure 4 - 7), the 0.2% offset yield strength did not decrease for this section thickness. Therefore, this result was discarded in the development of the model to estimate the damping capacity.

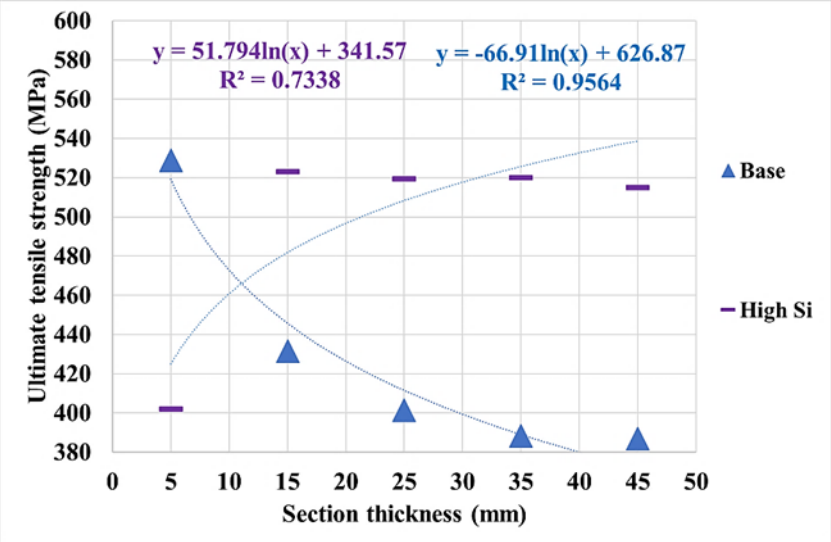


Figure 4 - 6. Ultimate tensile strength of the High Si-alloyed and Base 0 SGIs *vs.* the section thicknesses of the step-castings.

Table 4 - 6. Variation of the ultimate tensile strength of the High Si-alloyed SGI

High Si	**Section thickness (mm)**	**5**	**15**	**25**	**35**	**45**
	Relative variation (%)	-24	21	29	34	33
	CV estimated (%)	± 7				

A significant increase, relative to the Base 0 SGI, was observed regarding the 0.2% offset yield (Figure 4 - 7 and Table 4 - 7). Nevertheless, the results for the High-Si-alloyed SGI are quite similar regardless of the

section thicknesses (Figure 4 - 7), indicating that this mechanical property for this SGI doesn't vary significantly with the cooling rate.

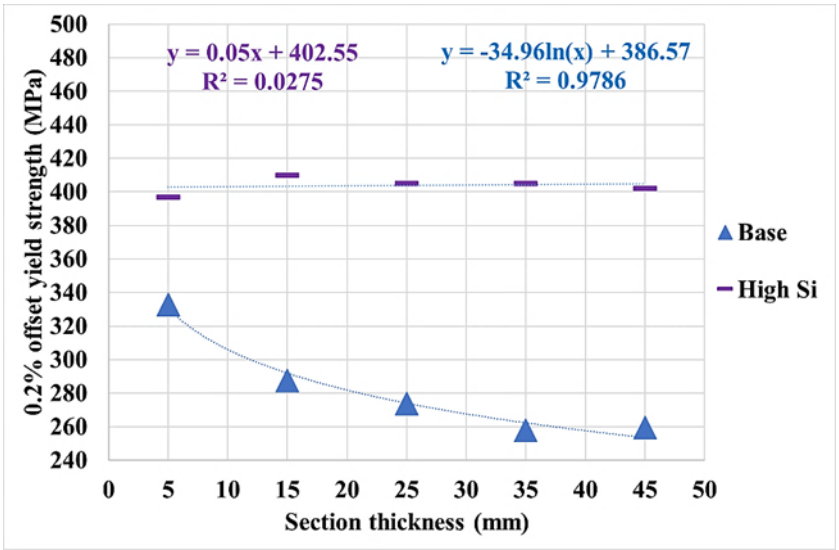


Figure 4 - 7. 0.2% offset yield strength of the High Si-alloyed and Base 0 SGIs *vs.* the section thicknesses of the step-castings.

Table 4 - 7. Variation of the 0.2% offset yield strength of the High Si-alloyed SGI

High Si	**Section thickness (mm)**	**5**	**15**	**25**	**35**	**45**
	Relative variation (%)	19	43	48	57	55
	CV estimated (%)	*± 6*				

The values for elongation are presented in Figure 4 - 8 and Table 4 - 8; an improvement was observed for the 25 and 15 mm section thicknesses. In contrast, no variation has been registered for the 45 and 35 mm thicknesses.

Although the Si alloying promoted matrix strengthening, the elongation is still considered high, as expected for an SGI. For instance, for the 15 mm section thickness, a 520 MPa ultimate tensile strength and a 21.9% elongation were obtained, with a 12% ± *1%* increase in the damping capacity.

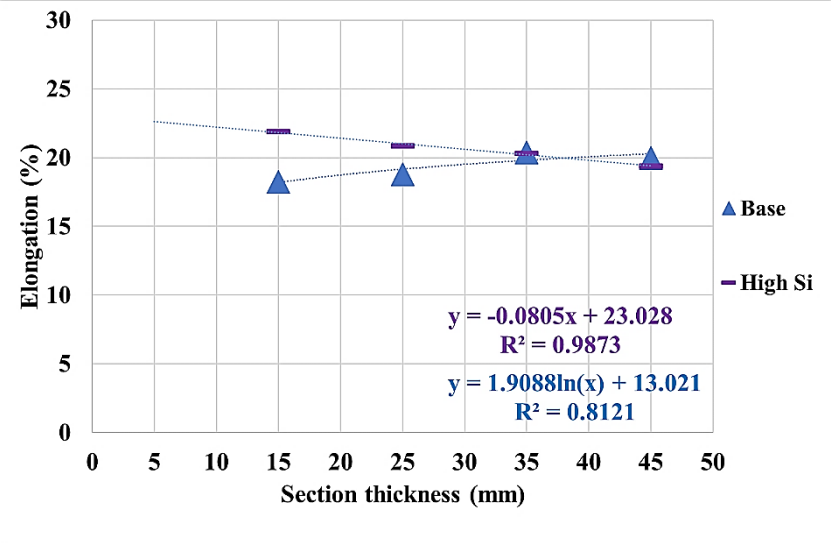


Figure 4 - 8. Elongation of the High Si-alloyed and Base 0 SGIs *vs.* the section thicknesses of the step-castings.

Table 4 - 8. Variation of the elongation of the High Si-alloyed SGI

High Si	**Section thickness (mm)**	**15**	**25**	**35**	**45**
	Relative variation (%)	20	11	0	-3
	CV estimated (%)	*± 6*			

From the analysis of Figure 4 - 9 and Table 4 - 9, in general, and only considering the coefficient of variation estimated, we can observe a decrease of Young's modulus relative to the Base 0 SGI.

The values obtained are still considered high for an SGI (the minimum Young's modulus obtained was 171 GPa). Moreover, considering the absolute values, the differences might not be substantial, for instance, 4 GPa for the 5 mm section thickness.

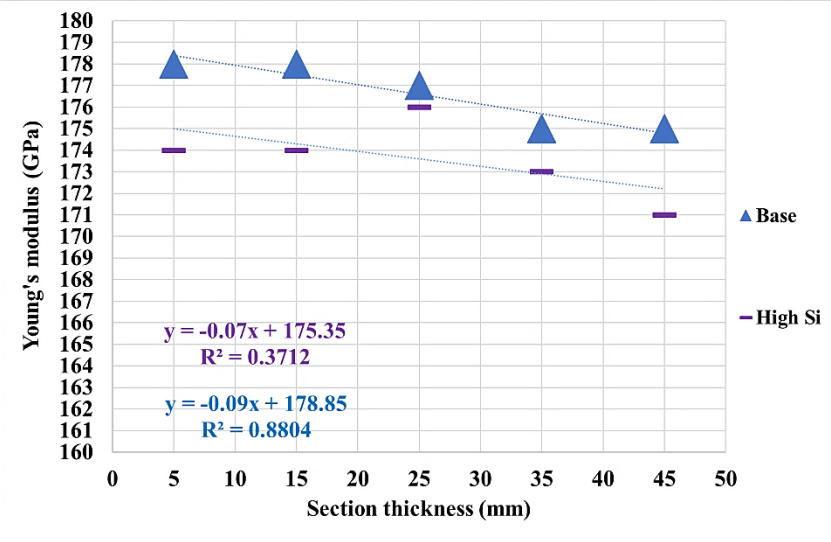


Figure 4 - 9. Young's modulus of the High Si-alloyed and Base 0 SGIs *vs.* the section thicknesses of the step-castings.

Table 4 - 9. Variation of the Young's modulus of the High Si-alloyed SGI

High Si	**Section thickness (mm)**	**5**	**15**	**25**	**35**	**45**
	Relative variation (%)	-2.3	-2.3	-0.6	-1.1	-2.3
	CV estimated (%)	*± 1.1*	*± 1.1*	*± 1.1*	*± 1.2*	*± 1.2*

Finally, from the data in Table 4 - 10, it will be possible to stress an improvement of the hardness relative to the Base 0 SGI, corroborating the solid solution strengthening of the matrix by the Si.

Table 4 - 10. Variation of the hardness of the High Si-alloyed SGI

High Si	**Section thickness (mm)**	**5**	**15**	**25**	**35**	**45**	**Trend line equation and R^2 for the material property (y) *vs.* the section thickness (x)**
	Hardness (HBW 2.5/-*) *62.5: ≤ 140 HBW or 187.5: > 140 HBW	187	185	182	183	181	$y = -2.564 \ln(x) + 191.44$ $R^2 = 0.8417$
	Relative variation (%)	18	34	23	40	38	
	CV estimated (%)	*± 5*					

4.2.1.1.2. Co-alloyed SGI

Co was chosen as an alloying element to promote ferrite formation and potentially increase the damping capacity.

According to the literature, Co increases the fraction of ferrite in SGI and induces an increase in tensile and yield strengths [74].

Co was tested for two different contents: 2.4% and 4.3%.

In order to understand the effect of the Co alloying on the microstructure of the SGI casting, one sample from each section thickness was observed by optical microscopy. The microstructures of the castings are presented in Figure 4 - 10 and Figure 4 - 11.

The samples from both compositions appear to have a similar structure. For the section thicknesses of 45 to 15 mm, the graphite nodules are dispersed in a ferritic matrix containing some residual pearlite.

For the samples from the 5 mm section thickness, the fraction of pearlite is higher, reaching 20% (Table 4 - 11 and Table 4 - 12). The higher cooling rate of the solidification of this section promotes the formation of pearlite, indicating that the ferritizing power of Co decreases for thinner sections.

The results obtained from the microstructural analysis of the Co (x1) samples also show that nodularity is lower than in the Co (x2) samples for thinner section thicknesses, indicating that increasing the Co content would improve the SGI nodularity. This phenomenon may have been related to the more significant fraction of graphite form-III obtained for the 5 and 15 mm section thicknesses from the Co (x1) experiments. Nevertheless, the nodularity obtained for both compositions is lower than the Base 0 SGI.

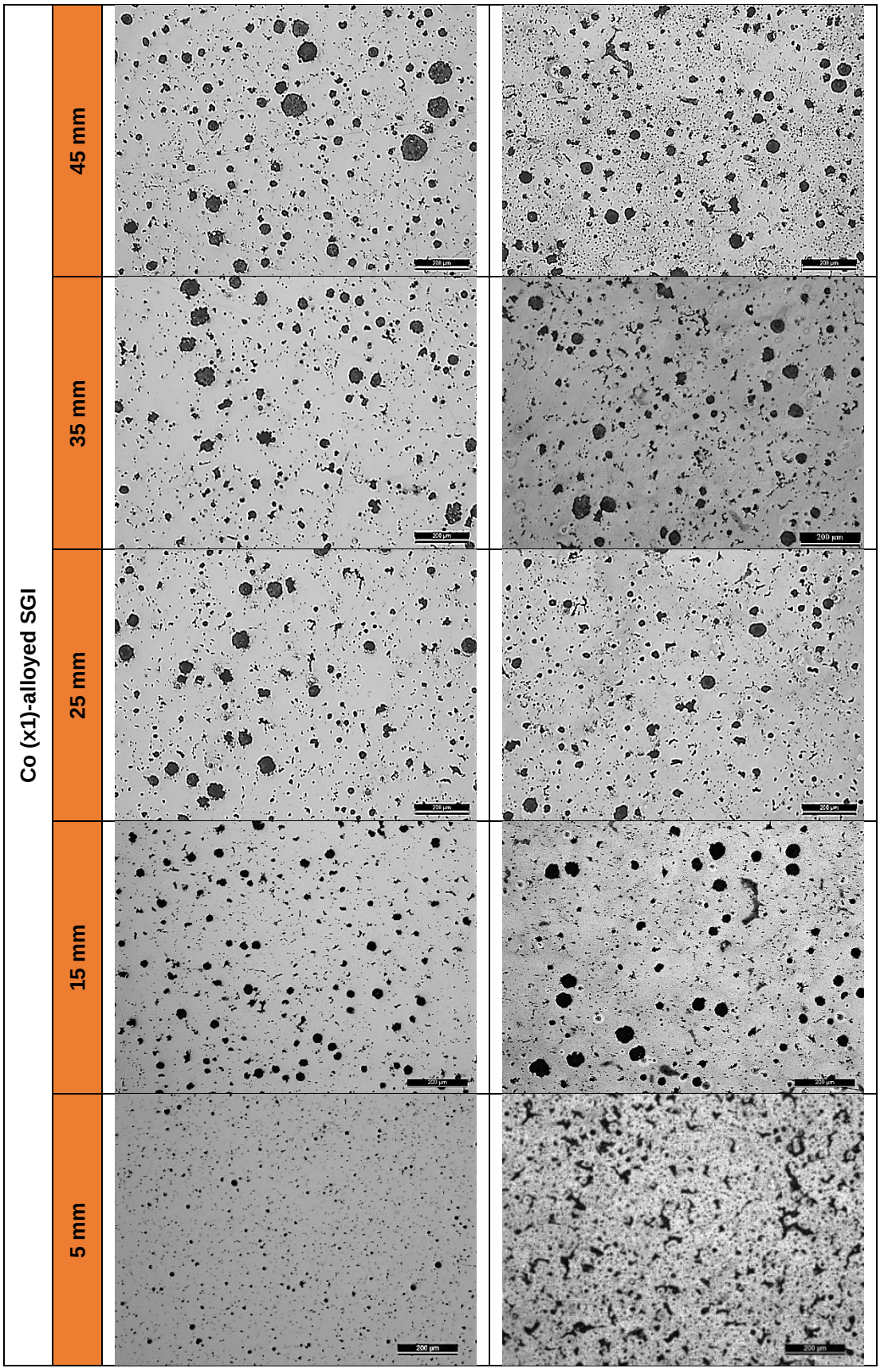


Figure 4 - 10. LOM micrographs of the Co (x1)-alloyed SGI, for different section thicknesses.

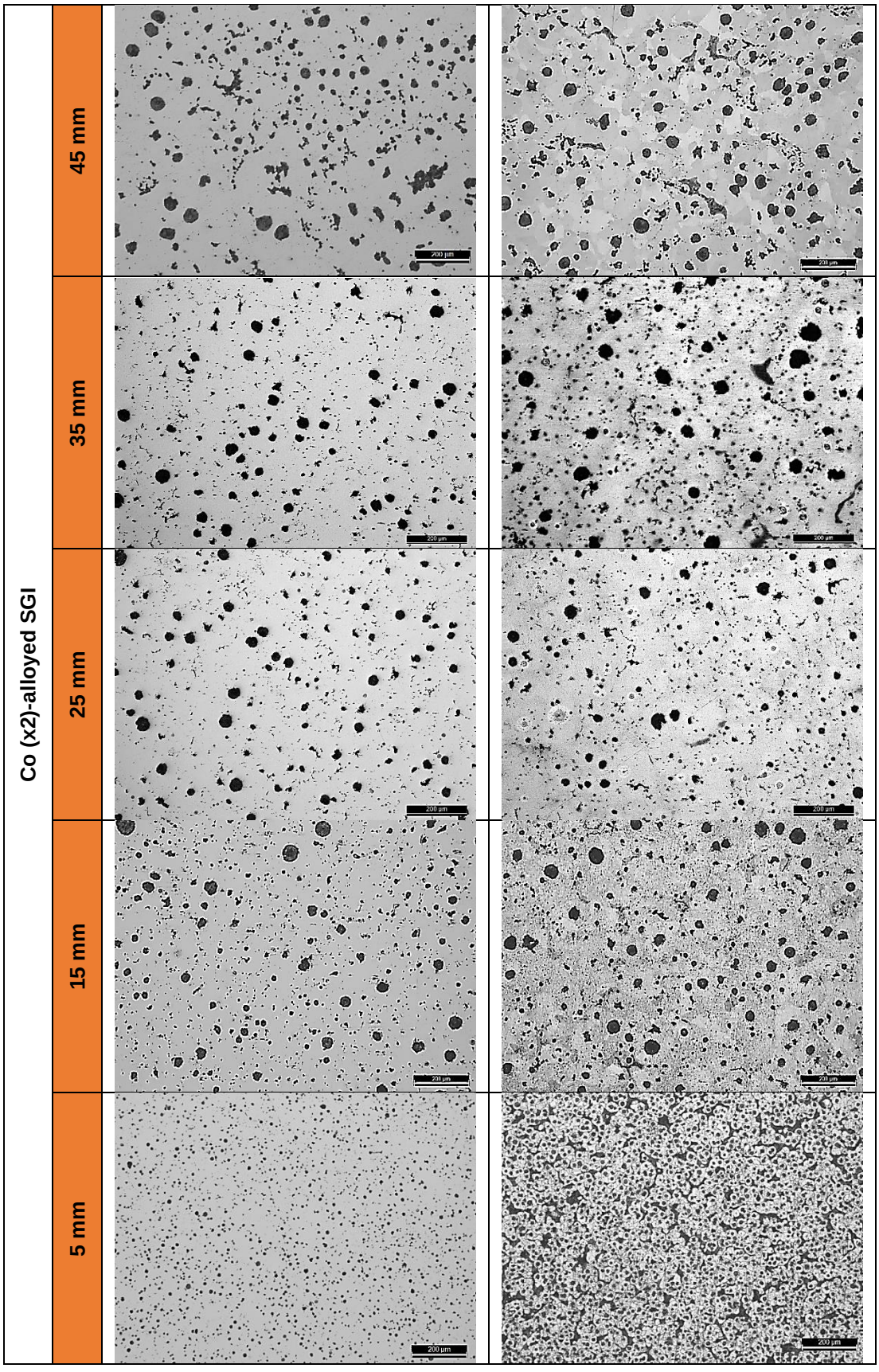


Figure 4 - 11. LOM micrographs of the Co (x2)-alloyed SGI, for different section thicknesses.

Table 4 - 11. Microstructural parameters of the Co (x1)-alloyed SGI, for different section thicknesses

Co (x1)-alloyed SGI	Section thickness (mm)	5	15	25	35	45
	Pearlite (%)	20	Residual			
	Graphite (%)	2.8[5]	7.0	8.5	8.3	10.0
	Nodularity (%)	63	64	71	71	73
	Nodule count (particles/mm^2)	467	416	336	331	325
	Convex perimeter (µm)	30	43	49	47	51
	Graphite form-III (%)	15.0	13.3	9.4	11.2	10.8

Table 4 - 12. Microstructural parameters of the Co (x2)-alloyed SGI, for different section thicknesses

Co (x2)-alloyed SGI	Section thickness (mm)	5	15	25	35	45
	Pearlite (%)	20	Residual			
	Graphite (%)	8.4	8.7	5.7	7.5	12.6
	Nodularity (%)	84	75	61	60	64
	Nodule count (particles/mm^2)	1083	475	322	482	322
	Convex perimeter (µm)	30	43	45	41	64
	Graphite form-III (%)	2.9	6.6	19.1	20.6	18.8

In the meantime, the samples from the 45 mm section thickness of the Co (x2)-alloyed SGI were analysed by EPMA to understand better the microstructure revealed by LOM observation.

Figure 4 - 12 shows the results of that analysis. The yellow areas will correspond to a higher concentration of the element under analysis, while the blue areas to a lower concentration.

We can observe that Si and Co present similar distributions, with higher concentrations around the graphite nodules.

[5] Only the particles with an area ≥ 25 µm^2 and length > 5 µm were considered. Therefore, the graphite particles considered depend on their size; for instance, very small particles or chunky graphite might not be considered.

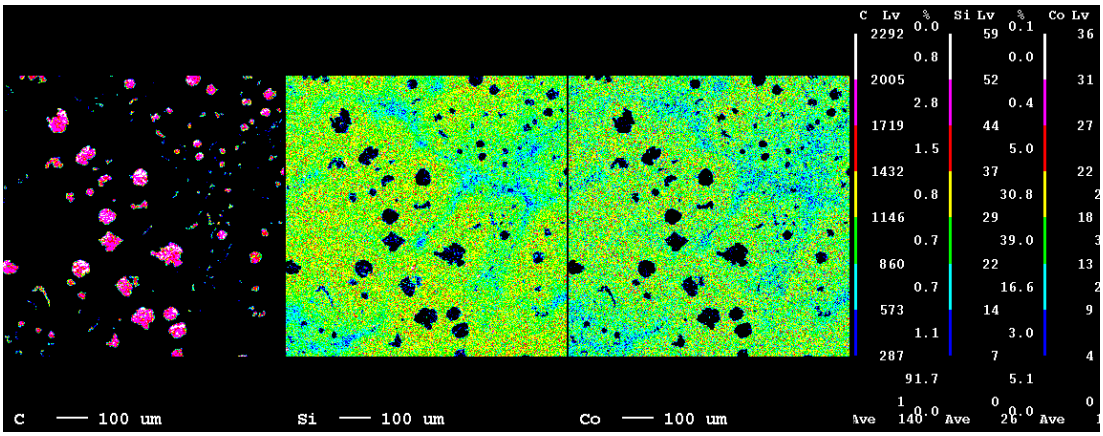


Figure 4 - 12. EPMA maps for C, Si and Co for the Co (x2)-alloyed SGI, for the 45 mm section thickness.

Damping capacity was first evaluated to clarify the effect of the microstructure on this mechanical property. It was generally found that the Co-alloyed SGIs present higher damping capacity than the Base 0 SGI, as presented in Figure 4 - 13 and Table 4 - 13.

Moreover, the trend lines indicate that damping capacity decreases with section thickness, which appears to be associated with an increase in the fraction of pearlite.

The most significant improvement was 26% ± *1%*, obtained for the 35 and 25 mm section thicknesses for the Co (x2)-alloyed SGI. The samples present a fully ferritic matrix (*i.e.*, pearlite < 5%) and nodularity and a fraction of graphite lower than the Base 0 SGI.

The almost doubling of the Co content, from 2.4% to 4.3%, has proven to be a good bet on improving SGI damping capacity.

The variation of the damping capacity of the Co-alloyed SGI (regardless of its content) seems less affected by the variation of the section thickness than the Base 0 SGI. So, the damping capacity appears to be only associated with graphite variations since the matrix is fully ferritic for section thicknesses between 45 and 15 mm. For the Base 0 SGI, the fraction of pearlite varied for the different section thicknesses.

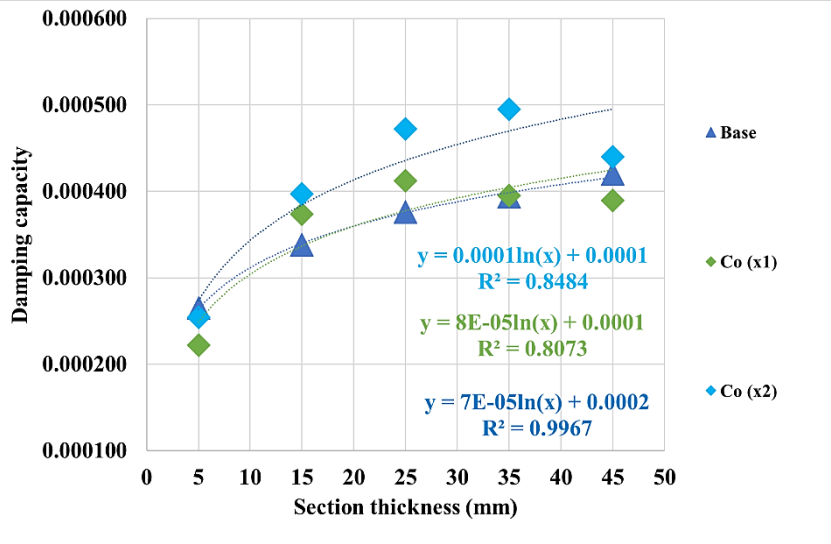


Figure 4 - 13. Damping capacity of the Co-alloyed and Base 0 SGIs *vs.* the section thicknesses of the step-castings.

Table 4 - 13. Variation of the damping capacity of the Co-alloyed SGIs

Section thickness (mm)		**5**	**15**	**25**	**35**	**45**
Co (x1)	**Relative variation (%)**	-16	10	10	0	-7
Co (x2)		-4	18	26	26	5
CV estimated (%)		*± 1*				

As mentioned before, the primary goal of this thesis was to establish the best compromise between the mechanical properties aimed for an SGI and its damping capacity; therefore, tensile tests were performed to verify the impact of the microstructure on the mechanical properties.

An improvement of the ultimate tensile strength was achieved for the Co-alloyed SGIs (Figure 4 - 14), with a maximum of 12% ± *7%* (Table 4 - 14).

As aforementioned, the microstructures of the samples with 5 mm section thickness for both Co-alloyed SGIs present pearlite, meaning that the higher cooling rate compromises the ferritizing power of Co.

Notice that the pearlite's interlamellar spacing was not evaluated, which might influence the tensile properties since a larger spacing may lead to lower tensile values. However, as the focus was the fully ferritic SGI, only the fraction of pearlite in the matrix has been evaluated.

Once again, Co-alloyed SGIs seem less influenced by the variation of the section thickness because a more consistent behaviour was registered.

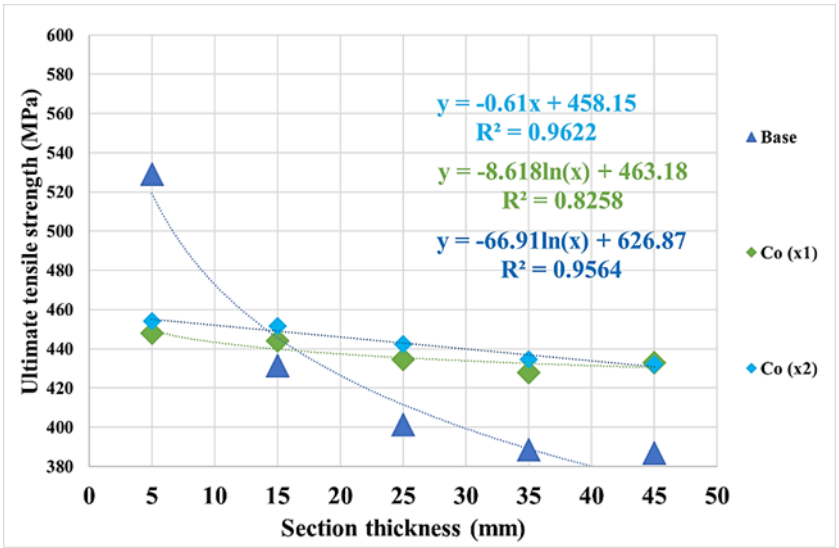


Figure 4 - 14. Ultimate tensile strength of the Co-alloyed and Base 0 SGIs *vs.* the section thicknesses of the step-castings.

Table 4 - 14. Variation of the ultimate tensile strength of the Co-alloyed SGIs

Section thickness (mm)		**5**	**15**	**25**	**35**	**45**
Co (x1)	**Relative variation (%)**	-15	3	8	10	12
Co (x2)		-14	5	10	12	12
CV estimated (%)		± 7				

The 0.2% offset yield strength increased for the Co-alloyed SGIs, as observed in Figure 4 - 15 and Table 4 - 15. The most significant improvement registered was 20% ± *6%*.

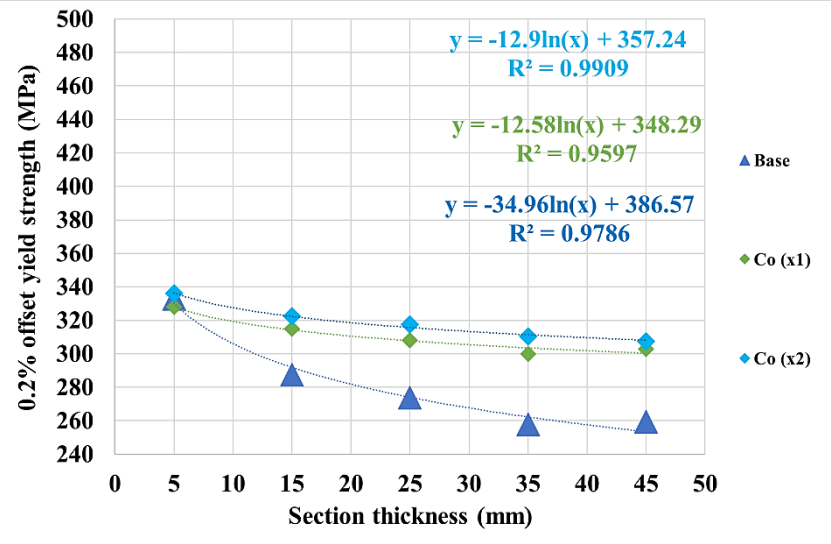


Figure 4 - 15. 0.2% offset yield strength of the Co-alloyed and Base 0 SGIs *vs.* the section thicknesses of the step-castings.

Table 4 - 15. Variation of the 0.2% offset yield strength of the Co-alloyed SGIs

Section thickness (mm)		**5**	**15**	**25**	**35**	**45**
Co (x1)	**Relative variation (%)**	-2	10	12	16	17
Co (x2)		1	12	16	20	18
CV estimated (%)		± *6*				

The results for the elongation of the Co-alloyed SGIs samples are shown in Figure 4 - 16 and Table 4 - 16. Different relative variations were observed for all the section thicknesses.

The most significant improvement was 25% ± *6%*.

The minimum elongation obtained was 19.2% for a minimum tensile strength of 428 MPa.

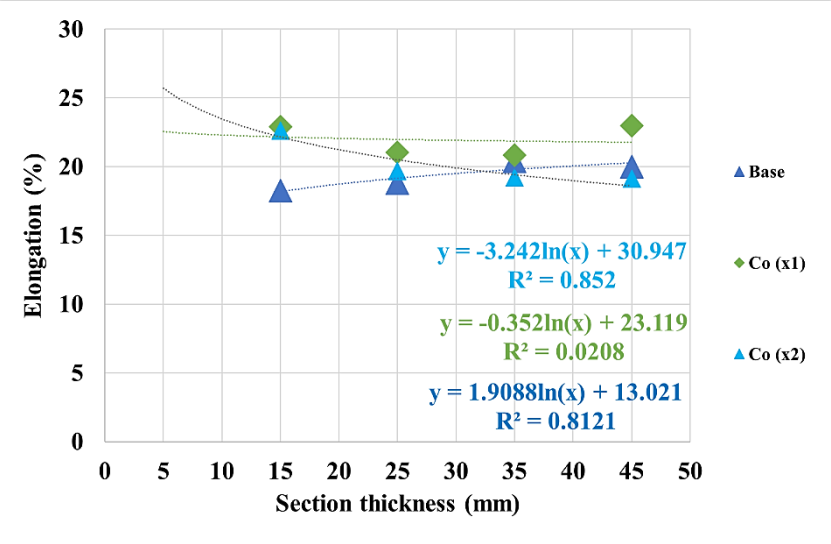


Figure 4 - 16. Elongation of the Co-alloyed and Base 0 SGIs *vs.* the section thicknesses of the step-castings.

Table 4 - 16. Variation of the elongation of the Co-alloyed SGIs

Section thickness (mm)		**15**	**25**	**35**	**45**
Co (x1)	**Relative variation (%)**	25	12	2	15
Co (x2)		24	5	-6	-4
CV estimated (%)		*± 6*			

It was necessary to verify if Young's modulus is influenced by the microstructure since it is an important mechanical property to be considered in the project of the automotive components considered.

Table 4 - 17 shows that, in general, Young's modulus results were unaltered regarding the Base 0 SGI and that no substantial influence of the section thickness was observed (Figure 4 - 17). Moreover, although a decrease was observed in some cases, Young's modulus is still considered high for an SGI since a minimum of 170 GPa was obtained.

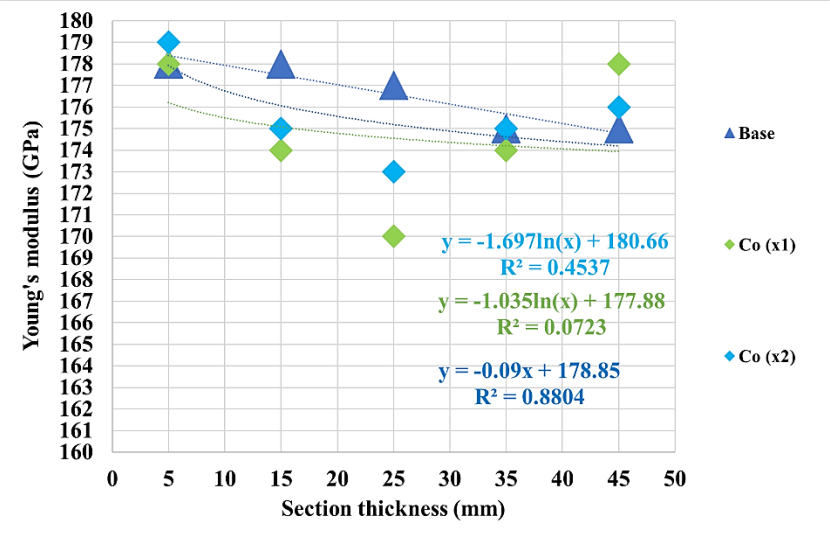


Figure 4 - 17. Young's modulus of the Co-alloyed and Base 0 SGIs *vs.* the section thicknesses of the step-castings.

Table 4 - 17. Variation of the Young's modulus of the Co-alloyed SGIs

Section thickness (mm)		**5**	**15**	**25**	**35**	**45**
Co (x1)	**Relative variation (%)**	0	-2.3	-3.9	-0.6	1.7
	CV estimated (%)	*± 1.2*	*± 1.1*	*± 1.1*	*± 1.2*	*± 3.2*
Co (x2)	**Relative variation (%)**	0.6	-1.7	-2.3	0	0.6
	CV estimated (%)	*± 2.1*	*± 2.2*	*± 1.1*	*± 1.2*	*± 1.2*

A hardness improvement, relative to the Base 0 SGI, was registered for both compositions (Table 4 - 18), indicating a solid state strengthening of the matrix by the Co.

Similar hardness values were obtained for both SGIs. Additionally, it is noticed that the matrix strengthening effects by the Co and the pearlite are comparable since it was found similar (or higher) hardness values to those from a ferritic-pearlitic matrix (Base 0).

Table 4 - 18. Variation of the hardness of the Co-alloyed SGIs

Section thickness (mm)		5	15	25	35	45	Trend line equation and R^2 for the material property (y) *vs.* the section thickness (x)
Co (x1)	**Hardness (HBW 2.5/-*)** *62.5: ≤ 140 HBW or 187.5: > 140 HBW	181	153	153	149	147	$y = -15.15 \ln(x) + 201.71$ $R^2 = 0.9041$
	Relative variation (%)	14	11	3	14	12	
Co (x2)	**Hardness (HBW 2.5/-*)** *62.5: ≤ 140 HBW or 187.5: > 140 HBW	186	158	153	150	152	$y = -16.36 \ln(x) + 208.58$ $R^2 = 0.8898$
	Relative variation (%)	17	14	3	14	16	
CV estimated (%)		± 5					

4.2.1.1.3. RE-alloyed SGI

As reported for the High Si-alloyed SGI (*sub-chapter 4.2.1.1.1.*), the improvement of the damping capacity was only obtained for lower section thicknesses. The samples present a fully ferritic matrix (*i.e.*, pearlite < 5%) but very high nodularity.

Therefore, a RE-alloyed SGI (0.048% RE) was produced to manipulate the graphite shape by adding RE elements.

Figure 4 - 18 shows the microstructures obtained for the RE (x1)-alloyed SGI: graphite nodules in a ferritic-pearlitic matrix. The pearlite fraction varies with section thickness (Table 4 - 19). Relative to the Base 0 SGI, the RE (x1)-alloyed-SGI samples present the following main general differences:

- lower fraction of pearlite;
- higher nodule count and fraction of graphite form-III;
- lower nodularity.

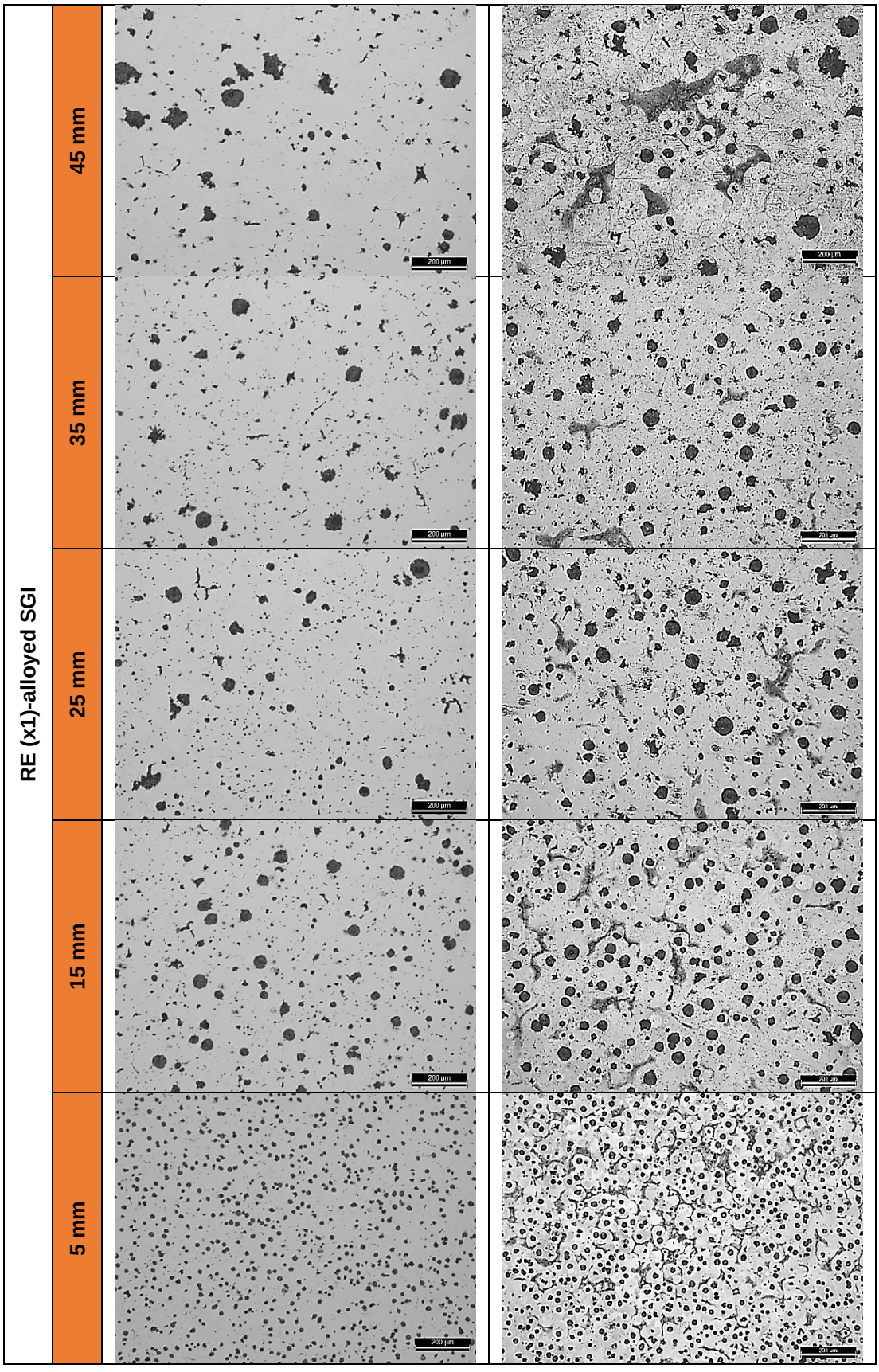


Figure 4 - 18. LOM micrographs of the RE (x1)-alloyed SGI, for different section thicknesses.

Table 4 - 19. Microstructural parameters of the RE (x1)-alloyed SGI, for different section thicknesses

RE (x1)-alloyed SGI	Section thickness (mm)	5	15	25	35	45
	Pearlite (%)	20	15	10	10	15
	Graphite (%)	14.1	13.7	5.7	5.9	7.2
	Nodularity (%)	79	84	65	51	53
	Nodule count (particles/mm^2)	635	415	310	305	195
	Convex perimeter (µm)	52	57	41	44	59
	Graphite form-III (%)	6.2	4.4	13.9	23.8	22.8

With RE addition, an increase in damping capacity for the 15 and 5 mm section thicknesses was achieved (Figure 4 - 19 and Table 4 - 20).

The damping capacity results show a similar tendency between High Si and RE (x1) trials: a relatively small increase regarding Base 0 SGI was only registered for lower section thicknesses.

The results (Table 4 - 20) point to a combination of a variation of the graphite morphology and the pearlite fraction.

It should be noticed that the potential impact of the interlamellar spacing of the pearlite microconstituent on the damping capacity was not evaluated. Therefore, further investigation would be necessary to fully interpret the results of the RE (x1) trial.

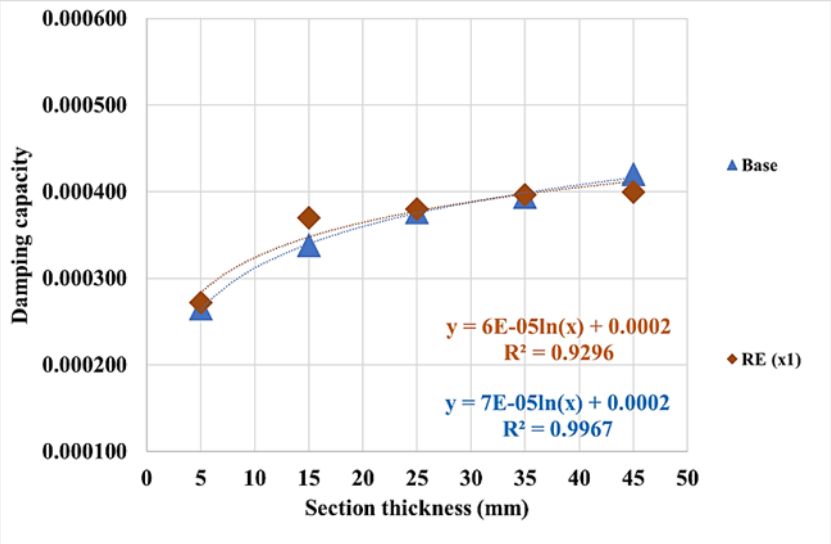


Figure 4 - 19. Damping capacity of the RE (x1)-alloyed and Base 0 SGIs *vs.* the section thicknesses of the step-castings.

Table 4 - 20. Variation of the damping capacity of the RE (x1)-alloyed SGI

RE (x1)	**Section thickness (mm)**	**5**	**15**	**25**	**35**	**45**
	Relative variation (%)	3	9	1	1	-5
	CV estimated (%)	*± 1*				

RE alloying doesn't significantly impact the tensile and yield strengths (Figure 4 - 20 and Figure 4 - 21, and Table 4 - 21 and Table 4 - 22) of the SGI.

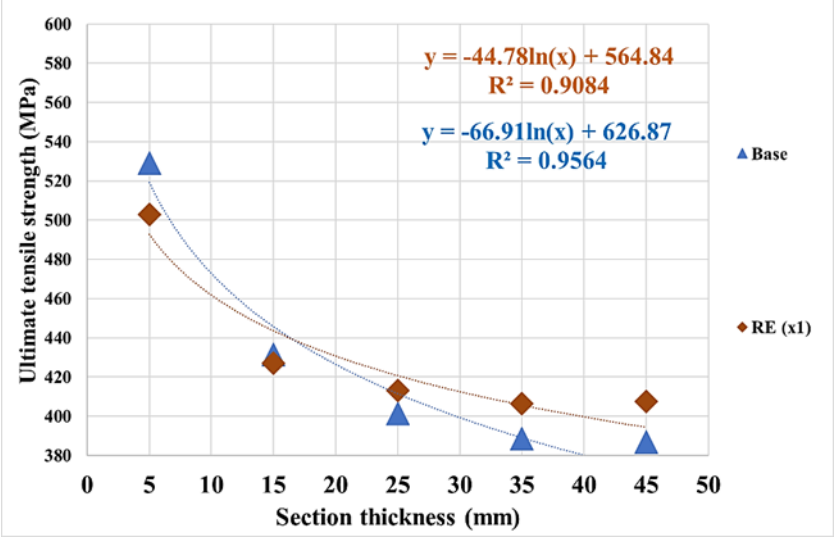


Figure 4 - 20. Ultimate tensile strength of the RE (x1)-alloyed and Base 0 SGIs *vs.* the section thicknesses of the step-castings.

Table 4 - 21. Variation of the ultimate tensile strength of the RE (x1)-alloyed SGI

RE (x1)	**Section thickness (mm)**	**5**	**15**	**25**	**35**	**45**
	Relative variation (%)	-5	-1	3	5	5
	CV estimated (%)	± 7				

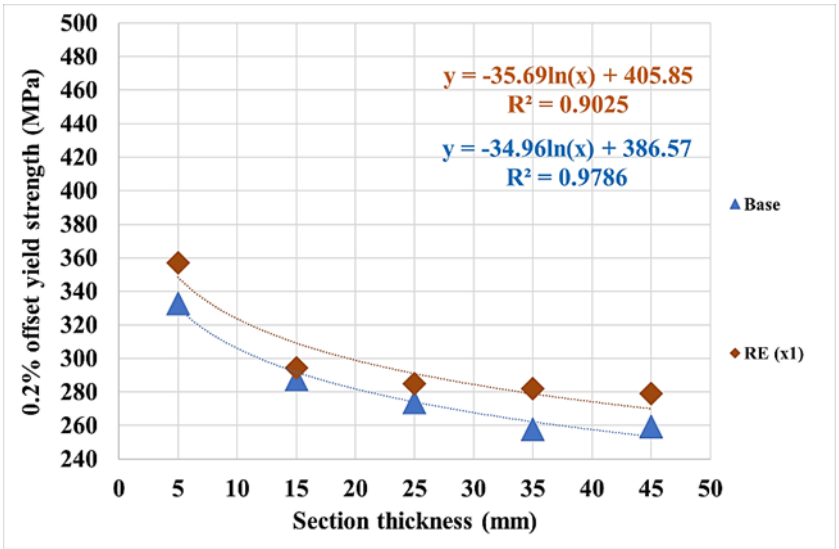


Figure 4 - 21. 0.2% offset yield strength of the RE (x1)-alloyed and Base 0 SGIs *vs.* the section thicknesses of the step-castings.

Table 4 - 22. Variation of the 0.2% offset yield strength of the RE (x1)-alloyed SGI

	Section thickness (mm)	5	15	25	35	45
RE (x1)	Relative variation (%)	7	2	4	9	8
	CV estimated (%)	± *6*				

Regarding elongation, an increase relative to the Base 0 SGI was registered (Figure 4 - 22), which can be explained by the decrease in the pearlite fraction of the matrix (Table 4 - 23).

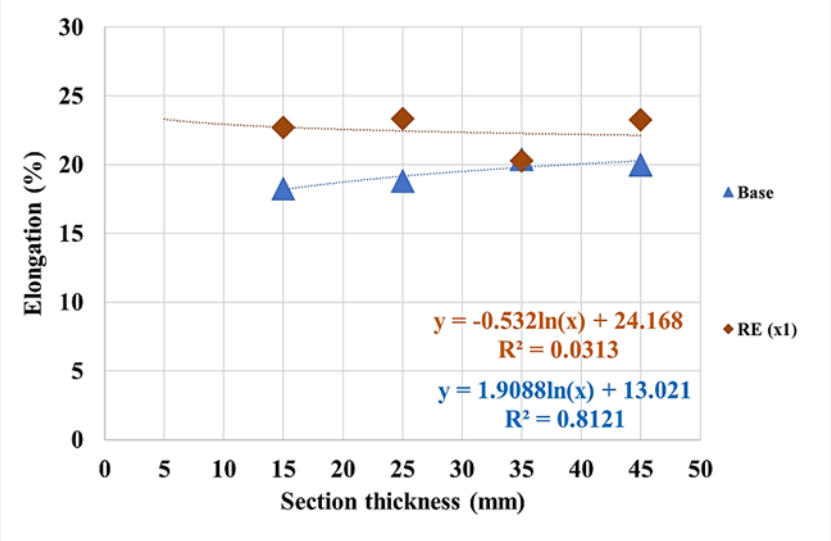


Figure 4 - 22. Elongation of the RE (x1)-alloyed and Base 0 SGIs *vs.* the section thicknesses of the step-castings.

Table 4 - 23. Variation of the elongation of the RE (x1)-alloyed SGI

	Section thickness (mm)	15	25	35	45
RE (x1)	Relative variation (%)	24	24	0	16
	CV estimated (%)	± *6*			

Although, in general, the variation of Young's modulus isn't so significant, its values vary in opposite directions with the section thicknesses, *i.e.*, it decreases for the RE-alloyed SGI and increases for the Base 0 SGI (Figure 4 - 23 and Table 4 - 24).

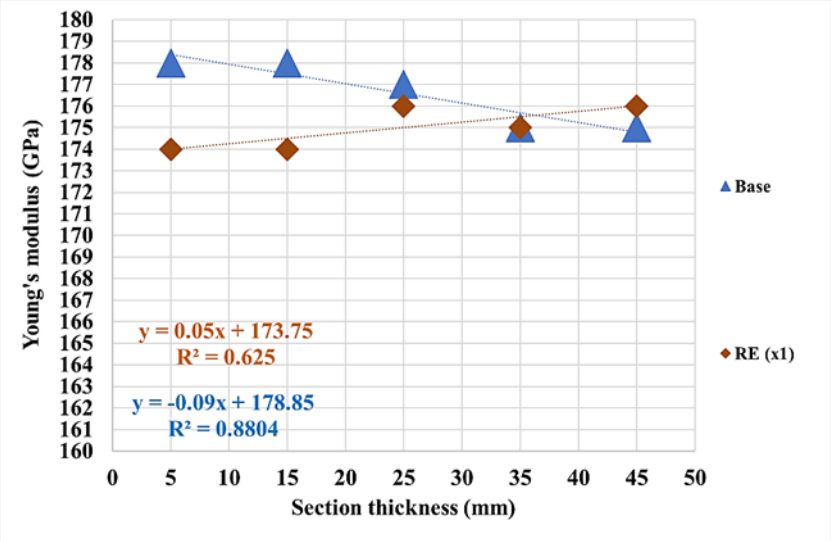


Figure 4 - 23. Young's modulus of the RE (x1)-alloyed and Base 0 SGIs *vs.* the section thicknesses of the step-castings.

Table 4 - 24**.** Variation of the Young's modulus of the RE (x1)-alloyed SGI

RE (x1)	**Section thickness (mm)**	**5**	**15**	**25**	**35**	**45**
	Relative variation (%)	-2.3	-2.3	-0.6	0.0	0.6
	CV estimated (%)	*± 1.3*	*± 2.2*	*± 1.1*	*± 1.2*	*± 2.2*

In its turn, the hardness presents a heterogeneous behaviour regarding its variation with the section thickness (Table 4 - 25), indicating that RE hasn't promoted the strengthening of the matrix by solid solution. The hardness values are similar to those from the Base 0 SGI, which also presents a ferritic-pearlitic matrix.

Table 4 - 25. Variation of the hardness of the RE (x1)-alloyed SGI

	Section thickness (mm)	5	15	25	35	45	Trend line equation and R^2 for the material property (y) *vs.* the section thickness (x)
RE (x1)	**Hardness (HBW 2.5/-*)** *62.5: ≤ 140 HBW or 187.5: > 140 HBW	156	154	138	135	131	$y = -0.6929x + 160.06$ $R^2 = 0.905$
	Relative variation (%)	-2	11	-7	3	0	
	CV estimated (%)	± 5					

4.2.1.1.4. High Si + RE-alloyed SGI

As previously stated, damping capacity increases for an SGI presenting a fully ferritic matrix (*i.e.*, pearlite < 5%) and lower nodularity. This was achieved for most of the section thicknesses of the Co-alloyed SGI. However, its cost is higher than other alloying options.

Therefore, a combination of two alloying elements was developed that alone increased the damping capacity, although not substantially: Si to promote a fully ferritic matrix and RE to decrease nodularity.

For High Si combined with RE elements, two compositions were tested: 3.4% Si + 0.024% RE and 3.4% Si + 0.045% RE. The lower RE content was considered to better control the excessive formation of chunky graphite.

Figure 4 - 24 and Figure 4 - 25 show the microstructures obtained from the High Si + RE-alloyed SGIs. A combination of the effects of both alloying elements was obtained: a fully ferritic matrix (*i.e.*, pearlite < 5%) and higher nodule count, but lower nodularity (Table 4 - 26 and Table 4 - 27).

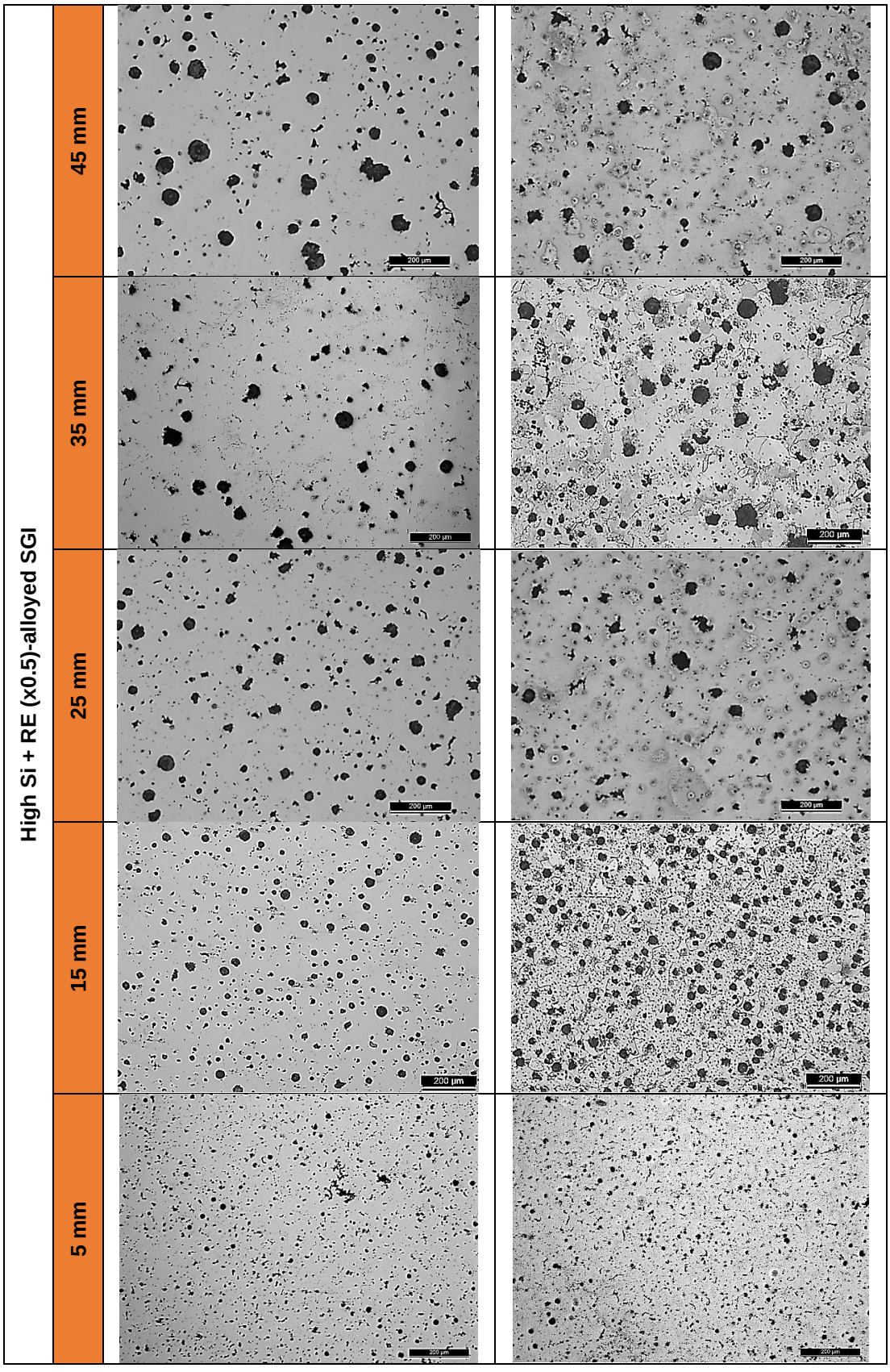


Figure 4 - 24. LOM micrographs of the High Si + RE (x0.5)-alloyed SGI, for different section thicknesses.

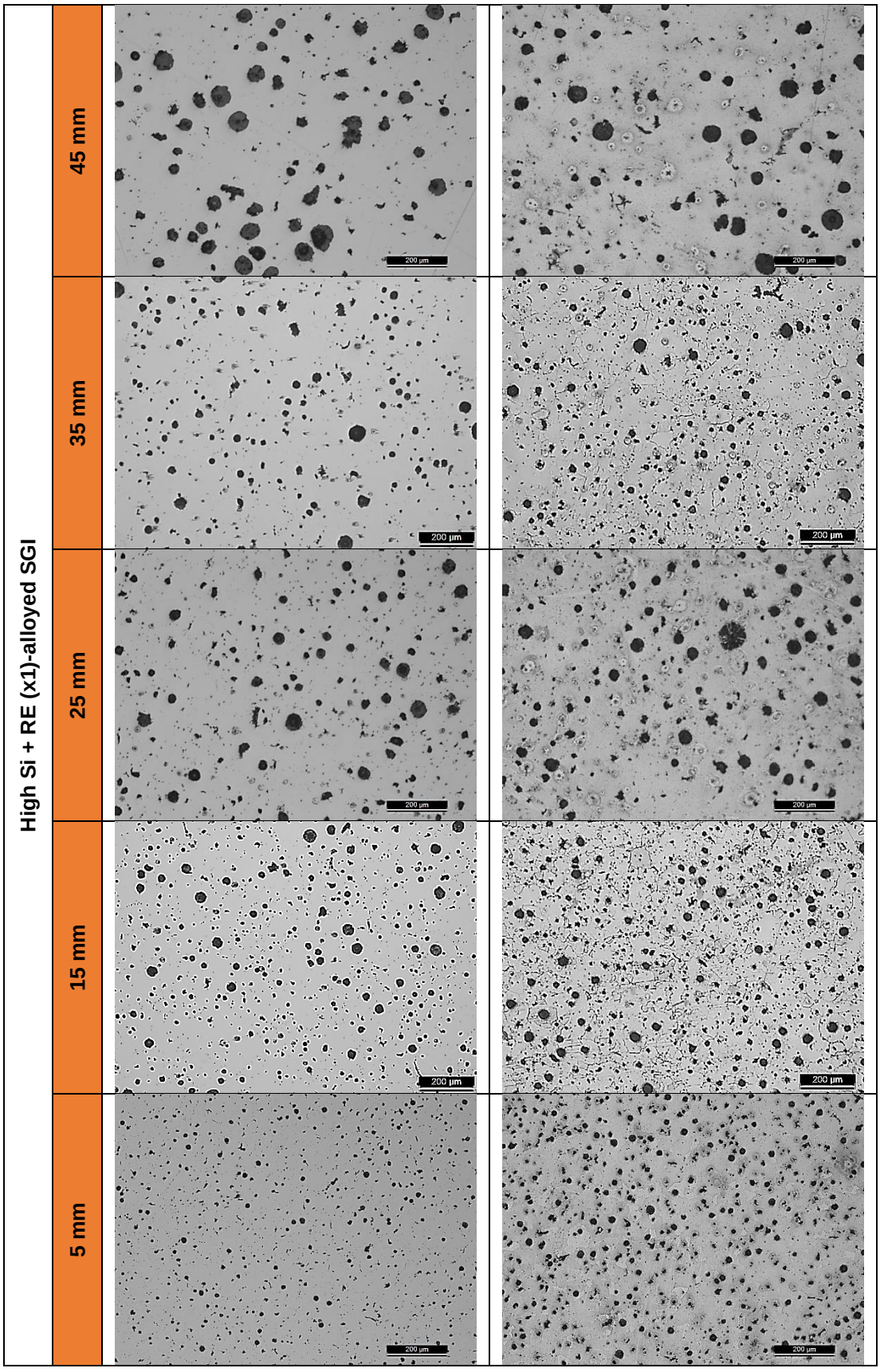


Figure 4 - 25. LOM micrographs of the High Si + RE (x1)-alloyed SGI, for different section thicknesses.

The nodularity and nodule count obtained for the High Si + RE (x0.5) SGI are, in general, lower than for the High Si + RE (x1), which, in turn, are lower than for the High Si-alloyed SGI (Table 4 - 26, Table 4 - 27 and Table 4 - 4, respectively).

Table 4 - 26. Microstructural parameters of the High Si + RE (x0.5)-alloyed SGI, for different section thicknesses

High Si + RE (x0.5) SGI	Section thickness (mm)	5	15	25	35	45
	Graphite (%)	5.1	7.7	10.5	5.2	10.4
	Nodularity (%)	64	82	68	42	68
	Nodule count (particles/mm^2)	679	406	382	243	300
	Convex perimeter (µm)	33	44	53	47	58
	Graphite form-III (%)	15.1	5.2	11.5	30.2	11.9

Table 4 - 27. Microstructural parameters of the High Si + RE (x1)-alloyed SGI, for different section thicknesses

High Si + RE (x1) SGI	Section thickness (mm)	5	15	25	35	45
	Graphite (%)	8.9	7.6	11.9	7.4	10.5
	Nodularity (%)	85	79	68	69	74
	Nodule count (particles/mm^2)	750	400	466	256	195
	Convex perimeter (µm)	38	45	50	53	74
	Graphite form-III (%)	3.6	7.9	11.9	13.9	8.8

On the other hand, higher damping capacity was obtained for both High Si + RE-alloyed SGIs (Figure 4 - 26 and Table 4 - 28).

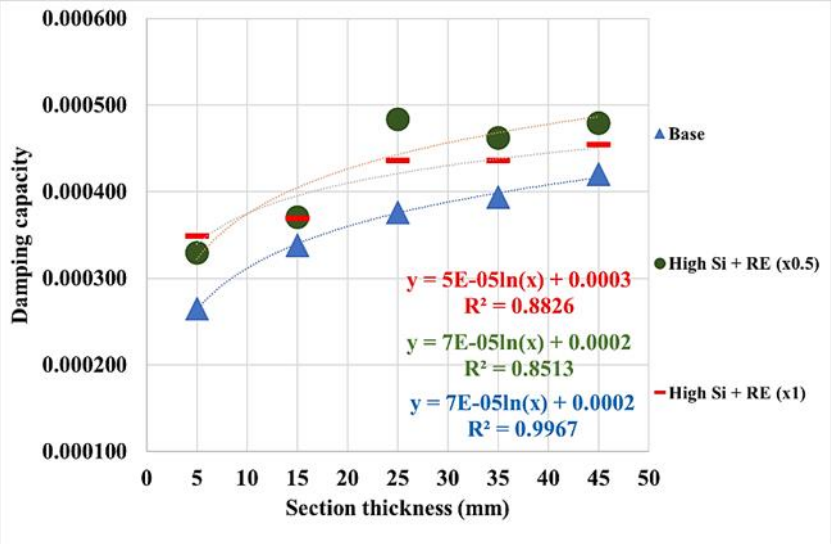


Figure 4 - 26. Damping capacity of the High Si + RE-alloyed and Base 0 SGIs *vs.* the section thicknesses of the step-castings.

Table 4 - 28. Variation of the damping capacity of the High Si + RE-alloyed SGIs

Section thickness (mm)		**5**	**15**	**25**	**35**	**45**
High Si + RE (x0.5)	**Relative variation (%)**	24	10	29	17	14
High Si + RE (x1)		32	9	16	11	8
CV estimated (%)		*± 1*				

Regarding the ultimate tensile strength, the results can be observed in Figure 4 - 27 and Table 4 - 29. There is no substantial impact of the section thickness on its values, most probably due to the fully ferritic matrix (*i.e.*, pearlite < 5%) presented by all the samples.

The ultimate tensile strength has improved for all the section thicknesses for the combination of both alloying elements, except for the 5 mm section thickness, which is similar to the value obtained for the Base 0 SGI. The results are identical for both compositions. As the Si content is the same for both SGIs, we can conclude that the matrix strengthening by solid solution will be only induced by the Si, which corroborates the results previously obtained.

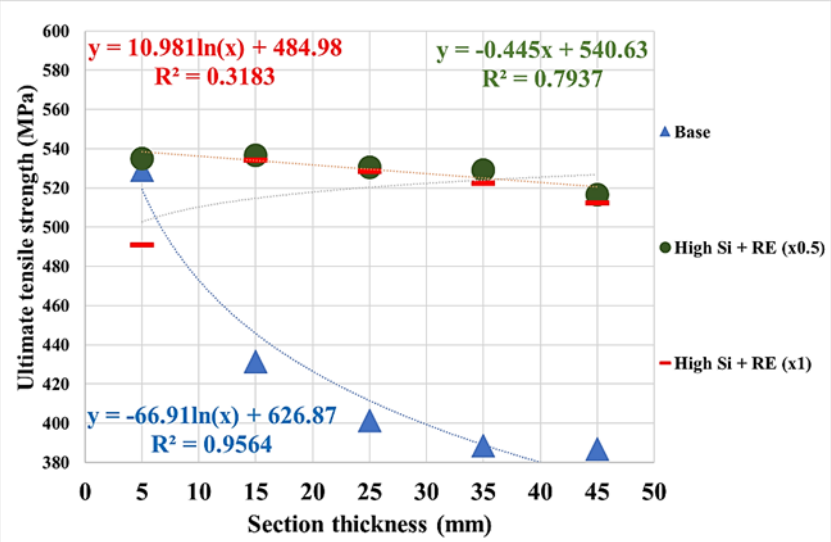


Figure 4 - 27. Ultimate tensile strength of the High Si + RE-alloyed and Base 0 SGIs *vs.* the section thicknesses of the step-castings.

Table 4 - 29. Variation of the ultimate tensile strength of the High Si + RE-alloyed SGIs

Section thickness (mm)		**5**	**15**	**25**	**35**	**45**
High Si + RE (x0.5)	**Relative variation (%)**	1	24	32	36	33
High Si + RE (x1)		-7	24	32	34	32
CV estimated (%)		± 7				

An increase of the 0.2% offset yield strength was registered (Figure 4 - 28 and Table 4 - 30) for all the section thicknesses and both compositions tested. As for the ultimate tensile strength, no significant influence of the section thickness variation was observed.

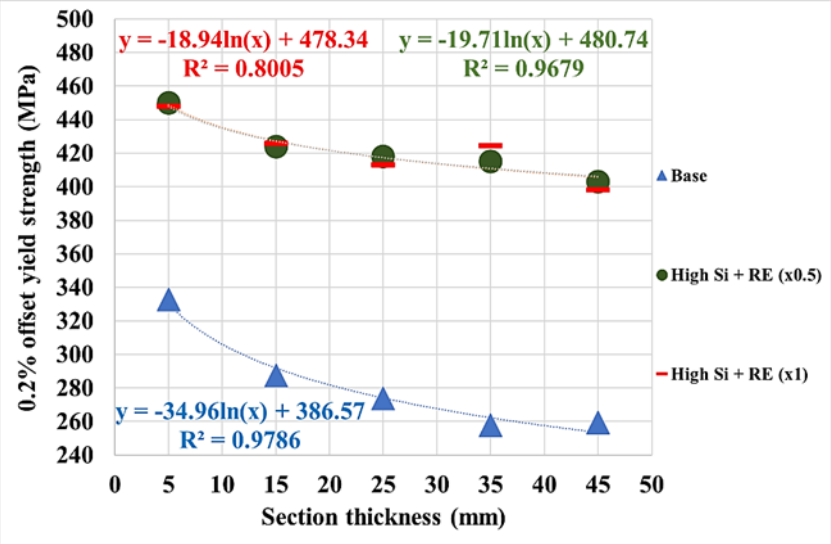


Figure 4 - 28. 0.2% offset yield strength of the High Si + RE-alloyed and Base 0 SGIs *vs.* the section thicknesses of the step-castings.

Table 4 - 30. Variation of the 0.2% offset yield strength of the High Si + RE-alloyed SGIs

Section thickness (mm)		**5**	**15**	**25**	**35**	**45**
High Si + RE (x0.5)	**Relative variation (%)**	35	48	51	65	53
High Si + RE (x1)		35	47	53	61	55
CV estimated (%)		± *6*				

Regarding elongation, the results obtained (Figure 4 - 29 and Table 4 - 31) show that the relative variation depends on the section thickness. An improvement in elongation was observed for the lower section thicknesses.

Regardless, elongation can still be considered high, taking into account the other tensile properties; for instance, the minimum elongation is higher than 15% (Figure 4 - 29), for an ultimate tensile strength higher than 500 MPa (Figure 4 - 27).

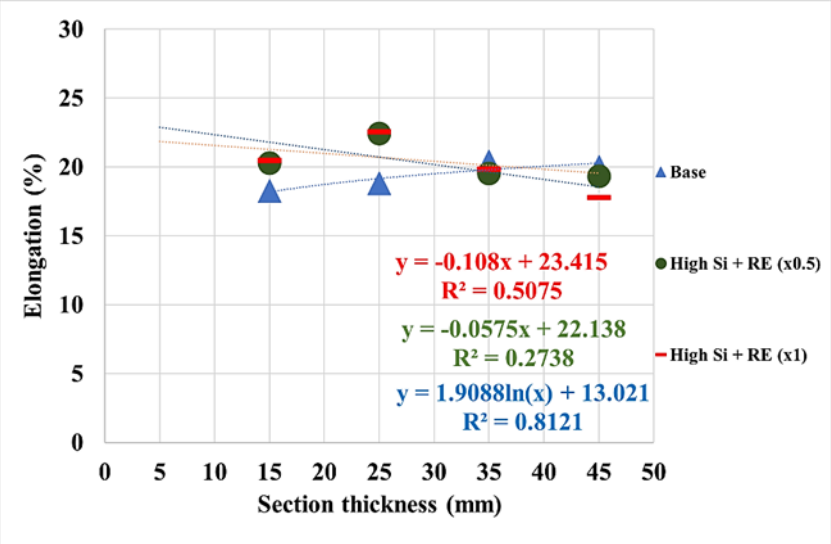


Figure 4 - 29. Elongation of the High Si + RE-alloyed and Base 0 SGIs *vs.* the section thicknesses of the step-castings.

Table 4 - 31. Variation of the elongation of the High Si + RE-alloyed SGIs

Section thickness (mm)		**5**	**15**	**25**	**35**	**45**
High Si + RE (x0.5)	**Relative variation (%)**	11	19	-4	-3	11
High Si + RE (x1)		12	20	-3	-11	12
CV estimated (%)		± *6*				

Although Young's modulus of the High Si + RE-alloyed SGIs decreased relative to the Base 0 (Figure 4 - 30 and Table 4 - 32), the values obtained can still be considered high (minimum of 170 GPa) for an SGI.

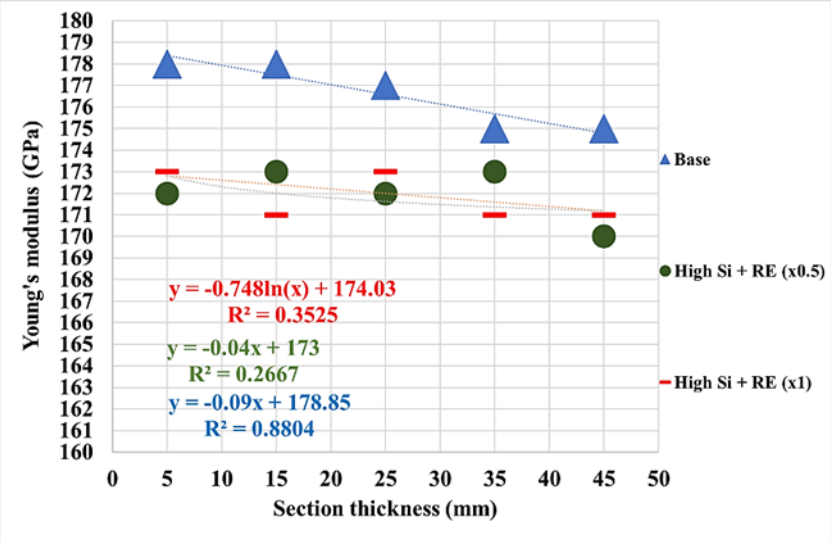


Figure 4 - 30. Young's modulus of the High Si + RE-alloyed and Base 0 SGIs *vs.* the section thicknesses of the step-castings.

Table 4 - 32. Variation of the Young's modulus of the High Si + RE-alloyed SGIs

Section thickness (mm)		**5**	**15**	**25**	**35**	**45**
High Si + RE (x0.5)	**Relative variation (%)**	-3.4	-2.8	-2.8	-1.1	-2.9
	CV estimated (%)	*± 1.2*	*± 2.5*	*± 1.1*	*± 1.3*	*± 1.2*
High Si + RE (x1)	**Relative variation (%)**	-2.8	-3.9	-2.3	-2.3	-2.3
	CV estimated (%)	*± 1.3*	*± 3.2*	*± 1.3*	*± 2.3*	*± 2.2*

Finally, regarding hardness, the results for the High Si + RE-alloyed SGIs are presented in Table 4 - 33. A significant hardness increase relative to the Base 0 SGI was achieved due to the matrix strengthening induced by the Si alloying.

Table 4 - 33. Variation of the hardness of the High Si + RE-alloyed SGIs, for different section thicknesses

Section thickness (mm)		5	15	25	35	45	Trend line equation and R^2 for the material property (y) *vs.* the section thickness (x)
High Si + RE (x0.5)	**Hardness (HBW 2.5/-*)** *62.5: ≤ 140 HBW or 187.5: > 140 HBW	193	196	183	188	179	$y = -0.3514x + 196.56$ $R^2 = 0.6228$
	Relative variation (%)	21	42	23	43	37	
High Si + RE (x1)	**Hardness (HBW 2.5/-*)** *62.5: ≤ 140 HBW or 187.5: > 140 HBW	192	193	183	188	176	$y = -0.3629x + 195.41$ $R^2 = 0.6838$
	Relative variation (%)	21	39	23	43	35	
CV estimated (%)		± 5					

4.2.2. Fine approach experiments

The chemical composition of the SGI melts produced for the fine approach experiments is presented in Table 4 - 34.

The castings were produced by a slightly different method (sub-chapter 3.1.3.) than for the first approach experiments since they were essentially used for the final validation of the more interesting results obtained in the first approach experiments.

For each set of trials, one base SGI (Base 1 and Base 2) was produced; on the other hand, a Ce alloy was used to prepare some melts instead of the RE alloy used for the fine approach experiments.

The results obtained for the experiments with the Base 1, Co + Ce (x0.5) and Co + Ce (x1) SGIs (Figure 3 - 7, *sub-chapter 3.1.3.2.*) were not considered for developing the model for the estimation of the SGI damping capacity because it will not consider the results obtained for the SGIs with a pearlitic-ferritic matrix. In the meantime, the corresponding results are presented in Annexe B.2.

On the other hand, the composition noted Base 2 corresponds to a standard ferritic-pearlitic SGI used as a comparison to analyse the impact of the different alloying elements on the mechanical properties of the SGIs developed. The microstructures, and the mechanical properties as well as the data relative to the microstructural analysis of this reference, are presented in Figure 4 - 31 and Table 4 - 35, respectively.

As mentioned before (sub-chapter 3.1.1.), only the 35 mm and also, for some melts, the 15 mm section thicknesses were considered for these experiments.

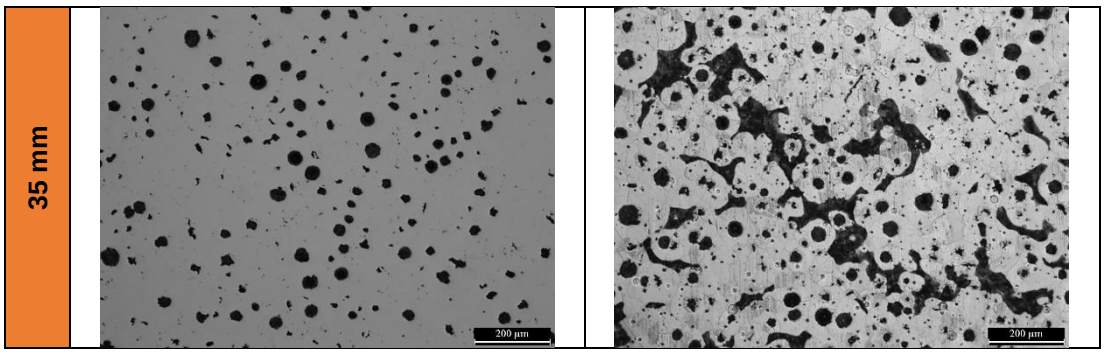
Table 4 - 34. Chemical composition of the SGI melts produced for the fine approach experiments

	Chemical composition (wt.%)						
	Base 1	**Co + Ce (x0.5)**	**Co + Ce (x1)**	**Base 2**	**High Si**	**High Si + Ce (x0.5)**	**High Si + Ce (x0.5) + Co**
C	3.47	3.67	3.73	3.92	3.85	3.91	3.90
Si	2.25	2.53	2.47	2.25	**3.24**	**3.27**	**4.5**
Mn	0.29	0.41	0.41	0.27	0.27	0.27	0.23
P	0.01	0.01	0.01	0.01	0.01	0.01	0.01
S	0.01	0.01	0.01	0.01	0.01	0.01	0.01
Mg	0.06	0.05	0.05	0.064	0.070	0.067	0.07
Cu	0.1	0.08	0.08	0.09	0.09	0.09	0.09
Mo	< 0.01	< 0.01	< 0.01	0.01	0.01	0.01	< 0.01
Co	–	**3.2**	**3.2**	–	–	–	**1.05**
Ce	–	***0.017***	***0.03***	0.008	0.008	**0.018**	**0.018**
La	–	*0.004*	*0.004*	0.004	0.004	0.004	0.004
Cr	0.4	0.4	0.4	0.067	0.067	0.067	0.067
Al	0.010	0.015	0.012	0.014	0.019	0.019	0.025
C.E.	*4.2*	*4.5*	*4.6*	*4.7*	*4.9*	*5.0*	*5.4*

Obs: C.E. calculated from Equation (9) (sub-chapter 2.3.1.2.)

The content of the alloying element(s) that qualify each trial is highlighted in bold

The composition of the Al (x5) melt couldn't be obtained due to the lack of standards for the calibration of the emission spectrometry



Before etching After etching

Figure 4 - 31. LOM micrographs of the Base 2 SGI, for the 35 mm section thickness.

Table 4 - 35. Results of the tests performed on the Base 2 SGI sample for the fine approach experiments

Section thickness (mm)	**35**
Damping capacity	0.000373
CV estimated (%)	*± 1*
Fundamental flexural frequency (Hz)	4251
CV estimated (%)	*± 0.004*
Young's modulus (GPa)	174
CV estimated (%)	*± 2.4*
Shear modulus (GPa)	68
CV estimated (%)	*± 0.9*
Poisson's ratio	0.273
CV estimated (%)	*± 0.06*
Ultimate tensile strength (MPa)	424
CV estimated (%)	*± 7*
0.2% offset yield strength (MPa)	308
CV estimated (%)	*± 6*
Elongation (%)	7.2
CV estimated (%)	*± 6*
Hardness (HBW 2.5/187.5)	149
CV estimated (%)	*± 5*
Pearlite (%)	25
Graphite (%)	7.2
Nodularity (%)	89
Nodule count (particles/mm^2)	198
Convex perimeter (µm)	63
Graphite form-III (%)	1.7

4.2.2.1. Evaluation of the fine approach experiments

A fine approach was conducted to validate the results of the most promising alloying combinations from the first approach experiments and pursue the development of the most promising alloyed SGI for the objectives of the *Brake Noise* project.

The evaluation of the fine approach experiments followed the categorization method presented in sub-chapter 4.2.1.1.; the results are presented in Table 4 - 36.

Table 4 - 36. Comparative evaluation of the mechanical properties of the SGI castings from the fine approach experiments

	Damping	Young's modulus	Ultimate tensile strength	0.2% offset yield strength	Elongation
High Si	+	–	+	+	+
High Si + Ce (x0.5)	+	–	+	+	+
High Si + Ce (x0.5) + Co	=	=	ND	ND	ND

ND – Not determined ***– Decreased*** ***= Unaltered*** ***+ Improved***

The damping capacity was generally improved without significantly decreasing the tensile properties for the High Si and High Si + Ce (x0.5) SGIs.

4.2.2.2. High Si-alloyed SGI combinations

Co and High Si combined with RE were the two most promising compositions tested in the first approach experiments (Figure 4 - 32). So, High Si and High Si + Ce[6] (x0.5) melts were prepared to produce test castings for validating some of the results obtained in the first approach experiments. Additionally, a High Si + Ce (x0.5) + Co-alloyed SGI was developed to evaluate whether Co-alloying would improve the damping capacity.

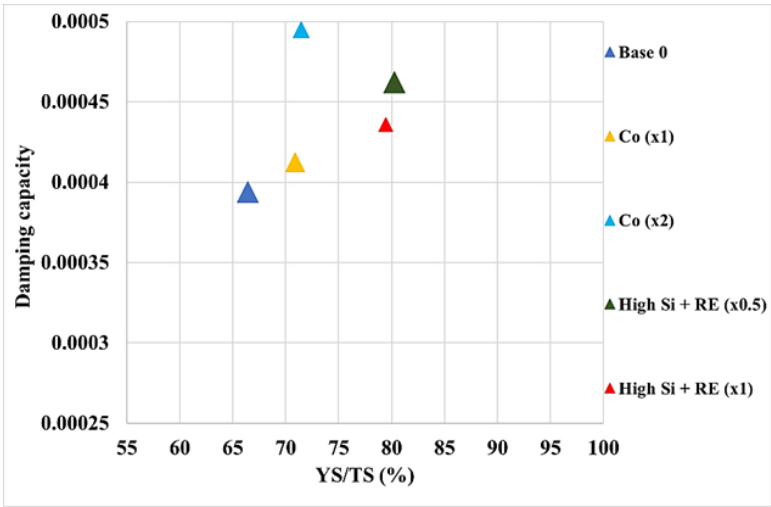
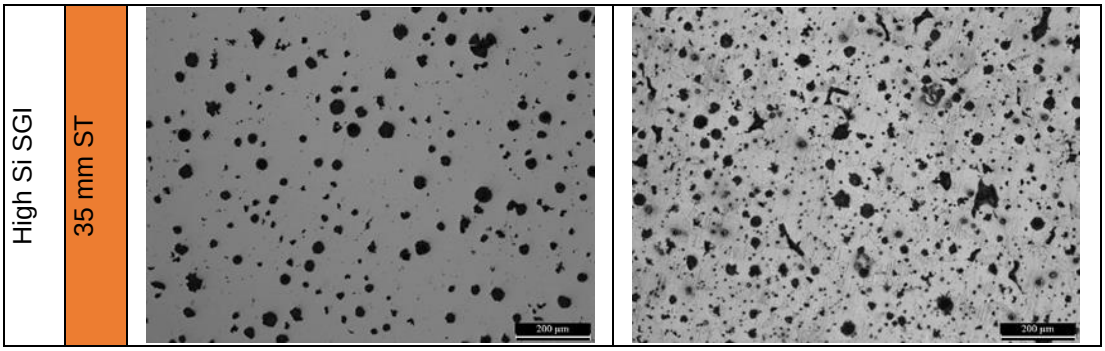


Figure 4 - 32. Damping capacity *vs.* the YS/TS ratio for the samples with 35 mm section thickness from the most promising alloyed SGIs from the first approach experiments.

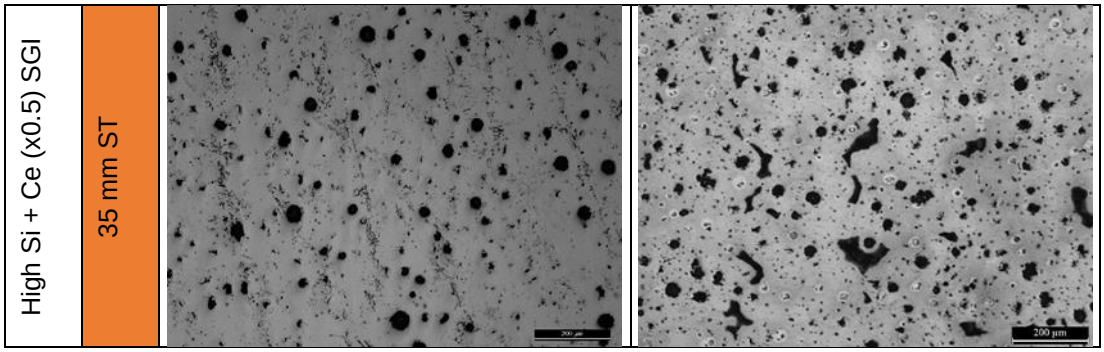
Figure 4 - 33 through Figure 4 - 35 show the microstructures relating to the High Si, High Si + Ce (x0.5) and High Si + Ce (x0.5) + Co SGIs. The corresponding microstructural parameters are presented in Table 4 - 37.

[6] A Ce alloy was used instead of the alloy comprising RE in its composition.



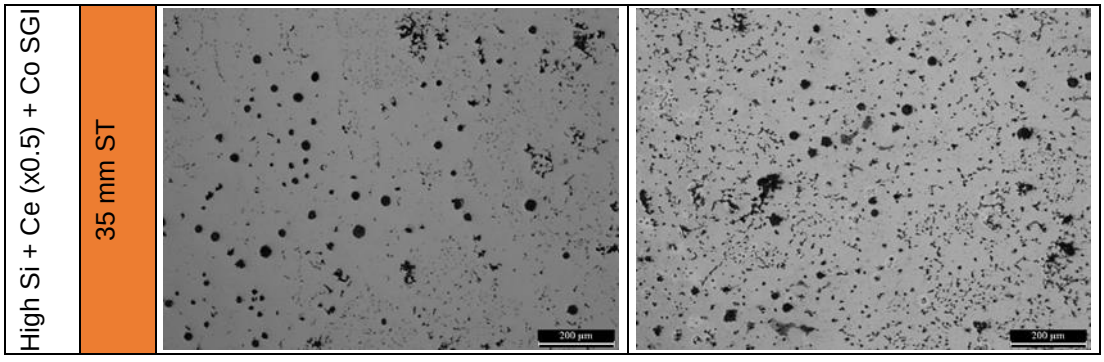
Before etching After etching

Figure 4 - 33. LOM micrographs of the High Si-alloyed SGI, for the sample with 35 mm section thickness.



Before etching After etching

Figure 4 - 34. LOM micrographs of the High Si + Ce (x0.5)-alloyed SGI, for the sample with 35 mm section thickness.



Before etching After etching

Figure 4 - 35. LOM micrographs of the High Si + Ce (x0.5) + Co-alloyed SGI, for the sample with 35 mm section thickness.

All samples present a fully ferritic matrix (*i.e.*, pearlite < 5%). On the other hand, while the sample relative to the High Si SGI shows a similar nodularity to the Base 2 SGI, a nodularity decrease and traces of chunky graphite were registered for the High Si + Ce (x0.5) and High Si + Ce (x0.5) + + Co SGIs.

Table 4 - 37. Microstructural parameters of the different alloyed SGIs of the fine approach trials, for the 35 mm section thickness

	Alloyed SGI	High Si	High Si + Ce (x0.5)	High Si + Ce (x0.5) + Co
35 mm ST	**Pearlite (%)**	5	5	0
	Graphite (%)	8.0	9.1	4.6
	Nodularity (%)	86	41	44
	Nodule count (particles/mm^2)	241	294	283
	Convex perimeter (µm)	61	61	45
	Graphite form-III (%)	2.8	36.6	39.0

Table 4 - 38 presents the variation of the damping capacity of the different alloyed SGIs developed for the fine approach experiments; an improvement in damping capacity was observed for all the samples.

It should be stressed that the most significant improvements were found for the samples with lower nodularity, as already observed in the first approach experiments.

Nevertheless, as will be seen later (sub-chapter 5.1.), damping capacity results from a combination of different microstructural features, corroborating the statements of several researchers already mentioned in sub-chapter 2.3.2.1. In the meantime, the 4% improvement registered for the High Si SGI might be only due to its ferritic matrix. On the other hand, the Base 2 SGI corresponds to a ferritic-pearlitic SGI, indicating, once again, that the modification of the matrix is only beneficial up to a certain level.

So, damping capacity seems to be predominantly affected by the graphite morphology and its fraction, as pointed out in sub-chapter 2.3.2.1.1.

Table 4 - 38. Variation of the damping capacity of the alloyed SGIs from the fine approach experiments

35 mm ST	Alloyed SGI	High Si	High Si + Ce (x0.5)	High Si + Ce (x0.5) + Co
	Damping capacity	0.000390	0.000441	0.000396
	Relative variation (%)	4	18	6
	CV estimated (%)	*± 1*		

In their turn, Table 4 - 39 and Table 4 - 40 show that the ultimate tensile and 0.2% offset yield strengths increased for the SGIs tested. It is relevant to notice that the lower nodularity did not negatively affect these mechanical properties, which might indicate that the SGI matrix has been strengthened by the Si alloying.

Table 4 - 39. Variation of the ultimate tensile strength of the alloyed SGIs from the fine approach experiments

35 mm ST	Alloyed SGI	High Si	High Si + Ce (x0.5)	High Si + Ce (x0.5) + Co
	Ultimate tensile strength (MPa)	496	503	**ND**
	Relative variation (%)	17	19	–
	CV estimated (%)	*± 7*		

ND – Not determined due to some defects in the sample

Table 4 - 40. Variation of the 0.2% offset yield strength of the alloyed SGIs from the fine approach experiments

35 mm ST	Alloyed SGI	High Si	High Si + Ce (x0.5)	High Si + + Ce (x0.5) + Co
	0.2% offset yield strength (MPa)	376	386	**ND**
	Relative variation (%)	22	25	–
	CV estimated (%)	± *6*		

ND – Not determined due to some defects in the sample

The results of elongation are presented in Table 4 - 41; an improvement in elongation, relative to the Base 2 SGI, was registered for the alloying combinations tested.

Table 4 - 41. Variation of the elongation of the alloyed SGIs from the fine approach experiments

35 mm ST	Alloyed SGI	High Si	High Si + Ce (x0.5)	High Si + Ce (x0.5) + Co
	Elongation (%)	24.6	17.1	**ND**
	Relative variation (%)	242	138	–
	CV estimated (%)	± *6*		

ND – Not determined due to some defects in the sample

Table 4 - 42 shows that Young's modulus decreased relative to the Base 2 SGI. The highest decrease was registered for the High Si + Ce (x0.5); this decrease is aligned with an increase in damping capacity.

Table 4 - 42. Variation of the Young's modulus of the alloyed SGIs from the fine approach experiments

35 mm ST	Alloyed SGI	High Si	High Si + Ce (x0.5)	High Si + Ce (x0.5) + Co
	Young's modulus (GPa)	170	167	170
	Relative variation (%)	-2.3	-4.0	0.0
	CV estimated (%)	*± 1.4*	*± 2.4*	*± 2.2*

As observed for the first approach experiments, the fundamental flexural frequency, shear modulus and Poisson's ratio are not significantly influenced by the variation of the section thickness (Annexe B.2.2.).

Finally, the data of Table 4 - 43 points for a significant hardness increase relative to the Base 2 SGI, confirming that these alloying combinations promoted the hardening of the matrix of the SGIs tested.

Table 4 - 43. Variation of the hardness of the alloyed SGIs from the fine approach experiments

35 mm ST	Alloyed SGI	High Si	High Si + Ce (x0.5)	High Si + Ce (x0.5) + Co
	Hardness (HBW 2.5/187.5)	169	173	232
	Relative variation (%)	13	16	55
	CV estimated (%)	*± 5*		

5. Discussion of Results

Chapter 5 presents an overall analysis and discussion of the results.

5.1. Overall analysis

The braking system zero noise represents one of the first five objectives to be achieved by OEMs [11].

High-damping materials are used to reduce vibration and noise [12]. Hence, the thesis's strategy consisted of studying the damping capacity of a new SGI to be used by *AAPICO* to produce the anchor and calliper for the automotive braking system. The purpose was to improve the damping capacity of these brake components without compromising the industry standards and customers' requirements in terms of mechanical properties. The main goal is to promote the dissipation of the brake disc vibration through these critical safety components.

As *AAPICO* is currently producing the anchor and the calliper in a pearlitic-ferritic SGI, a characterization of the damping capacity of this SGI relative to other cast alloys was performed.

The highest damping capacity was obtained for the FGI and the lowest for the Al cast alloys. Moreover, as corroborated by the results obtained for the CGI and FGI, the cast irons with non-spheroidal graphite present a higher damping capacity.

It was also verified that damping capacity varies with the matrix type, increasing in the following order: pearlitic SiboDur → ADI → pearlitic SGI → → ferritic SGI → ferritic SiboDur.

So, the pearlitic SGI produced by *AAPICO* presents a lower damping capacity than the CGI, FGI, alloyed-SGI-1 (ferritic SiboDur) and the ferritic SGI (also produced by *AAPICO*). At the same time, it shows a higher damping capacity than the alloyed-SGI-2 (pearlitic SiboDur), ADI, AlSi12Cu1 and AlSi9Cu3 (Figure 4 - 1).

The preliminary results pointed to, in order to obtain an SGI with higher damping capacity, the need to ensure that its matrix will be fully ferritic (*i.e.*, < 5% pearlite) and present lower nodularity. Therefore, the strategy was based on producing several alloyed-SGIs, which may influence either the matrix or the graphite morphology and its fraction. The damping capacity and mechanical properties of the SGIs developed were then evaluated.

The starting point was developing a test casting that would consider the impact of different cooling rates on the SGI microstructure and, consequently, on its mechanical properties; so, a step-casting geometry was used. Its design has considered the necessary dimensions for machining samples for tensile, IET and hardness tests, and microstructural analysis for each section thickness. The 45 – 5 mm range chosen for the section thicknesses was based on those from the braking system components actually produced by *AAPICO*.

The overall assessment of the results showed that damping capacity depends on the section thickness because the pearlite fraction increases for the thinner ones, inducing a drop in damping capacity.

In the fully ferritic SGI samples (*i.e.*, < 5% pearlite), for which there is no matrix modification with the section thickness, the damping variation will only result from the graphite features (morphology and distribution). This can be confirmed by the results of the Co-alloyed SGI samples (Figure 4 - 10 and Figure 4 - 11) since, for the samples from the 45 to 25 mm section thicknesses, the matrix is fully ferritic (*i.e.*, < 5% pearlite), being the slight damping capacity variations related to the graphite features (Table 4 - 11 and Table 4 - 12). In turn, the pearlite fraction increases for the 5 mm section thickness and, consequently, a significant drop in damping capacity was observed.

The most promising alloyed-SGIs from the first approach experiments, which presented the highest damping capacity improvement, were:

- High Si + RE (x1);
- High Si + RE (x0.5);
- Co (x2),

which presented a damping increase, relative to the Base 0 SGI, up to 32%, 29% and 26%, respectively.

These alloyed SGIs present a fully ferritic (*i.e.*, < 5% pearlite) matrix and a nodularity in the range of 41-85% for section thicknesses in the range of 5--45 mm. The results allow us to conclude that both matrix type and graphite features influence the damping capacity of the SGI.

Effectively, an increase of the damping capacity, relative to the Base 0 SGI, was registered for the High Si-alloyed SGI samples (Figure 4 - 4), which present a fully ferritic matrix (*i.e.*, pearlite < 5%) and no variation in graphite features (Table 4 - 4). On the other hand, a higher damping capacity increase was observed for the samples from the Co and High Si + RE trials (Figure 4 - 13 and Figure 4 - 26, respectively) that bedsides presenting a fully ferritic matrix show a variation in the graphite features.

Moreover, considering the fraction of pearlite in the matrix of the samples from the 5 mm section thickness, Si seems to be a more potent ferritizer than Co (Table 4 - 11 and Table 4 - 12).

Finally, the samples from the Cu or Mo alloying experiments show a decrease in damping capacity (Table B. 7 through Table B. 9), which is assumed to be related to an increase in the pearlite fraction. Besides, the results relative to the samples with a pearlitic-ferritic matrix (Base 1, Co + + Ce (x0.5) and Co + Ce (x1)) also confirm that an increase of the fraction of ferrite improves damping capacity (Table B. 11 through Table B. 14).

Regarding the graphite features, a nodularity decrease is associated with a higher damping capacity. In addition, it is seen that a nodularity decrease will not necessarily induce, by itself, a significant damping increase. This fact can be corroborated by the results of the RE-alloyed SGI experiments, in which a nodularity decrease was observed but with no significant impact on its variation (Figure 4 - 19) since pearlite formation has also occurred.

In its turn, a high nodularity might be, in some cases, associated with higher damping capacity; however, this analysis should be established between SGIs presenting different matrices and similar nodularity (Figure 4 - 5).

Only when combining several alloying elements, which can induce an increase of the ferrite fraction in the matrix (*e.g.*, Si) and promote the

precipitation of graphite nodules with irregular shapes (*e.g.*, RE), a damping capacity increase was achieved for all the section thicknesses (Figure 4 - 26 and Table 4 - 38).

In the meantime, it was verified that the ultimate tensile strength and yield strength did not drop for these alloyed SGIs (Figure 4 - 14 and Figure 4 - 27); the nodularity decrease has been overtaken by the strengthening of the matrix (ferrite) by Si and Co. It should be noticed that the standard EN-1563:2011 [58] contemplates that approximately 20% of graphite form-III can be accepted on solid solution strengthened ferritic SGI. Also, it was observed that Si has a more significant impact on increasing the tensile properties than Co (Table 4 - 6 and Table 4 - 14, respectively), as will be discussed further in sub-chapter 5.3.

Literature refers that a 20% decrease in pearlite fraction might induce a drop of approximately 50 MPa in the tensile strength (Figure 2 - 13). In this thesis, the reduction from 25% pearlite (Base 0 SGI) to 0% pearlite (High Si and Co-alloyed SGIs) induced an increase of the tensile strength between 50 and 140 MPa (Figure 4 - 6 and Figure 4 - 14). Once again, this indicates that these elements promoted the strengthening of the ferrite.

A hardness increase was registered for all the fully ferritic samples, also indicating a strengthening of the matrix for the High Si, Co, High Si + RE, High Si + Ce(x0.5), and High Si + Ce(x0.5) + Co SGIs (Table 4 - 10, Table 4 - 18, Table 4 - 33, Table 4 - 43, respectively). Additionally, it is seen that the increase relative to the base sample is as higher for fully ferritic as for pearlitic SGIs, indicating that the matrix strengthening induced by these alloying elements is comparable to the one promoted by the increase of the pearlite fraction in the matrix.

Finally, in the particular case of the Al-alloyed SGIs, which were studied on both approaches, their production was challenging due to the high viscosity of the melts and slag formation.

Al alloying induced significant deformation of the graphite nodules for both experiments (Annexe B). Al (x1)-alloyed SGI showed an increase in the tensile and yield strengths and a decrease in damping capacity and elongation. Nevertheless, it was impossible to determine the damping capacity and tensile

properties of the Al (x5)-alloyed SGI due to the impossibility of machining the test samples (high hardness).

A significant increase in hardness, relative to the base SGIs, was obtained for both compositions: 49% for Al (x1) and 67% for Al (x5). Based on these limitations, it was decided not to pursue the studies with the Al-alloyed SGI.

5.2. Model for estimating the SGI damping capacity

A multiple linear regression analysis was selected to develop the model to estimate the SGI damping capacity due to the number of microstructural features (independent variables > 2 that might influence it, such as ferrite fraction, nodularity, fraction of graphite, convex perimeter, among others.

The multiple variables were studied since each effect cannot be evaluated individually. For instance, a slightly deformed and big nodule would present a high convex perimeter, which seems to be associated with higher damping capacity; however, it would not influence the nodularity decrease since it would still correspond to graphite nodules of forms V or IV. This can also be seen by analysing only the convex perimeter of the base SGI samples from the first approach experiments, which presented the highest values; however, this does not promote a higher damping capacity since the nodularity is high and the samples present a ferritic-pearlitic matrix.

A first model was developed, considering only the fractions of the two main constituents (ferrite and graphite) in the matrix:

$$Q^{-1} = 7.592x10^{-5} + 2.837x10^{-6}\,(F) + 5.474x10^{-6}\,(G) \qquad (10)$$

with:

(Q^{-1}) – Internal friction;
(F) – Fraction of ferrite (%);
(G) – Fraction of graphite (%).

The model considers all the results from the first and fine approaches experiments. As aforementioned, the pearlitic-ferritic samples were not considered (trials relative to Base 1 of the fine approach experiments).

The analysis revealed a statistically significant model [$p < 0.001$; $R = 0.674$; $R^2 = 0.454$], although with a moderate correlation factor.

The damping capacity can be estimated at around 45% by the set of predictor variables: % ferrite ($\beta = 0.629$; $p < 0.001$) and % graphite ($\beta = 0.209$; $p = 0.049$).

The model reveals that the increase of the fractions of ferrite and graphite improves damping capacity. It is noticed that the model highlights that the ferrite fraction has the most decisive impact on damping capacity since the value (0.629) of β associated with this predictor is higher than for the fraction of graphite ($\beta = 0.209$). However, other predictor variables should be considered for explaining the remaining 55% of the damping capacity estimation.

So, a deep analysis was undertaken on other graphite features that could be influencing the SGI damping capacity.

The second model developed only considered ferritic (% pearlite ≤ 25%[7]) matrices from the fine and first approach experiments:

$$Q^{-1} = 3.992\text{x}10^{-6}\,(F) + 3.586\text{x}10^{-6}\,(\textit{Convex}P) + 1.760\text{x}10^{-6}\,(\text{III-form}) \qquad (11)$$

with:

(Q^{-1}) – Internal friction;
(F) – Fraction of ferrite (%);
(*Convex*P) – Convex perimeter (µm);
(Form-III) – Fraction of graphite form-III (%).

Note: the model doesn't comprise any independent term.

[7] Fraction of pearlite accepted by *AAPICO* for its ferritic SGI.

The analysis points to a statistically significant model [$p < 0.001$; $R = 0.851$; $R^2 = 0.724$], with a strong correlation factor, indicating that damping capacity is estimated at 72% by the set of predictor variables: % ferrite ($\beta = 0.628$; $p < 0.001$), convex perimeter ($\beta = 0.590$; $p < 0.001$) and % graphite form-III ($\beta = 0.267$; $p = 0.003$).

The analysis of the results of the multiple linear regression (Table 5 - 1) shows that all assumptions (sub-chapter 3.1.4.7) were fulfilled.

Table 5 - 1. Analysis of the assumptions of the multiple linear regression

Assumption	Results	
1	44 cases per independent variable	Fulfilled
2	Ferrite: Tolerance = 0.982 and VIF = 1.019 Convex Perimeter: Tolerance = 0.982 and VIF = 1.018 Form-III: Tolerance = 0.999 and VIF = 1.001	Fulfilled
3	Standard predicted value: -2.415 to 2.116 Standard residual: -1.735 to 2.755	Fulfilled
4	Acceptable fitting (Figure 5 - 1 and Figure 5 - 2)	Fulfilled
5	Values randomly scattered (Figure 5 - 3)	Fulfilled
6	Residuals randomly scattered around 0 (Figure 5 - 3)	Fulfilled

The residuals' histogram and predicted probability (P-P) plot of residuals (Figure 5 - 1 and Figure 5 - 2, respectively) help to analyse whether the variance is normally distributed.

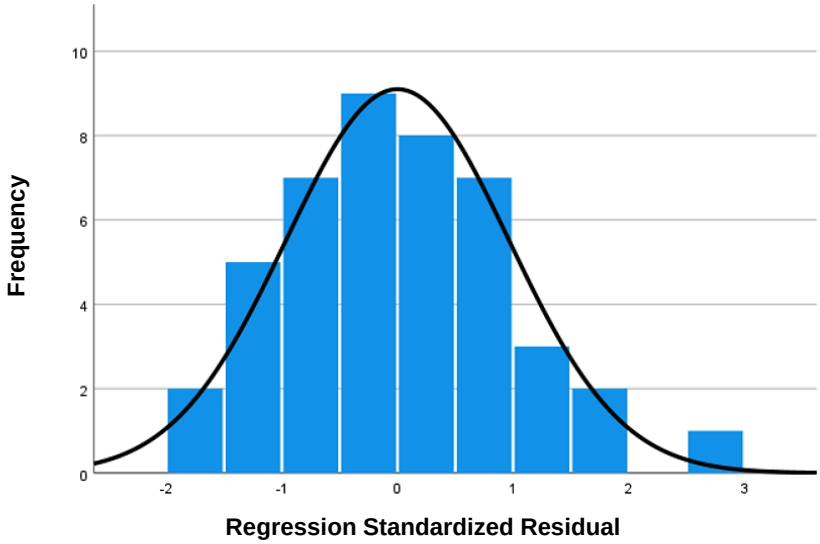


Figure 5 - 1.

Residuals' histogram.

The histogram shows a good fitting with a standardized normal distribution curve, whereas the P-P plot reveals that the two cumulative distribution functions (expected and observed) are similar since there is a good fitting with a straight line.

The histogram and P-P plot indicate that assumption 4 (Table 5 - 1) is fulfilled.

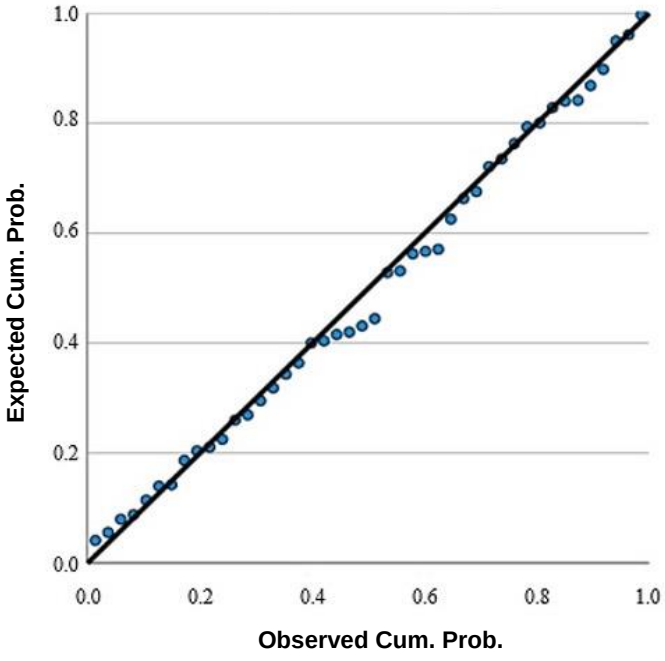


Figure 5 - 2. Plot of the predicted probability (P-P) for residuals.

On the other hand, the residuals' scattering plot (Figure 5 - 3) assesses both homoscedasticity and linearity, *i.e.*, whether the variance is constant and if there is a linear correlation between the dependent and independent variables.

The plot reveals that the values are randomly scattered, with the points roughly distributed along a rectangular area, indicating that the variance is constant and that assumption 5 (Table 5 - 1) is fulfilled. Moreover, they are mostly scattered around the horizontal line at y = 0, indicating that assumption 6 (Table 5 - 1) is also fulfilled and there is a linear correlation between the variables.

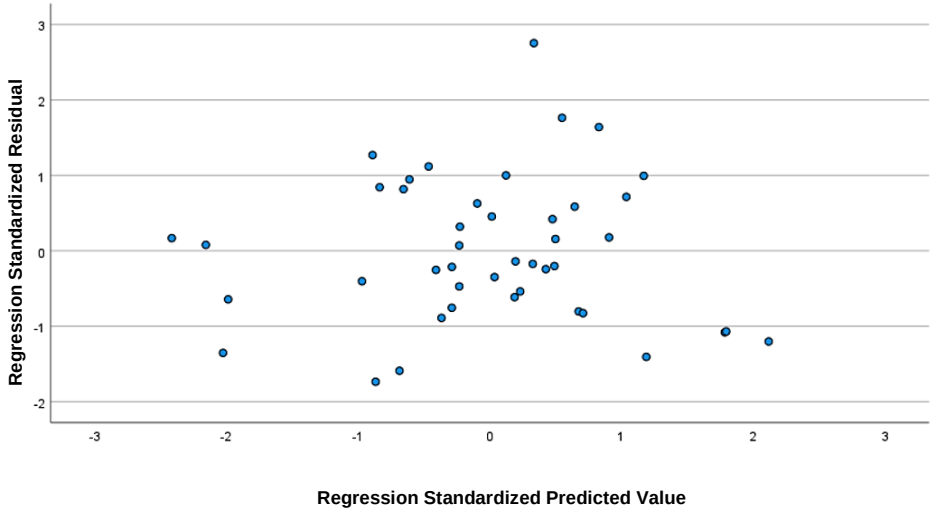


Figure 5 - 3. Residuals' scattering.

The model reveals that the increase of the fractions of ferrite and graphite form-III and its convex perimeter promote the increase in SGI damping capacity. The increase in the graphite average length also promotes the increase of the damping capacity; however, as the convex perimeter is strongly correlated with the graphite length, this variable was not included in the model.

The damping capacity is more related to the morphology of the graphite precipitates (evaluated by the convex perimeter and % graphite form-III) than their fraction in the matrix since its inclusion gave rise to a model with a more robust statistical significance (R^2 = 0.724 *vs.* R^2 = 0.454).

The standardized coefficients (β) are higher for the fraction of ferrite and convex perimeter. Therefore, they are more effective in increasing the damping capacity than the fraction of graphite form-III. This indicates that, for an SGI, the damping capacity increases with the fraction of vermicular graphite and more predominately with graphite completely degenerated (evaluated by the convex perimeter).

Additionally, a model involving the fraction of ferrite, convex perimeter and nodularity as predictors was developed (Annexe C). The model showed that the decrease in nodularity and the increase of the ferrite fraction and convex perimeter induce a damping improvement, with nodularity presenting a lower impact.

5.3. The most promising alloyed SGIs tested

The best compromise between damping capacity improvement and the tensile properties of alloyed SGIs was pursued in this thesis. Therefore, an in-depth study was performed for the most promising compositions (alloys developed that presented a damping capacity improvement).

The analysis of the different results focused on the samples from the sections of the step-castings with 35 mm thickness because more data from the first and fine approaches experiments were obtained.

The samples relative to the Co (x2), High Si + RE and High Si + + Ce (x0.5) compositions from the first approach experiments present an increase in the damping capacity and, simultaneously, of the Yield Strength/Tensile Strength (YS/TS) ratio (Figure 5 - 4). High Si + RE and High Si + Ce (x0.5) SGIs show a YS/TS ratio between 75% and 80%, which fits in the range established by the DIN EN 1563:2011 standard for solution-strengthened ferritic SGI (75% to 85%) [58].

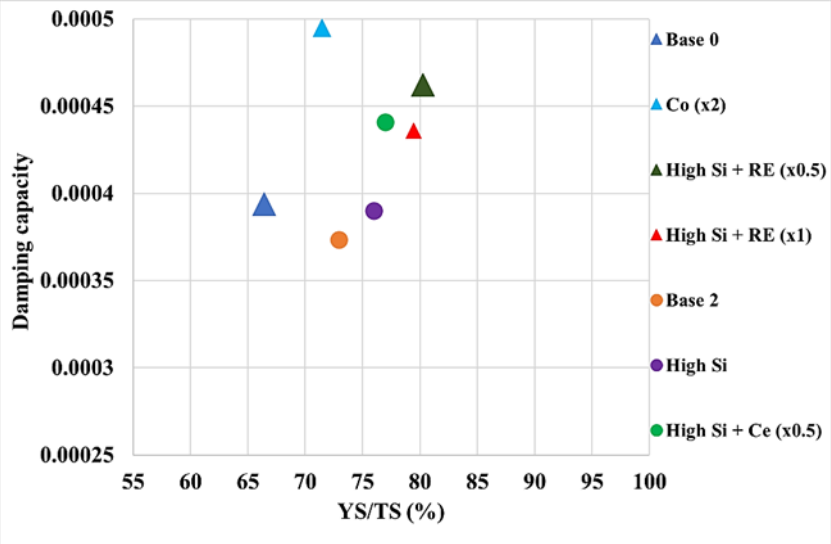


Figure 5 - 4. Damping capacity *vs.* the YS/TS ratio for the samples with 35 mm section thickness from the most promising alloyed SGIs.

In addition, a hardness increase was observed for the High Si + RE compositions (Table 4 - 33), confirming that Si effectively strengthens the ferrite by solid solution.

In its turn, the YS/TS ratio for the Co (x2)-alloyed SGI is not in the range established by the DIN EN 1563:2011 standard; however, its high hardness values (Table 4 - 18) might indicate that Co will also strengthen the ferrite, however, not so intensively as Si.

A high YS/TS ratio may allow product engineers to adjust the design of the castings since a “new” SGI, presenting higher damping capacity while keeping or even increasing its strength and elongation, can be used. It is believed that it will be possible to reduce the wall thickness of the castings and, consequently, promote their weight reduction. Additionally, the single-phase matrix obtained for all these alloyed-SGIs will contribute to the improvement of their machinability.

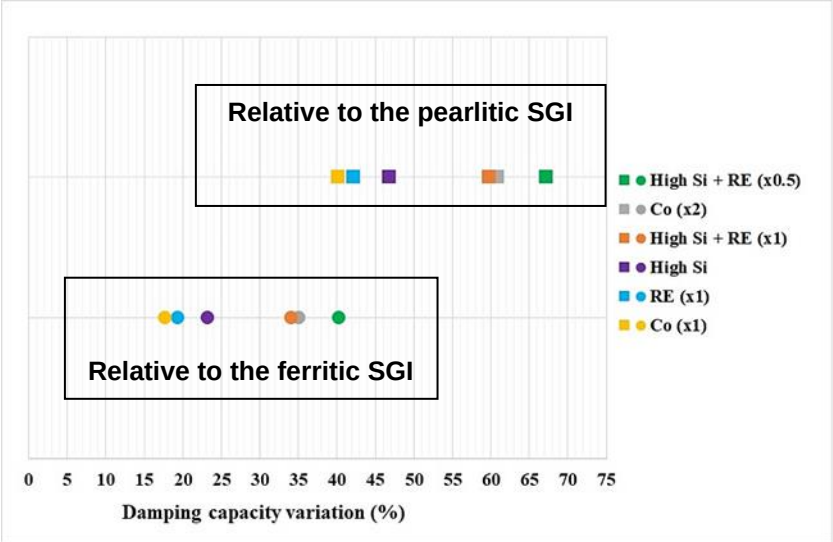
This thesis shows that damping capacity increase can be associated with a higher YS/TS for a slightly lower Young’s modulus.

Thus, after verifying that the mechanical properties requested for the SGI to be used were maintained, an additional study was conducted to select the most promising composition to be validated by *AAPICO* in its plant.

The most promising materials from the first and fine approaches were compared with two SGIs already produced by the enterprise: a ferritic SGI (% pearlite ≤ 25%) and a pearlitic SGI (75% < pearlite ≤ 100%).

The mean damping capacity for all the evaluated section thicknesses was determined for each composition, and then analysed the damping variation relative to a ferritic and a pearlitic SGI (Figure 5 - 5).

Figure 5 - 5 points to the High Si + RE (x0.5)-alloyed SGI as the first choice since it corresponds to the highest damping capacity improvement. The improvements in the damping capacity relative to the ferritic and pearlitic SGIs currently produced by *AAPICO* were 40% and 67%, respectively. This difference arises from the fact that the High Si + RE (x0.5) is an SGI with a fully ferritic matrix (*i.e.*, pearlite < 5%) and, therefore, compared with a SGI with, for instance, 75% pearlite (pearlitic SGI), the damping variation would be higher than compared with an SGI with, for example, 20% pearlite (ferritic SGI).



Obs: The trials from the fine approach haven´t been considered due to the impossibility of obtaining the mean damping capacity (only one section thickness was tested)

Figure 5 - 5. Variation of the damping capacity of the most promising alloying combinations relative to the ferritic and pearlitic SGIs produced by *AAPICO*.

Co (x2)-alloyed SGI would potentially be the second choice. For instance, it presents a higher damping capacity than the High Si-alloyed SGI, probably due to its lower nodularity (the matrix is fully ferritic for 45 mm through

15 mm section thicknesses). However, besides having higher associated production costs, the results have shown that Co is less effective in strengthening the ferrite than Si.

Moreover, Si appears to be a stronger ferritizer and graphite promoter than Co. For instance, literature [63, 126-128] indicates that the Si and Co atoms form a substitutional solid solution in ferrite. Co presents a similar atomic size to Fe, whereas Si has a smaller one. It also indicates that the strengthening effect is higher with an increase in the mismatch in atomic size; therefore, the higher mismatch between the atomic sizes of Si and Fe potentially induces a higher strengthening of the ferrite.

Therefore, it was established that the most promising material would be the High Si + RE (x0.5)-alloyed SGI since, as already seen, it presents the more significant damping capacity improvement while increasing (or at least keeping) the required mechanical properties.

5.4. Validation of the experiments at the industrial plant

AAPICO accepted to develop an industrial experiment with one of the alloyed SGIs, which revealed quite promising. The High Si + Ce (x0.5)-alloyed SGI was first selected. In the meantime, considering the mass of Ce alloy to be added to the pouring ladle to reach the composition, the experiment focused on the High Si SGI.

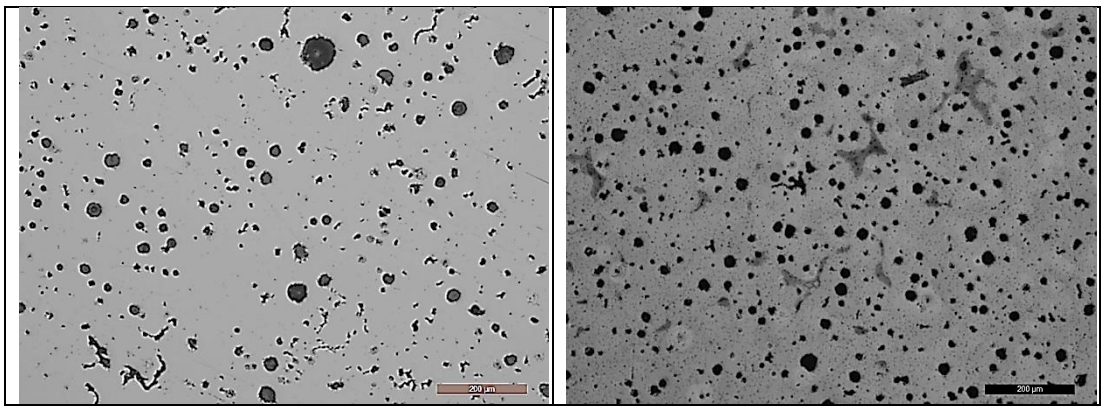
The castings to be tested were produced following the standard procedures adopted by the enterprise. However, to compensate for the effect of Ce alloying, the cores were previously removed from the moulds to be poured. Therefore, graphite degeneration was induced by a lower cooling rate due to the removal of the cores.

Lastly, the parts produced were the object of the following control: X-ray observation for defects control, tensile, hardness and IET, and microstructure analysis.

Figure 5 - 6 shows the microstructures of the samples: graphite nodules and degenerated graphite distributed in a ferritic matrix comprising some residual pearlite (< 5%).

Due to the high Si content, compacted graphite precipitates (form-III) could be observed (~14%).

It seems that the strengthened ferritic matrix overtook the impact of the low nodularity (70%) on the mechanical properties.



Before etching After etching

Figure 5 - 6. LOM micrographs of the High Si-alloyed SGI, with degenerated graphite.

Table 5 - 2 presents the results of the tests carried out over two castings from which two samples have been machined.

An improvement of the damping capacity was achieved regarding the ferritic and pearlitic SGIs current produced by *AAPICO*, respectively, 54% and 84%.

The results reveal that the minimum tensile strength required (550 MPa) for the castings was not reached, but just by a slight difference (16 MPa; ~3%); nevertheless, the minimum yield strength required (370 MPa) was obtained. Moreover, a high YS/TS ratio is observed (~81%), being one of the characteristic properties of a solution strengthened ferritic SGI. The elongation obtained is considerably higher than the minimum target (5%).

The minimum hardness required for calliper and anchor parts (190 HBW) was not also achieved only by a slight difference. The hardness obtained (189 HBW) indicates that the matrix strengthening by Si is comparable to the one induced by the pearlite in the matrix.

Table 5 - 2. Results of the industrial validation of the High Si SGI with degenerated graphite

Damping capacity	0.000471
CV estimated (%)	*± 1%*
Fundamental flexural frequency (Hz)	4200
CV estimated (%)	*± 0.004%*
Young's modulus (GPa)	164
CV estimated (%)	*± 0.2%*
Shear modulus (GPa)	65
CV estimated (%)	*± 0.2%*
Poisson's ratio	0.264
CV estimated (%)	*± 0.6%*
Ultimate tensile strength (MPa)	534
CV estimated (%)	*± 7%*
0.2% offset yield strength (MPa)	432
CV estimated (%)	*± 6%*
Elongation (%)	8.1
CV estimated (%)	*± 6%*
YS/TS ratio	0.81
Hardness (HBW 2.5/187.5)	189
CV estimated (%)	*± 5%*
Pearlite (%)	< 10
Graphite (%)	6.3
Nodularity (%)	70
Nodule count (particles/mm^2)	316
Convex perimeter (µm)	49
Graphite form-III (%)	14.1

6. Conclusions and Future Works

Chapter 6 presents the conclusions of the investigation developed under the scope of this thesis.

The metallurgical characteristics of any component have a crucial impact on its mechanical properties.

The need to suppress NVH originated the development of new alloys with high damping capacity while keeping the required mechanical properties. High damping capacity is a desirable property for many applications where it is crucial to minimize the resonant amplitude and, consequently, decrease the operating stresses to which the parts are submitted. Thus, a high damping capacity material may minimize NVH problems induced by the components of the braking system.

This thesis presents the development of alloyed SGIs and how they induce different metallurgical characteristics with influence on the damping capacity. The impact of the cooling rate was also approached by producing step-castings with different section thicknesses and, therefore, a range of microstructures.

The overall assessment of the results shows that the damping capacity depends on the section thickness of the step-castings because, for thinner ones, the fraction of pearlite increases, which causes a drop in damping capacity.

The damping capacity of different standard alloys was determined to benchmark the SGIs actually used by *AAPICO* for producing critical safety components for the automotive industry. It was found that the standard pearlitic SGI has a damping capacity ~70% lower than CGI and ~350% lower than FGI tested.

The highest damping improvement (> 15%) was reached for the High Si + RE (x0.5) and Co (x2) compositions; fully ferritic (*i.e.*, pearlite < 5%) SGIs with a nodularity in the range of 41-85% (depending on the section thickness) were obtained.

The ferritizing effect of Si and Co was confirmed. In turn, Co, RE and Ce alloying promoted some graphite degeneration.

The increase of the ferrite fraction and decrease of nodularity did not induce the decrease of the mechanical properties due to the effect of solid solution strengthening of the matrix by Si and Co alloying.

In the meantime, despite the ferrite fraction being a reliable predictor for the damping capacity estimation, this property also depends on other microstructural features, such as the fraction of graphite form-III and its convex perimeter. Therefore, a multiple-variable regression model was developed for its estimation.

The data analysis resulted in a statistically significant model [$p < 0.001$; $R = 0.851$; $R^2 = 0.724$], stressing that a set of predictor variables influences the SGI damping capacity. The model shows that increasing the fraction of ferrite or graphite form-III or its convex perimeter raises the SGI damping capacity, with the fraction of ferrite presenting the highest impact in its variation.

The automotive industry is also aiming for the weight reduction of the different components, which can be partially obtained by using SGI castings with a high ratio of YS/TS that will allow to reduce their wall thickness. In the research developed, the alloyed SGI with more significant damping capacity improvement also presents a high YS/TS ratio due to the ferrite strengthening by the Si and Co alloying.

The beneficial impact of this research on the automotive industry lies in the possibility of increasing the damping capacity of SGI without compromising its tensile strength by balancing the graphite degeneration and strengthening the ferritic matrix.

Concluding, a set of remarks could be drawn:

- The SGI damping capacity can be increased by obtaining a fully ferritic matrix (*i.e.*, pearlite < 5%) with uniform dispersed graphite nodules presenting low nodularity;

- The tensile and yield strengths could be maintained or even increased, despite the high range of nodularity obtained, due to the strengthening of the ferritic matrix.

  The matrix strengthening induced by the Si and Co alloying is comparable to the one promoted by the presence of pearlite in the matrix. So, the matrix strengthening overtakes the detrimental effect of graphite degeneration on the tensile properties;

- The production of SGIs presenting a higher YS/TS ratio may lead to the production of lightweight components due to the decrease in their wall thickness.

6.1. Future works perspectives

After completing this research, which primarily pointed to finding the best compromise between the required tensile properties and damping capacity of SGI, it would be essential to characterize the fatigue behaviour of the most promising alloys tested. Its evaluation would be necessary to verify the influence of nodularity decrease on the customer's requirements for the anchor and calliper of the braking system produced by *AAPICO*.

Further investigation is necessary to continue developing and adjusting the promising alloyed SGI and its production process. For instance, the upper limit of Si content for the improvement of damping capacity should be established because the results show that %Si > 4.5% (combined with Co and Ce alloying) did not significantly increase the damping capacity. In addition, it is crucial to study the best compromise between degenerated graphite and strengthened matrix.

In applications where pearlitic SGI is used, it would be necessary to clarify the effect of interlamellar spacing of this microconstituent on damping capacity.

This thesis deals with the SGI mechanical properties at room temperature. A natural extension of this work would be evaluating these properties, particularly damping capacity at higher temperatures, considering

the operating temperatures at which the brake components are subjected in operation. For instance, the evaluation could be performed from room temperature up to 220ºC, the maximum operating temperature recommended for a brake calliper.

A higher intrinsic damping capacity of the parts could reduce the noise induced by the braking system; therefore, in further studies, it would be crucial to evaluate the noise level in the braking system comprising the calliper and anchor parts produced with the developed alloy.

References

1. *Council Directive 86/188/EEC of 12 May 1986 on the protection of workers from the risks related to exposure to noise at work*. 1986. In: Åberg, J., *On the experimental determination of damping of metals and calculation of thermal stresses in solidifying shells*. PhD thesis, KTH Royal Institute of Technology, 2006.
2. Åberg, J., *On the experimental determination of damping of metals and calculation of thermal stresses in solidifying shells*. PhD thesis, KTH Royal Institute of Technology, 2006.
3. Bein, T.*, et al.*, *Advanced materials and technologies for reducing noise, vibration and harshness (NVH) in automobiles*, Advanced Materials in Automotive Engineering. 2012, pp. 254-298.
4. Canali, R.J., *Determinação de propriedades físicas de diferentes materiais para discos e pastilhas de freio e relação destas propriedades com ruído*. MSc thesis, Escola de Engenharia, Universidade Federal do Rio Grande do Sul, 2002.
5. Kinkaid, N.M., O'Reilly, O.M. and Papadopoulos, P., *Automotive disc brake squeal*. Journal of Sound and Vibration, 2003, 267(1). pp. 105-166.
6. Panza, M.A., *A review of experimental techniques for NVH analysis on a commercial vehicle*. Energy Procedia, 2015, 82, pp. 1017-1023.
7. Mayer, D., Militzer, J. and Bein, T., *Integrated solutions for noise and vibration control in vehicles*. SAE International Journal of Passenger Cars-Mechanical Systems, 2014, 7, pp. 1183-1193.
8. Papinniemi, A., Lai, J.C. and Zhao, J., *Brake squeal: a literature review*. Applied Acoustics, 2002, 63, pp. 391-400.
9. Hiller, M.B., *Correlation between parameters of the tribosystem and automotive disc brake squeal*. PhD thesis, University of Paderborn, 2006.
10. Oberst, S. and Lai, J., *Squeal noise in simple numerical brake models*. Journal of Sound and Vibration, 2015, 352, pp. 129-141.
11. Continental. *Leverage R&D&I foundry initiatives*, in *Foundry on Wheels Conference*, Águeda, Portugal, October 19-20, 2017.
12. *ASM Handbook, Volume 1 - Properties and Selection: Irons, Steels, and High-Performance Alloys*. ASM Intl.: Cleveland, OH, USA, 1990.
13. Halderman, J.D. and Mitchell, C.D., *Automotive Brake Systems*. Vol. 2. 2000, Upper Saddle River, N.J.: Prentice-Hall.
14. Wang, X., *Vehicle Noise and Vibration Refinement*. 2010, Elsevier.
15. Day, A., *Braking of Road Vehicles*. 2014, Butterworth-Heinemann.
16. Beards, C., *Structural Vibration: Analysis and Damping*. 1996, Elsevier.
17. Fahy, F. and Walker, J., *Advanced Applications in Acoustics, Noise and Vibration*. 2004, Spon Press.
18. Mazlee, M.*, et al.*, *Damping behaviour of as-received and as-cast Al-Si-Mg alloys*, in National Metallurgical Conference 2007 (NMC 2007), Johor, Malaysia, November 26-27, 2007.
19. Angus, H.T., *Cast Iron: Physical and Engineering Properties*. 2nd ed. 1976, Butterworths.

20. Rao, S.S., *Mechanical Vibrations*. 2005, Pearson Prentice Hall.
21. Paun, V.-P.*, et al.*, *On the energy dissipation capacity and the shape memory. A comparative study between polymer composites and alloys*. Materiale Plastice, 2010, 47(2). pp. 158-163. In: Crăciun, R., *et al.*, *Metallic materials for mechanical damping capacity applications*, in *IOP Conference Series: Materials Science and Engineering*, 2016. 012031. IOP Publishing.
22. Crăciun, R.*, et al.*, *Metallic materials for mechanical damping capacity applications*, in *IOP Conference Series: Materials Science and Engineering*, 2016. 012031. IOP Publishing.
23. Silva, C.W., *Vibration Damping, Control, and Design*. 2007, CRC Press.
24. Musolino, B., *Algoritmo de determinação do coeficiente de amortecimento em materiais refratários de alta alumina*. MSc thesis, Escola de Engenharia de São Carlos, Universidade de São Paulo, 2011.
25. Brebels, A. and Bollen, B., *Non-destructive evaluation of material properties as function of temperature by the Impulse Excitation Technique*, The e-Journal of Nondestructive Testing, 2015, Vol. 20(6).
26. Beranek, L.L. and Vér, I.L., *Noise and Vibration Control Engineering - Principles and Applications*. 1992, John Wiley & Sons, INC.
27. Kareem, A. and Gurley, K., *Damping in structures: its evaluation and treatment of uncertainty*. Journal of Wind Engineering and Industrial Aerodynamics, 1996, 59, pp. 131-157.
28. Blanter, M.S.*, et al.*, *Internal Friction in Metallic Materials: A Handbook*. 2007, Springer.
29. Ritchie, J.G. and Pan, Z.-L., *High-damping metals and alloys*. Metallurgical Transactions A, 1991, 22A, pp. 607-616.
30. Zhang, Z., Perez, R. and Lavernia, E., *Documentation of damping capacity of metallic ceramic and metal-matrix composite materials*. Journal of Materials Science, 1993, 28, pp. 2395-2404.
31. Roebben, G.*, et al.*, *Impulse excitation apparatus to measure resonant frequencies, elastic moduli, and internal friction at room and high temperature*. Review of Scientific Instruments, 1997, 68 (12), pp. 4511-4515.
32. Rao, M.D., *Recent applications of viscoelastic damping for noise control in automobiles and commercial airplanes*. Journal of Sound and Vibration, 2003, 262, pp. 457-474.
33. Lima, P., *Obtenção e determinação da capacidade de amortecimento da liga Cu-14Al-4Ni pelo método de excitação por impulso*. MSc thesis, Faculdade do Gama, Universidade de Brasília, 2013.
34. Psiuk, B.*, et al.*, *Impulse Excitation Technique IET as a non-destructive method for determining changes during the gelcasting process*. Ceramics International, 2016, 42, pp. 3989-3996.
35. Wu, G.*, et al.*, *Damping properties of aluminum matrix-fly ash composites*. Materials Letters, 2006, 60(24), pp. 2945-2948.
36. *Standard Test Method for Dynamic Young's Modulus, Shear Modulus, and Poisson's Ratio by Impulse Excitation of Vibration*. Annual Book of ASTM Standards no. 3. 2001.

37. Latella, B.A. and Humphries, S.R., *Young's modulus of a 2.25 Cr-1Mo steel at elevated temperature*. Scripta Materialia, 2004, 51(7), pp. 635-639.
38. Schmidt, R., Wicher, V. and Tilgner, R., *Young's modulus of moulding compounds measured with a resonance method*. Polymer Testing, 2005, 24, pp. 197-203.
39. Pereira, A.*, et al.*, *Algoritmo para determinação do amortecimento de materiais cerâmicos pela técnica das frequências naturais de vibração via excitação por impulso*. Cerâmica, 2012, 58, pp. 229-237.
40. Montecinos, S., Tognana, S. and Salgueiro, W., *Determination of the Young's modulus in CuAlBe shape memory alloys with different microstructures by Impulse Excitation Technique*. Materials Science and Engineering: A, 2016, 676, pp. 121-127.
41. Mortezavi, V.*, et al.*, *Fatigue analysis of metals using damping parameter*. International Journal of Fatigue, 2016, 91, pp. 124-135.
42. IMCE – Integrated Material Control Engineering, *Manual Version 1.1 - RFDA basic*. Accessed on December 2019.
43. Roebben, G.*, et al.*, *The innovative impulse excitation technique for high-temperature mechanical spectroscopy*. Journal of Alloys and Compounds, 2000, 310, pp. 284-287.
44. Roebben, G.*, et al.*, *Assessment of the high temperature elastic and damping properties of silicon nitrides and carbides with the Impulse Excitation Technique*. Journal of the European Ceramic Society, 2002, 22, pp. 2501-2509.
45. Voiconi, T.*, et al.*, *Determination of elastic and damping properties for closed-cell aluminium foams using Impulse Excitation Technique*, in *Proceedings of XIIIth Youth Symposium of Experimental Solid Mechanics*, Děčín, Czech Republic, June 29 - July 2, 2014, pp. 141-145.
46. Bollen, B., *The Impulse Excitation Technique, an innovative NDT method for microstructure and mechanical properties characterization of refractory used in the aluminum industry*, in *AMAP Colloquium*, Aachen, February 16, 2016.
47. Popov, I.*, et al.*, *Application of Impulse Excitation Technique to Investigation of Concrete Damping and Its Changes at Early Ages*. DEStech Transactions on Engineering and Technology Research, 2016.
48. Tognana, S.*, et al.*, *Measurement of the Young's modulus in particulate epoxy composites using the Impulse Excitation Technique*. Materials Science and Engineering: A, 2010, 527, pp. 4619-4623.
49. Dreiman, N., Evensen, H. and Hendrickson, A., *The effect of material properties on the radiation of impact sound from cylinders*. Experimental Mechanics, 1979, 19(9), pp. 331-335.
50. *ASM Handbook Volume 15: Casting*. ASM Intl.: Cleveland, OH, USA, 1990.
51. *ASM Handbook Volume 9: Metallography and Microstructures*. ASM Intl.: Cleveland, OH, USA, 1990.
52. ISO-945, Microstructure of cast irons - Part 1: Graphite classification by visual analysis. 2008.

53. ISO-945, Microstructure of cast irons - Part 4: Determination of nodularity in spheroidal graphite cast irons. 2015.
54. Ribeiro, L.M.M., *Estudo da influência da velocidade de arrefecimento nas temperaturas de transformação de um ferro fundido nodular*. Private report, not published. 2006.
55. Azevedo dos Anjos, V.E., *Use of Thermal Analysis to control the solidification morphology of nodular cast irons and reduce feeding needs*. PhD thesis, University of Duisburg, Essen, 2015.
56. Labrecque, C. and Gagne, M., *Ductile iron: Fifty years of continuous development*. Canadian Metallurgical Quarterly, 1998, 37(5). 343-378.
57. Elkem. *Alloying elements and their effects in ductile iron*. Internal Technical Information 5, 2018.
58. DIN EN 1563: 2012 – *Spheroidal Graphite Cast Irons.* European Standards, 2012.
59. Kasvayee, K.A.*, et al.*, *Characterization and modeling of the mechanical behavior of high silicon ductile iron*. Materials Science Engineering: A, 2017, 708, pp. 159-170.
60. Foglio, E.*, et al.*, *Fatigue characterization and optimization of the production process of heavy section ductile iron castings*. International Journal of Metalcasting, 2017, 11(1). pp. 33-43. In: Kasvayee, K.A.*, et al.*, *Characterization and modeling of the mechanical behavior of high silicon ductile iron*. Materials Science Engineering: A, 2017, 708, pp. 159-170.
61. Bjorkegren, L. and Hamberg, K., *Silicon alloyed ductile iron with excellent ductility and machinability*, in Proceedings of the Keith Millis Symposium on Ductile Iron, Hilton Head Island, SC, USA, 2003. In: Kasvayee, K.A.*, et al.*, *Characterization and modeling of the mechanical behavior of high silicon ductile iron*. Materials Science Engineering: A, 2017, 708, pp. 159-170.
62. Stets, W.*, et al.*, *Solution strengthened ferritic ductile cast iron properties, production and application*. International Journal of Metalcasting, 2014, 8(2), pp. 35-40.
63. Glavas, Z., Strkalj, A. and Stojakovic, A., *The properties of silicon alloyed ferritic ductile irons*. Metalurgija, 2016, 55(3), pp. 293-296.
64. González-Martínez, R.*, et al.*, *Effects of high silicon contents on graphite morphology and room temperature mechanical properties of as-cast ferritic ductile cast irons. Part II: Mechanical properties*. Materials Science and Engineering: A, 2018, 712, pp. 803-811.
65. González-Martinez, R.*, et al.*, *Effects of high silicon contents on graphite morphology and room temperature mechanical properties of as-cast ferritic ductile cast irons. Part I: microstructure*. Materials Science and Engineering: A, 2018, 712, pp. 794-802.
66. Baer, W., *Chunky graphite in ferritic spheroidal graphite cast iron: formation, prevention, characterization, impact on properties: an overview*. International Journal of Metalcasting, 2019, 93(6), pp. 1-35.
67. McCluhan, T., *The effect of cerium on carbides in thin section ductile iron*. AFS Transactions, 1967, 75, pp. 372-375. In: Sheikh, M.A. and Iqbal, J., *Effect of lanthanum on nodule count and nodularity of ductile iron*. Journal of Rare Earths, 2007, 25, pp. 533-536.

68. Onsoien, M., *Microstructure evolution in ductile cast iron containing rare earth metals: Experiments, mechanisms and modelling*. PhD thesis, Norwegian University of Science and Technology, 1997. In: Choi, J.*, et al.*, *Effect of rare earth elements on microstructure formation and mechanical properties of thin wall ductile iron castings*. Materials Science and Engineering: A, 2004, 383, pp. 323-333.
69. Sheikh, M.A. and Iqbal, J., *Effect of lanthanum on nodule count and nodularity of ductile iron*. Journal of Rare Earths, 2007, 25, pp. 533-536.
70. Kanetkar, C.S., Cornell, H.H. and Stefanescu, D.M., *The influence of some rare earth (Ce-La-Pr-Nd) and yttrium in the magnesium ferrosilicon alloy on the structure of spheroidal graphite cast iron*. AFS Transactions, 1984, 92. pp. 417-428. In: Choi, J.*, et al.*, *Effect of rare earth elements on microstructure formation and mechanical properties of thin wall ductile iron castings*. Materials Science and Engineering: A, 2004, 383, pp. 323-333.
71. Choi, J.*, et al.*, *Effect of rare earth elements on microstructure formation and mechanical properties of thin wall ductile iron castings*. Materials Science and Engineering: A, 2004, 383, pp. 323-333.
72. Walton, C.F. and Opar, T.J., *Iron Castings Handbook: Covering Data on Gray, Malleable, Ductile, White, Alloy and Compacted Graphite Irons*. 1981, Iron Castings Society, Inc.
73. Ibrahim, M.M.*, et al.*, *Microstructure, hot oxidation resistance and damping capacity of Al-alloyed cast iron*. International Journal of Cast Metals Research, 2017, 30(2), pp. 61-69.
74. Hu, C.-H., Chen, M.-L. and Hu, C.-J., *Microstructure and mechanical properties of 4% cobalt and nickel alloyed ductile irons*. Materials Science and Engineering: A, 2007, 444, pp. 339-346.
75. Anjos, V.*, et al.*, *The use of Thermal Analysis to compare solidification pattern, and evaluate the performance of several inoculants in ductile iron*, in *71st World Foundry Congress*, Bilbao, May 19-21, 2014.
76. Hammersberg, P.*, et al.*, *Variation of tensile properties of high silicon ductile iron*. Materials Science Forum, 2018, 925, pp. 280-287.
77. Björkegren, L., *Ferritic ductile iron with higher silicon content*. Swerea SWECAST Report 941028, 1994. In: Hammersberg, P.*, et al.*, *Variation of tensile properties of high silicon ductile iron*. Materials Science Forum, 2018, 925, pp. 280-287.
78. Fuller, A.G., Emerson, P.J. and Sergeant, G.F., *A report on the effect upon mechanical properties of variation in graphite form in irons having varying amounts of ferrite and pearlite in the matrix structure and the use of nondestructive tests in the assessments of mechanical properties of such ions*. AFS Transactions, 1980, 80(09), pp. 21-50. In: *ASM Handbook Volume 15: Casting*. ASM Intl.: Cleveland, OH, USA, 1990.
79. Hamberg, K., Björkgren, L. and Sun, Z., *Chunky graphite in ductile iron, a literature survey*. Svenska Gjuteriföreningen, 2003, pp. 16-49.
80. Löblich, H., *Einfluss der Keimbildungsbedingungen auf die Entstehung von Chunky-Graphit in dickwandigem Gusseisen mit Kugelgraphit EN-GJS*. 2006. In: Baer, W., *Chunky graphite in ferritic spheroidal graphite*

cast iron: formation, prevention, characterization, impact on properties: an overview. International Journal of Metalcasting, 2019, 93(6), pp. 1-35.

81. Hartung, K., Knustad, O. and Wardenaer, K., *Chunky graphite in ductile cast iron castings-Theories and examples*. Indian Foundry Journal, 2009, 55. pp. 25-29. In: Baer, W., *Chunky graphite in ferritic spheroidal graphite cast iron: formation, prevention, characterization, impact on properties: an overview*. International Journal of Metalcasting, 2019, 93(6), pp. 1-35.
82. Petzschmann, U., *Vermeidung von Chunky-Graphit in dickwandigen Gussstücken aus Gusseisen mit Kugelgraphit*. Final report AiF-Vorhaben 16801 N, Institut für Gießereitechnik, Düsseldorf, 2013. In: Baer, W., *Chunky graphite in ferritic spheroidal graphite cast iron: formation, prevention, characterization, impact on properties: an overview*. International Journal of Metalcasting, 2019, 93(6). pp. 1-35.
83. Källbom, R., *Chunky graphite in heavy section ductile iron castings*. Thesis for the degree of Licentiate of Engineering, Chalmers University of Technology, Göteborg, Sweden, 2006. In: Baer, W., *Chunky graphite in ferritic spheroidal graphite cast iron: formation, prevention, characterization, impact on properties: an overview*. International Journal of Metalcasting, 2019, 93(6), pp. 1-35.
84. Sertucha, J.*, et al.*, *Statistical analysis of the influence of some trace elements on chunky graphite formation in heavy section nodular iron castings*. Metallurgical Materials Transactions A, 2013, (44), pp. 1159-1162. In: Baer, W., *Chunky graphite in ferritic spheroidal graphite cast iron: formation, prevention, characterization, impact on properties: an overview*. International Journal of Metalcasting, 2019, 93(6), pp. 1-35.
85. Borgström, H. and Fourlakidis, V., *A review of side-lined chunky graphite phenomena*, in *Proceedings of the 10th International Symposium on the Science and Processing of Cast Iron - SPCI10*, Mar del Plata, Argentina, November 10-13, 2014. In: Baer, W., *Chunky graphite in ferritic spheroidal graphite cast iron: formation, prevention, characterization, impact on properties: an overview*. International Journal of Metalcasting, 2019, 93(6), pp. 1-35.
86. Prinz, B.*, et al.*, *Untersuchung von ursachen von graphitentartungen bei gusseisen mit kugelgraphit in form von chunky-graphit*. Gießereiforschung, 1991, 43(3). pp. 107-115. In: Baer, W., *Chunky graphite in ferritic spheroidal graphite cast iron: formation, prevention, characterization, impact on properties: an overview*. International Journal of Metalcasting, 2019, 93(6), pp. 1-35.
87. Karsay, S. and Campomanes, E., *Control of graphite structure in heavy ductile iron castings*. AFS Transactions, 1970, 78. pp. 85-92. In: Baer, W., *Chunky graphite in ferritic spheroidal graphite cast iron: formation, prevention, characterization, impact on properties: an overview*. International Journal of Metalcasting, 2019, 93(6), pp. 1-35.
88. Gagné, M., *Heavy section ductile iron. Part II: Formation of chunk graphite*, in Proceedings of the International Conference on Advanced Casting Technology, Kalamazoo, Michigan, USA, November 12-14, 1987. pp. 245-256. In: Baer, W., *Chunky graphite in ferritic spheroidal*

graphite cast iron: formation, prevention, characterization, impact on properties: an overview. International Journal of Metalcasting, 2019, 93(6), pp. 1-35.

89. Tonn, B., Lacaze, J. and Duwe, S., *Degenerated graphite growth in ductile iron*. Materials Science Forum, 2018, 925. pp. 62-69. In: Baer, W., *Chunky graphite in ferritic spheroidal graphite cast iron: formation, prevention, characterization, impact on properties: an overview*. International Journal of Metalcasting, 2019, 93(6), pp. 1-35.
90. Thielemann, T., *Zur Wirkung von Spurenelementen im Gusseisen mit Kugelgraphit*. Giessereitechnik, 1970, 16, pp. 16-24. In: Baer, W., *Chunky graphite in ferritic spheroidal graphite cast iron: formation, prevention, characterization, impact on properties: an overview*. International Journal of Metalcasting, 2019, 93(6), pp. 1-35.
91. Hoover Jr, H., *A literature survey on degenerate graphite in heavy section ductile iron*. AFS Transactions, 1986, 94, pp. 86-102. In: Baer, W., *Chunky graphite in ferritic spheroidal graphite cast iron: formation, prevention, characterization, impact on properties: an overview*. International Journal of Metalcasting, 2019, 93(6), pp. 1-35.
92. Hasse, S., *Die Wirkung von Spurenelementen in Gusseisen mit Kugelgraphit*. Gießerei-Praxis, 1995, 15(16), pp. 271-278. In: Baer, W., *Chunky graphite in ferritic spheroidal graphite cast iron: formation, prevention, characterization, impact on properties: an overview*. International Journal of Metalcasting, 2019, 93(6), pp. 1-35.
93. Diao, X.*, et al.*, *Effects of antimony addition and section size on formation of chunky graphite in ductile iron*. Materials Science Technology, 2011, 27(4). pp. 834-838. In: Baer, W., *Chunky graphite in ferritic spheroidal graphite cast iron: formation, prevention, characterization, impact on properties: an overview*. International Journal of Metalcasting, 2019, 93(6), pp. 1-35.
94. Plénard, E., *Cast iron, damping capacity, structure and property relations*. Modern Castings, 1962, 41, pp. 144-151. In: Angus, H.T., *Cast Iron: Physical and Engineering Properties*. 2nd ed. 1976, Butterworths.
95. Gharderi, A., Ahmadabadi, M.N. and Ghasemi, H., *Effect of graphite morphologies on the tribological behavior of austempered cast iron*. Wear, 2003, 255, pp. 410-416.
96. Berns, H. and Theisen, W. *Ferrous materials: steel and cast iron*. 2008, Springer Science & Business Media.
97. *ASM Handbook Volume 2: Properties and Selection: Nonferrous Alloys and Special-Purpose Materials,* ASM Intl.: Cleveland, OH, USA, 1990.
98. Fox, M. and Adams, R., *Correlation of the damping capacity of cast iron with its mechanical properties and microstructure*. Journal of Mechanical Engineering Science, 1973, 15(2), pp. 81-94.
99. Gale, W.F. and Totemeier, T.C., *Smithells Metals Reference Book*. 2003, Butterworth-Heinemann.
100. Granato, A. and Lucke, K., *Theory of mechanical damping due to dislocations*. Journal of Applied Physics, 1956, 27, pp. 583-593. In: Song, J.-M.*, et al.*, *Effects of matrix structure on the resonant vibration*

behavior of spheroidal graphite cast iron. Materials Transactions, 2004, 45(4), pp. 1379-1382.
101. Ruff, G.F. and Doshi, B.K., *Relation between mechanical properties and graphite structure in cast irons II - Ductile iron*. Modern Castings, 1980, 70. pp. 50-55. In: Song, J.-M.*, et al.*, *Effects of matrix structure on the resonant vibration behavior of spheroidal graphite cast iron*. Materials Transactions, 2004, 45(4), pp. 1379-1382.
102. Minkoff, I., *The Physical Metallurgy of Cast Iron*. New York, John Wiley & Sons, 1983. In: Song, J.-M.*, et al.*, *Effects of matrix structure on the resonant vibration behavior of spheroidal graphite cast iron*. Materials Transactions, 2004, 45(4), pp. 1379-1382.
103. O'Rourke, R., *Cast iron: A solid choice for reducing gear noise*. Gear Technology, 1999, 16, pp.46-49.
104. Petrushin, G., Petrushina, A. and Golovin, S., *Inelastic properties of high-strength cast iron with strained graphite*. Metal Science and Heat Treatment, 2011, 53(1-2), pp. 75-81.
105. Golovin, S., *On the damping capacity of cast irons*. The Physics of Metals and Metallography, 2012, 113(7), pp. 716-720.
106. Obaid, A.Y., Mahmood, I.A. and Abood, A.N., *Effects of friction stir processing on microstructural, hardness and damping characteristics of ferritic nodular cast iron*. Journal of Engineering Science and Technology, 2017, 12(1), pp. 229-240.
107. Song, J.-M.*, et al.*, *Effects of matrix structure on the resonant vibration behavior of spheroidal graphite cast iron*. Materials Transactions, 2004, 45(4), pp. 1379-1382.
108. Schaller, R. and Benoit, W., *Développement d'alliages biphasés à fort amortissement, un exemple: les fontes grises*. Material und Technik, 1985, 13. In: Millet, P., Schaller, R. and Benoit, W., *High damping in grey cast iron*. Le Journal de Physique Colloques, 1985, 46(C10),pp. 405-408.
109. Guesser, W. and Martins, L., *Stiffness and vibration damping capacity of high strength cast irons*. 25th SAE Brazil International Congress and Display, São Paulo, Brazil, October 25-27, 2016.
110. Murakami, T.*, et al.*, *Damping and tribological properties of Fe-Si-C cast iron prepared using various heat treatments*. Materials Science and Engineering: A, 2006, 432, pp. 113-119.
111. Lin, S., Lui, T. and Chen, L., *Effect of microstructure on resonant vibration fatigue fracture of ferritic spheroidal graphite cast iron*. International Journal of Cast Metals Research, 2000, 13. pp. 77-83. In: Lin, S.C., Lui, T.S., Chen, L.H. and Song, J.M., *Effect of pearlite on the vibration-fracture behavior of spheroidal graphite cast irons under resonant conditions*. Metallurgical and Materials Transactions A, 2002, 33(8), pp. 2623-2634.
112. Lin, S., Lui, T. and Chen, L., *Effect of nodularity on resonant vibration fracture behavior in upper bainitic and ferritic cast irons*. Metallurgical and Materials Transactions A, 2000, 31(9), pp. 2193-2203. In: Lin, S.C., Lui, T.S., Chen, L.H. and Song, J.M., *Effect of pearlite on the vibration-fracture behavior of spheroidal graphite cast irons under resonant conditions*. Metallurgical and Materials Transactions A, 2002, 33(8),

pp. 2623-2634.
113. Damir, A., Elkhatib, A. and Nassef, G., *Prediction of fatigue life using modal analysis for grey and ductile cast iron*. International Journal of Fatigue, 2007, 29, pp. 499-507.
114. Carpenter, S., Stuch, T. and Salzbrenner, R., *An investigation of the mechanical damping of ductile iron*. Metallurgical and Materials Transactions A, 1995, 26(11), pp. 2785-2790.
115. Cho, M.*, et al.*, *Tribological study of gray cast iron with automotive brake linings: The effect of rotor microstructure*. Tribology International, 2003, 36(7), pp. 537-545.
116. Dryden, J. and Purdy, G., *The effect of graphite on the mechanical properties of cast irons*. Acta Metallurgica, 1989, 37(7), pp. 1999-2006. In: Liu, X., *et al.*, *Damping characteristics of cast irons with aluminum addition*. Journal of Materials Science, 2005, 40. pp. 5565-5567.
117. Liu, X.*, et al.*, *Low-temperature damping behavior of cast iron with aluminum addition*. Journal of Materials Science, 2005, 40(7), pp. 1773-1775.
118. Takamori, S., Osawa, Y. and Halada, K., *Aluminum-alloyed cast iron as a versatile alloy*. Materials Transactions, 2002, 43(3), pp. 311-314.
119. Millet, P., Schaller, R. and Benoit, W., *High damping in grey cast iron*. Le Journal de Physique Colloques, 1985, 46(C10), pp. 405-408.
120. Fujimoto, R. and Hareyama, T., Patent Title: High-strength, high-damping-capacity cast iron. 2014, Toshiba Kikai Kabushiki Kaisha.
121. LAS – Leica Application Suite, *Automatic software manual*. Accessed on May 2021.
122. ISO-945, Microstructure of cast irons - Part 2: Graphite classification by image analysis. 2016.
123. ISO-945, Microstructure of cast irons - Part 3: Matrix structures. 2016.
124. Simões, S.L.S., *Ligação por difusão no estado sólido de aluminetos de titânio revestidos com filmes finos multicamada*. PhD thesis, Faculdade de Engenharia da Universidade do Porto, 2012.
125. Brundle, C.R., Evans, C.A.J. and Wilson, S., *Encyclopedia of Materials Characterization: Surfaces, Interfaces, Thin Films*. 1992, Gulf Professional Publishing.
126. ASM Handbook Volume 3: Alloy Phase Diagrams. ASM Intl.: Cleveland, OH, USA, 1990.
127. ASM Handbook Volume 8: Mechanical Testing and Evaluation. ASM Intl.: Cleveland, OH, USA, 1990.
128. Sinha, A.K. Physical Metallurgy Handbook. 2003, McGraw-Hill Professional Publishing.

Annexe A: Determination of the casting modulus

A study aiming to determine the casting modulus was performed to establish a single casting modulus for each section thickness of the step-casting. The *QuikCAST* software was used to simulate the solidification of the step-casting to understand if this desideratum would be possible.

Some of the selected simulation parameters are presented in Table A. 1. On the other hand, Figure A. 1 shows the results from the solidification simulation of the step-casting with those parameters.

Table A. 1. Parameters used for the simulation of the solidification of the step-casting by the QuikCAST software

Simulation parameters	
Cast iron grade	GJS 500-7
Pouring temperature	1500ºC
Mesh size	< 5 mm
Sand	Self-setting, 25ºC Permeability and rugosity from the software database

The casting modulus is related to the solidification rate of the geometric centre of each casting section.

Firstly, it was decided to establish a mean value for each section thickness based on the casting modulus range for the geometric centre of each section. However, as the results from the solidification pointed out, the casting modulus is not entirely homogeneous for each section thickness. So, it would not be perfectly correct to assume a single modulus for each step of the casting, regardless of considering its geometric centre.

Therefore, all the results are presented regarding the section thicknesses. As expected, the results shown in Figure A. 1 confirm that the casting modulus increases with the section thickness.

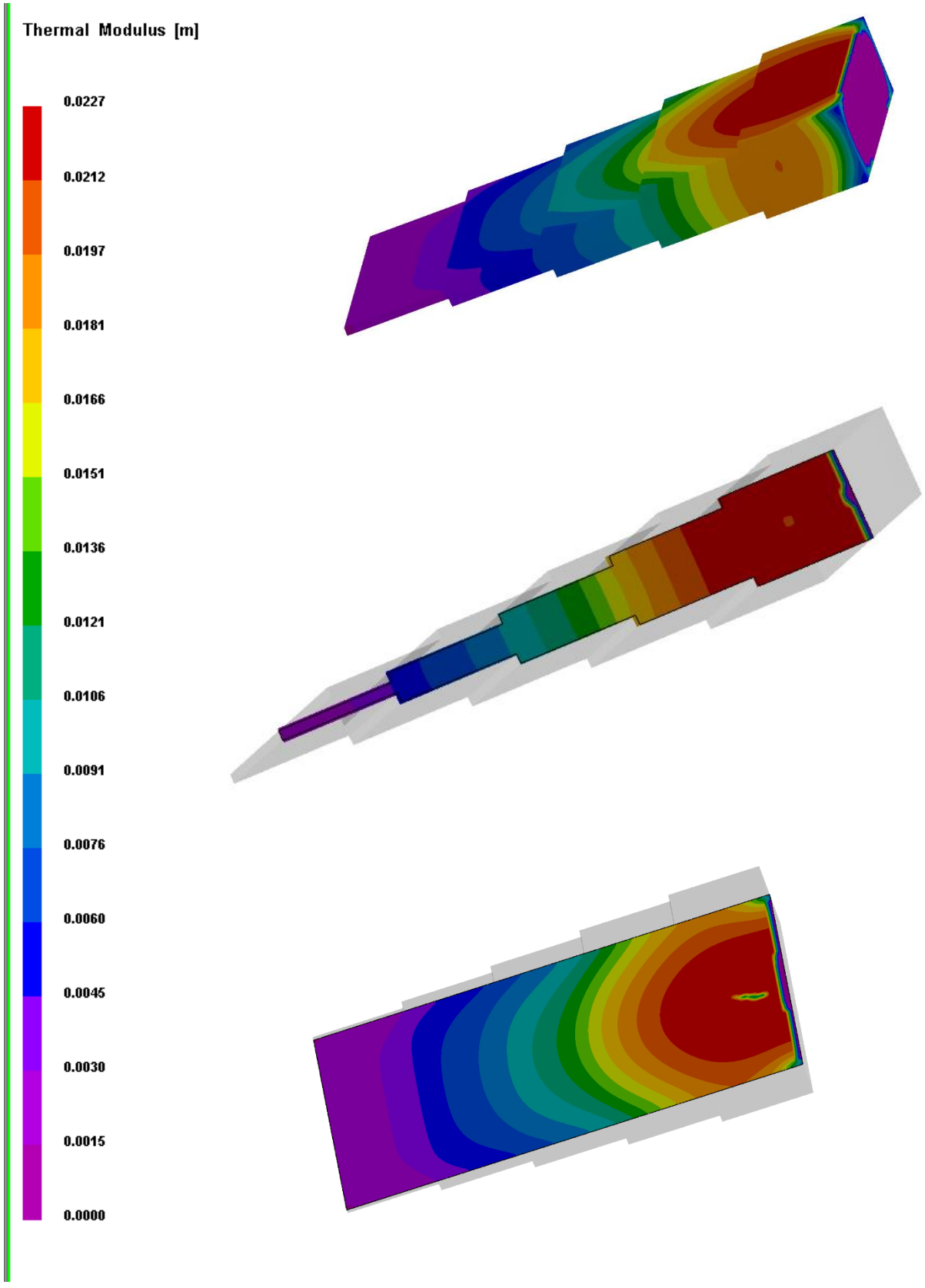


Figure A. 1. Images of the simulation of the solidification of the step-casting by the QuikCAST software.

Annexe B: Complementary results

B.1. First Approach Experiments

B.1.1. High Si-alloyed SGI

Table B. 1. Fundamental flexural frequency and elastic properties of the High Si-alloyed SGI, for different section thicknesses

Section thickness (mm)	5	15	25	35	45	Trend line equation and R^2 for the material property (y) *vs.* the section thickness (x)
Fundamental flexural frequency (Hz)	4239	4262	4259	4252	4226	$R^2 < 0.5$*
Relative variation (%)	-0.3	0.9	0.6	0.7	0.0	
CV estimated (%)	*± 0.004*					
Shear modulus (GPa)	68	68	69	68	67	$R^2 < 0.5$*
Relative variation (%)	-2.9	-2.9	0.0	-1.5	-2.9	
CV estimated (%)	*± 0.4*	*± 0.4*	*± 0.4*	*± 0.5*	*± 0.4*	
Poisson's ratio	0.275	0.273	0.274	0.266	0.276	$R^2 < 0.5$*
Relative variation (%)	2.2	-1.1	0.9	-1.6	2.2	
CV estimated (%)	*± 0.06*					

** As $R^2 < 0.5$, the trend line equation is not presented*

B.1.2. Co-alloyed SGI

Table B. 2. Fundamental flexural frequency and elastic properties of the Co (x1)-alloyed SGI, for different section thicknesses

Section thickness (mm)	5	15	25	35	45	Trend line equation and R^2 for the material property (y) *vs.* the section thickness (x)
Fundamental flexural frequency (Hz)	4264	4247	4235	4260	4228	$R^2 < 0.5$*
Relative variation (%)	0.3	0.5	0.0	0.9	0.1	
CV estimated (%)	*± 0.004*					
Shear modulus (GPa)	70	69	67	69	70	$R^2 < 0.5$*
Relative variation (%)	0.0	-1.4	-2.9	0.0	1.5	
CV estimated (%)	*± 0.5*	*± 0.4*	*± 0.4*	*± 0.4*	*± 1.1*	
Poisson's ratio	0.271	0.266	0.269	0.265	0.271	$R^2 < 0.5$*
Relative variation (%)	0.7	-3.6	-1.1	-1.9	0.4	
CV estimated (%)	*± 0.06*					

** As $R^2 < 0.5$, the trend line equation is not presented*

Table B. 3. Fundamental flexural frequency and elastic properties of the Co (x2)-alloyed SGI, for different section thicknesses

Section thickness (mm)	5	15	25	35	45	Trend line equation and R^2 for the material property (y) *vs.* the section thickness (x)
Fundamental flexural frequency (Hz)	4261	4265	4277	4263	4283	$R^2 < 0.5$*
Relative variation (%)	0.3	0.9	0.9	0.9	1.4	
CV estimated (%)	*± 0.004*					
Shear modulus (GPa)	70	69	68	69	69	$R^2 < 0.5$*
Relative variation (%)	0.0	-1.4	-1.5	0.0	0.0	
CV estimated (%)	*± 0.8*	*± 0.8*	*± 0.4*	*± 0.4*	*± 0.4*	
Poisson's ratio	0.273	0.273	0.273	0.265	0.269	$R^2 < 0.5$*
Relative variation (%)	1.4	-0.9	-0.4	-2.1	-0.4	
CV estimated (%)	*± 0.06*					

** As $R^2 < 0.5$, the trend line equation is not presented*

B.1.3. RE-alloyed SGI

Table B. 4. Fundamental flexural frequency and elastic properties of the RE (x1)-alloyed SGI, for different section thicknesses

	Section thickness (mm)	5	15	25	35	45	Trend line equation and R^2 for the material property (y) *vs.* the section thickness (x)
RE (x1)-alloyed SGI	**Fundamental flexural frequency (Hz)**	4214	4218	4222	4227	4222	y = 5.0893 ln(x) + + 4205.2 R^2 = 0.7897
	Relative variation (%)	-0.9	-0.2	-0.3	0.1	-0.1	
	CV estimated (%)	*± 0.004*					
	Shear modulus (GPa)	69	68	69	69	69	R^2 < 0.5*
	Relative variation (%)	-1.4	-2.9	0.0	0.0	0.0	
	CV estimated (%)	*± 0.5*	*± 0.8*	*± 0.4*	*± 0.4*	*± 0.8*	
	Poisson's ratio	0.270	0.272	0.274	0.271	0.273	R^2 < 0.5*
	Relative variation (%)	0.4	-1.3	0.9	0.1	0.9	
	CV estimated (%)	*± 0.06*					

** As R^2 < 0.5, the trend line equation is not presented*

B.1.4. High Si + RE-alloyed SGI combinations

Table B. 5. Fundamental flexural frequency and elastic properties of the High Si + RE (x0.5)-alloyed SGI, for different section thicknesses

Section thickness (mm)	5	15	25	35	45	Trend line equation and R^2 for the material property (y) *vs.* the section thickness (x)
Fundamental flexural frequency (Hz)	4223	4199	4240	4206	4204	$R^2 < 0.5$*
Relative variation (%)	-0.6	-0.6	0.1	-0.4	-0.5	
CV estimated (%)	*± 0.004*					
Shear modulus (GPa)	67	68	68	68	67	$R^2 < 0.5$*
Relative variation (%)	-4.3	-2.9	-1.5	-1.5	-2.9	
CV estimated (%)	*± 0.5*	*± 1.0*	*± 0.4*	*±0.6*	*± 0.5*	
Poisson's ratio	0.274	0.268	0.270	0.263	0.274	$R^2 < 0.5$*
Relative variation (%)	1.9	-2.9	-0.7	-2.7	1.5	
CV estimated (%)	*± 0.06*					

** As $R^2 < 0.5$, the trend line equation is not presented*

Table B. 6. Fundamental flexural frequency and elastic properties of the High Si + RE (x1)-alloyed SGI, for different section thicknesses

Section thickness (mm)	5	15	25	35	45	Trend line equation and R^2 for the material property (y) *vs.* the section thickness (x)
Fundamental flexural frequency (Hz)	4223	4222	4223	4199	4223	$R^2 < 0.5$*
Relative variation (%)	-0.7	-0.1	-0.3	-0.6	-0.1	
CV estimated (%)	*± 0.004*					
Shear modulus (GPa)	68	67	68	68	67	$R^2 < 0.5$*
Relative variation (%)	-2.9	-4.3	-1.5	-1.5	-2.9	
CV estimated (%)	*± 0.5*	*± 1.1*	*± 0.5*	*± 0.9*	*± 0.8*	
Poisson's ratio	0.277	0.270	0.270	0.263	0.274	$R^2 < 0.5$*
Relative variation (%)	2.9	-2.2	-0.7	-2.9	1.5	
CV estimated (%)	*± 0.06*					

** As $R^2 < 0.5$, the trend line equation is not presented*

B.1.5. Cu-alloyed SGI

Table B. 7. Results of tests performed on the Cu-alloyed SGI samples from the first approach experiments

Section thickness (mm)	5	15	25	35	45	Trend line equation and R^2 for the material property (y) *vs.* the section thickness (x)
Damping capacity	0.000237	0.000295	0.000302	0.000331	0.000312	$y = 4x10^{-5} \ln(x) + 0.0002$ $R^2 = 0.8894$
Relative variation (%)	– 10	– 13	– 20	– 16	– 26	
CV estimated (%)	*± 1*					
Fundamental flexural frequency (Hz)	4245	4241	4244	4241	4148	$y = -1.9448x + 4272.5$ $R^2 = 0.5262$
Relative variation (%)	– 0.1	0.3	0.2	0.4	– 1.8	
CV estimated (%)	*± 0.004*					
Young's modulus (GPa)	176	176	175	173	162	$y = -0.3096x + 180.15$ $R^2 = 0.6784$
Relative variation (%)	– 1.1	– 1.1	– 1.1	– 1.1	– 7.4	
CV estimated (%)	*± 1.4*	*± 1.1*	*± 1.1*	*± 2.1*	*± 2.3*	
Shear modulus (GPa)	69	69	69	68	64	$y = -0.11x + 70.55$ $R^2 = 0.6436$
Relative variation (%)	– 1.4	– 1.4	0	– 1.5	– 7.3	
CV estimated (%)	*± 0.6*	*± 0.4*	*± 0.4*	*± 0.8*	*± 0.8*	
Poisson's ratio	0.270	0.273	0.272	0.273	0.269	$R^2 < 0.5$*
Relative variation (%)	0.5	– 1.1	0	0.9	– 0.3	
CV estimated (%)	*± 0.06*					
Ultimate tensile strength (MPa)	473	565	576	570	548	$y = 38.907 \ln(x) + 430.37$ $R^2 = 0.6401$
Relative variation (%)	– 11	31	43	47	42	
CV estimated (%)	*± 7*					
0.2% offset yield strength (MPa)	379	356	357	351	342	$y = -15.16 \ln(x) + 402.08$ $R^2 = 0.9318$
Relative variation (%)	14	24	30	36	32	
CV estimated (%)	*± 6*					
Elongation (%)	–	13.3	12.7	13.8	13.2	$R^2 < 0.5$*
Relative variation (%)	–	– 27	– 33	– 32	– 34	
CV estimated (%)	*± 6*					
Hardness (HBW 2.5/187.5)	183	185	185	186	185	$y = 1.149 \ln(x) + 181.63$ $R^2 = 0.7789$
Relative variation (%)	15	34	25	42	42	
CV estimated (%)	*± 5*					
Pearlite (%)	45	45	45	45	40	–
Graphite (%)	7.9	10.8	9.5	11.4	11.1	–
Nodularity (%)	92	94	90	88	92	–
Nodule count (particles/mm²)	586	551	358	310	378	–
Convex perimeter (µm)	40	46	54	61	56	–
Graphite form-III (%)	0.6	0.8	1.6	4.2	1.1	–

** As $R^2 < 0.5$, the trend line equation is not presented*

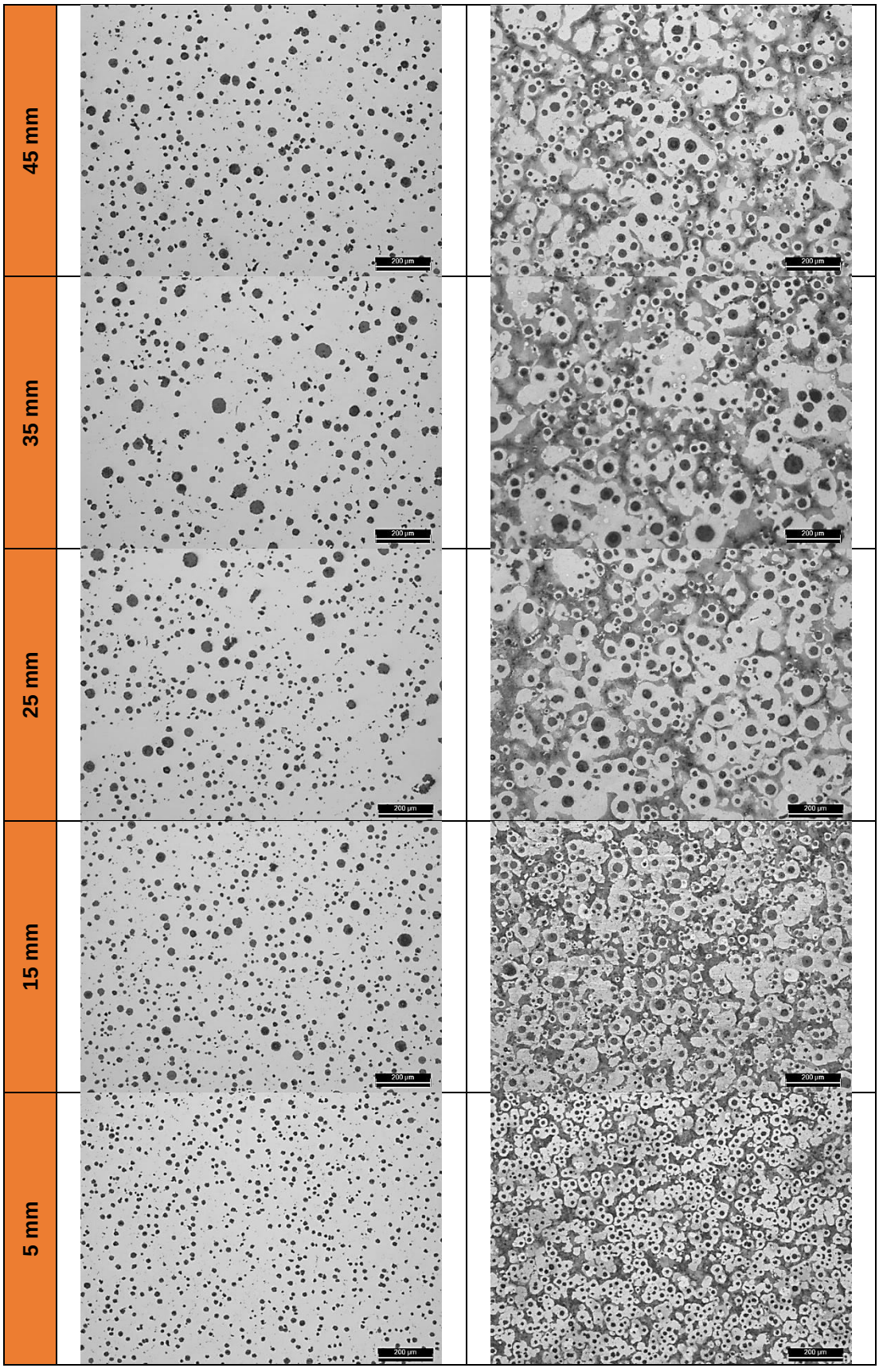


Figure B. 1. LOM micrographs of the Cu-alloyed SGI, for different section thicknesses.

B.1.6. Mo-alloyed SGI

Table B. 8. Results of tests performed on Mo(x1)-alloyed SGI samples from the first approach experiments

Section thickness (mm)	5	15	25	35	45	Trend line equation and R^2 for the material property (y) *vs.* the section thickness (x)
Damping capacity	0.000249	0.000313	0.000357	0.000351	0.000364	$y = 5x10^{-5} \ln(x) + 0.0002$ $R^2 = 0.9536$
Relative variation (%)	– 5	– 9	– 17	– 8	– 13	
CV estimated (%)	*± 1*					
Fundamental flexural frequency (Hz)	4280	4255	4217	4267	4260	$R^2 < 0.5$*
Relative variation (%)	0.7	0.7	– 0.4	1.0	0.8	
CV estimated (%)	*± 0.004*					
Young's modulus (GPa)	178	173	169	174	173	$R^2 < 0.5$*
Relative variation (%)	0	– 2.8	– 4.5	– 0.6	– 1.1	
CV estimated (%)	*± 1.1*	*± 1.2*	*± 1.2*	*± 1.2*	*± 1.2*	
Shear modulus (GPa)	70	68	67	68	68	$y = -0.985 \ln(x) + 71.136$ $R^2 = 0.6117$
Relative variation (%)	0.0	– 2.9	– 2.9	– 1.5	– 1.5	
CV estimated (%)	*± 0.4*	*± 0.5*	*± 0.4*	*± 0.5*	*± 0.5*	
Poisson's ratio	0.266	0.268	0.269	0.274	0.271	$y = 0.0028 \ln(x) + 0.2611$ $R^2 = 0.7233$
Relative variation (%)	– 1.1	– 2.9	– 0.9	1.1	0.3	
CV estimated (%)	*± 0.06*					
Ultimate tensile strength (MPa)	–	444	431	424	430	$y = -14.85 \ln(x) + 481.44$ $R^2 = 0.6965$
Relative variation (%)	–	3	7	9	11	
CV estimated (%)	*± 7*					
0.2% offset yield strength (MPa)	–	314	311	300	299	$y = -0.54x + 321.95$ $R^2 = 0.9042$
Relative variation (%)	–	9	13	16	15	
CV estimated (%)	*± 6*					
Elongation (%)	–	21.8	16.2	15.1	17.8	$R^2 < 0.5$*
Relative variation (%)	–	19	– 14	– 26	– 11	
CV estimated (%)	*± 6*					
Hardness (HBW 2.5/*) *62.5: ≤ 140 HBW or 187.5: > 140 HBW	163	156	153	138	136	$y = -0.7343x + 167.47$ $R^2 = 0.949$
Relative variation (%)	3	13	3	5	3	
CV estimated (%)	*± 5*					
Pearlite (%)	20					–
Graphite (%)	4.4	7.5	8.0	7.9	5.9	–
Nodularity (%)	70	61	56	53	42	–
Nodule count (particles/mm^2)	560	391	333	280	399	–
Convex perimeter (µm)	33	46	52	53	40	–
Graphite form-III (%)	10.1	15.2	24.2	23.9	31.6	–

** As $R^2 < 0.5$, the trend line equation is not presented*

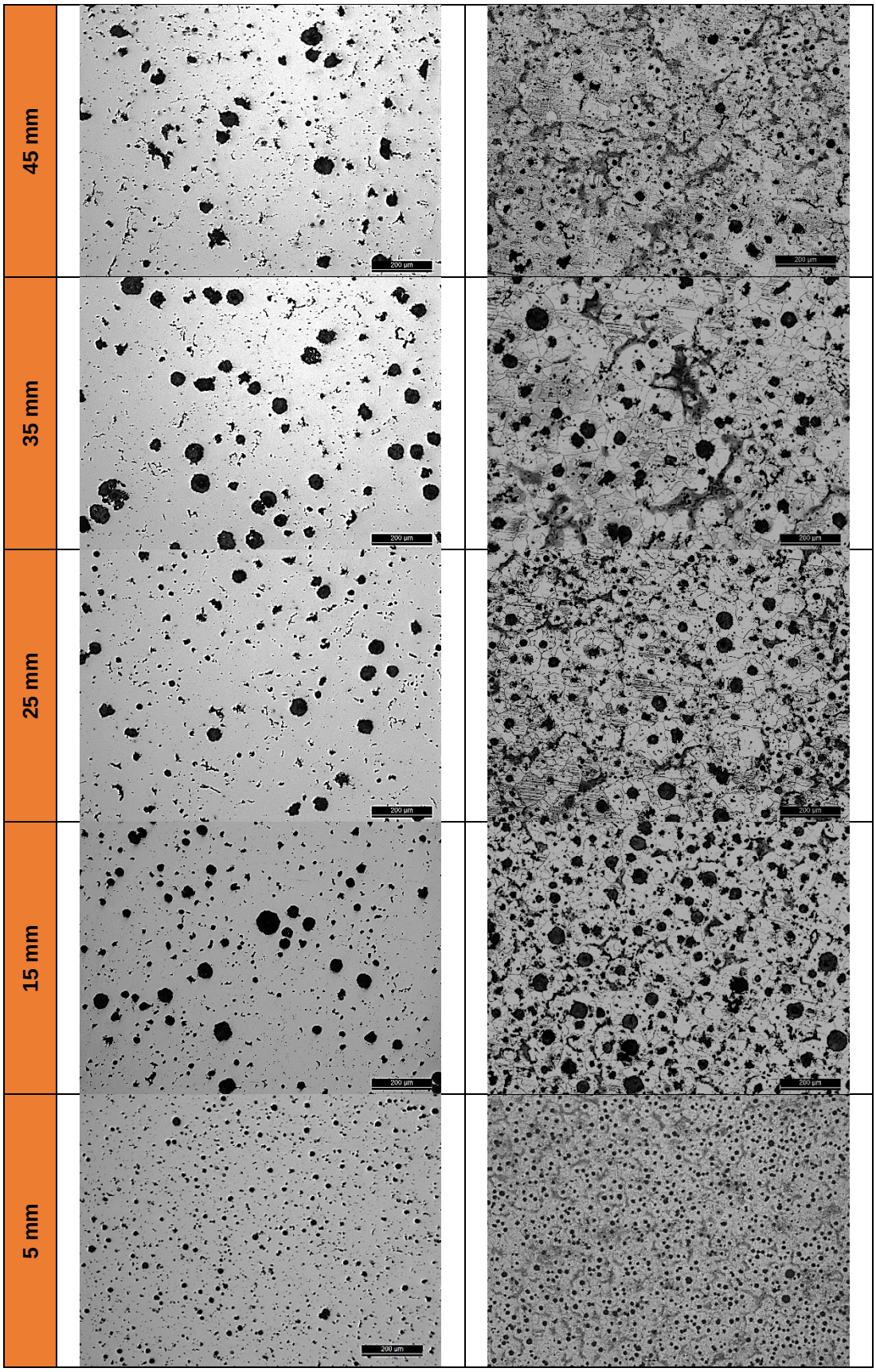


Figure B. 2. LOM micrographs of the Mo (x1)-alloyed SGI, for different section thicknesses.

Table B. 9. Results of tests performed on the Mo (x2)-alloyed SGI samples from the first approach experiments

Section thickness (mm)	5	15	25	35	45	Trend line equation and R^2 for the material property (y) *vs.* the section thickness (x)
Damping capacity	0.000251	0.000308	0.000313	0.000360	0.000366	$y = 5x10^{-5} \ln(x) + 0.0002$ $R^2 = 0.9406$
Relative variation (%)	– 5	– 9	– 17	– 8	– 13	
CV estimated (%)	*± 1*					
Fundamental flexural frequency (Hz)	4260	4267	4267	4255	4255	$R^2 < 0.5$*
Relative variation (%)	0.2	0.9	0.8	0.8	0.7	
CV estimated (%)	*± 0.004*					
Young's modulus (GPa)	175	175	176	174	174	$R^2 < 0.5$*
Relative variation (%)	– 1.7	– 1.7	– 0.6	– 0.6	– 0.6	
CV estimated (%)	*± 1.1*	*± 1.2*	*± 1.1*	*± 1.1*	*± 1.1*	
Shear modulus (GPa)	69	69	69	68	69	$R^2 < 0.5$*
Relative variation (%)	– 1.4	– 1.4	0.0	– 1.5	0.0	
CV estimated (%)	*± 0.4*					
Poisson's ratio	0.269	0.268	0.275	0.271	0.264	$R^2 < 0.5$*
Relative variation (%)	0.1	– 2.8	0.9	0.1	– 2.1	
CV estimated (%)	*± 0.06*					
Ultimate tensile strength (MPa)	527	473	452	448	454	$y = -36.13 \ln(x) + 578.34$ $R^2 = 0.9098$
Relative variation (%)	0	10	12	15	17	
CV estimated (%)	*± 7*					
0.2% offset yield strength (MPa)	441	333	323	317	316	$y = -57.47 \ln(x) + 517.13$ $R^2 = 0.8693$
Relative variation (%)	32	16	18	23	22	
CV estimated (%)	*± 6*					
Elongation (%)	–	17.2	12.2	10.9	16.8	$R^2 < 0.5$*
Relative variation (%)	–	– 6	– 35	– 47	– 16	
CV estimated (%)	*± 6*					
Hardness (HBW 2.5/187.5)	175	166	163	159	159	$y = -7.53 \ln(x) + 186.7$ $R^2 = 0.994$
Relative variation (%)	10	20	10	21	21	
CV estimated (%)	*± 5*					
Pearlite (%)	30					–
Graphite (%)	3.5	5.3	8.5	9.7	8.3	–
Nodularity (%)	64	69	55	42	61	–
Nodule count (particles/mm²)	465	320	444	286	285	–
Convex perimeter (µm)	32	42	45	62	53	–
Graphite form-III (%)	12.1	13.2	21.4	32.0	18.3	–

** As $R^2 < 0.5$, the trend line equation is not presented*

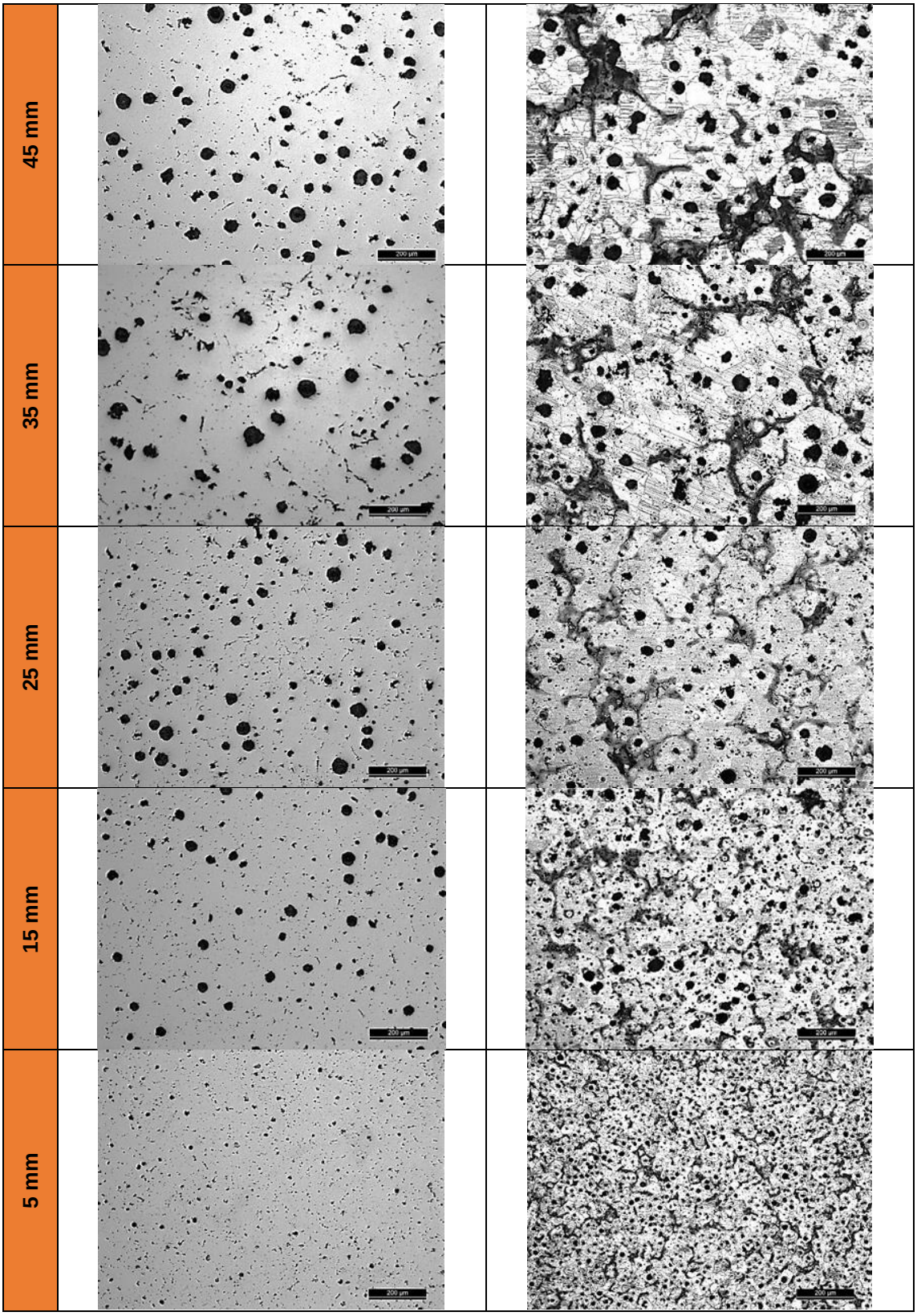


Figure B. 3. LOM micrographs of the Mo (x2)-alloyed SGI, for different section thicknesses.

B.1.7. Al (x1)-alloyed SGI

Table B. 10. Results of tests performed on the Al (x1)-alloyed SGI sample from the first approach experiments

Section thickness (mm)	45
Damping capacity	0.000292
Relative variation (%)	– 31
CV estimated (%)	± *1*
Fundamental flexural frequency (Hz)	4215
Relative variation (%)	– 0.24
CV estimated (%)	± *0.004*
Young's modulus (GPa)	168
Relative variation (%)	– 3.8
CV estimated (%)	± *1.2*
Shear modulus (GPa)	66
Relative variation (%)	– 3.9
CV estimated (%)	± *0.5*
Poisson's ratio	0.270
Relative variation (%)	0
CV estimated (%)	± *0.06*
Ultimate tensile strength (MPa)	528
Relative variation (%)	36
CV estimated (%)	± *7*
0.2% offset yield strength (MPa)	481
Relative variation (%)	85
CV estimated (%)	± *6*
Elongation (%)	2.8
Relative variation (%)	– 86
CV estimated (%)	± *6*
Hardness (HBW 2.5/187.5)	195
Relative variation (%)	49
CV estimated (%)	± *5*

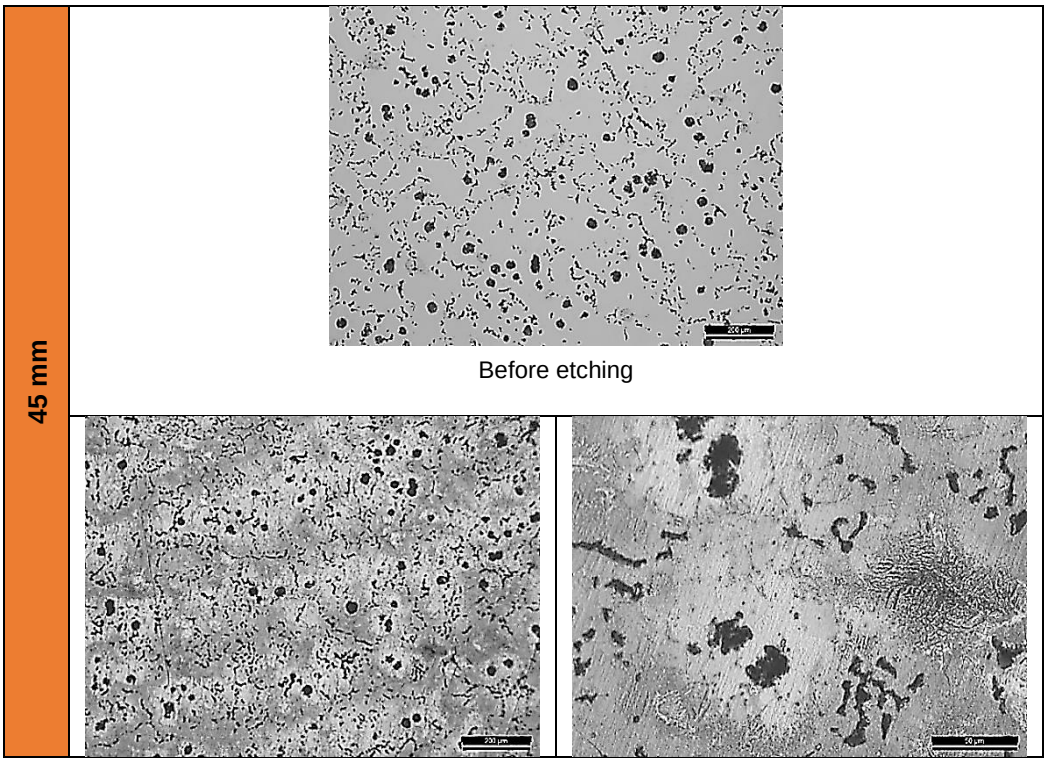


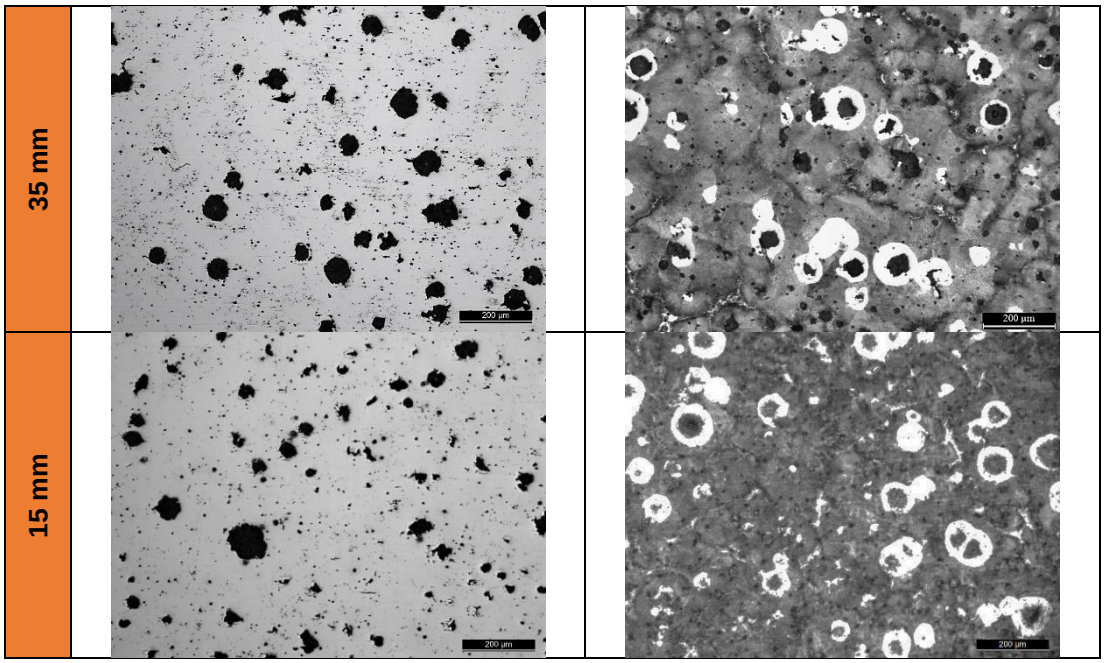
Figure B. 4. LOM micrographs of the Al (x1)-alloyed SGI, for the 45 mm section thickness.

B.2. Fine Approach Experiments

B.2.1. Base 1 SGI

Table B. 11. Results of the tests performed on the Base 1 SGI samples from the fine approach experiments

Section thickness (mm)	15	35
Damping capacity	0.000234	0.000250
CV estimated (%)	*± 1*	
Fundamental flexural frequency (Hz)	4197	4227
CV estimated (%)	*± 0.004*	
Young's modulus (GPa)	174	178
CV estimated (%)	*± 2.3*	*± 1.1*
Shear modulus (GPa)	69	71
CV estimated (%)	*± 0.9*	*± 0.4*
Poisson's ratio	0.264	0.261
CV estimated (%)	*± 0.06*	
Ultimate tensile strength (MPa)	753	719
CV estimated (%)	*± 7*	
0.2% offset yield strength (MPa)	430	410
CV estimated (%)	*± 6*	
Elongation (%)	7.2	6.8
CV estimated (%)	*± 6*	
Hardness (HBW 2.5/187.5)	237	226
CV estimated (%)	*± 5*	
Pearlite (%)	75	75
Graphite (%)	8.0	8.3
Nodularity (%)	39	57
Nodule count (particles/mm^2)	320	187
Convex perimeter (µm)	47	60
Graphite form-III (%)	35.2	17.5



Before etching After etching

Figure B. 5. LOM micrographs of the Base 1 SGI, for the 35 and 15 mm section thicknesses.

B.2.2. High Si-alloyed SGI combinations

Table B. 12. Fundamental flexural frequency and elastic properties of the High Si-alloyed SGI combinations from the fine approach experiments

	Alloyed SGI	High Si	High Si + Ce (x0.5)	High Si + Ce (x0.5) + Co
35 mm section thickness	**Fundamental flexural frequency (Hz)**	4233	4146	4240
	Relative variation (%)	0	– 2	0
	CV estimated (%)	*± 0.004*	*± 0.004*	*± 0.004*
	Shear modulus (GPa)	67	67	68
	Relative variation (%)	– 1	– 1	0
	CV estimated (%)	*± 0.6*	*± 0.9*	*± 0.8*
	Poisson's ratio	0.269	0.252	0.279
	Relative variation (%)	– 1	– 8	2
	CV estimated (%)	*± 0.06*		

B.2.3. Co + Ce-alloyed SGI

Table B. 13. Results of the tests performed on the Co + Ce (x0.5)-alloyed SGI samples from the fine approach experiments

Section thickness (mm)	15	35
Damping capacity	0.000272	0.000297
Relative variation (%)	17	19
CV estimated (%)	*± 1*	
Fundamental flexural frequency (Hz)	4251	4209
Relative variation (%)	1	0
CV estimated (%)	*± 0.004*	
Young's modulus (GPa)	175	176
Relative variation (%)	– 1	1
CV estimated (%)	*± 1.2*	*± 1.3*
Shear modulus (GPa)	70	70
Relative variation (%)	1	– 1
CV estimated (%)	*± 0.5*	*± 0.6*
Poisson's ratio	0.254	0.249
Relative variation (%)	– 4	– 4
CV estimated (%)	*± 0.06*	
Ultimate tensile strength (MPa)	679	655
Relative variation (%)	– 10	– 9
CV estimated (%)	*± 7*	
0.2% offset yield strength (MPa)	426	407
Relative variation (%)	– 1	– 1
CV estimated (%)	*± 6*	
Elongation (%)	10	7
Relative variation (%)	38	6
CV estimated (%)	*± 6*	
Hardness (HBW 2.5/187.5)	232	214
Relative variation (%)	– 2	– 5
CV estimated (%)	*± 5*	
Pearlite (%)	65	65
Graphite (%)	7.4	10.9
Nodularity (%)	51	50
Nodule count (particles/mm^2)	354	530
Convex perimeter (µm)	46	42
Graphite form-III (%)	26.9	23.1

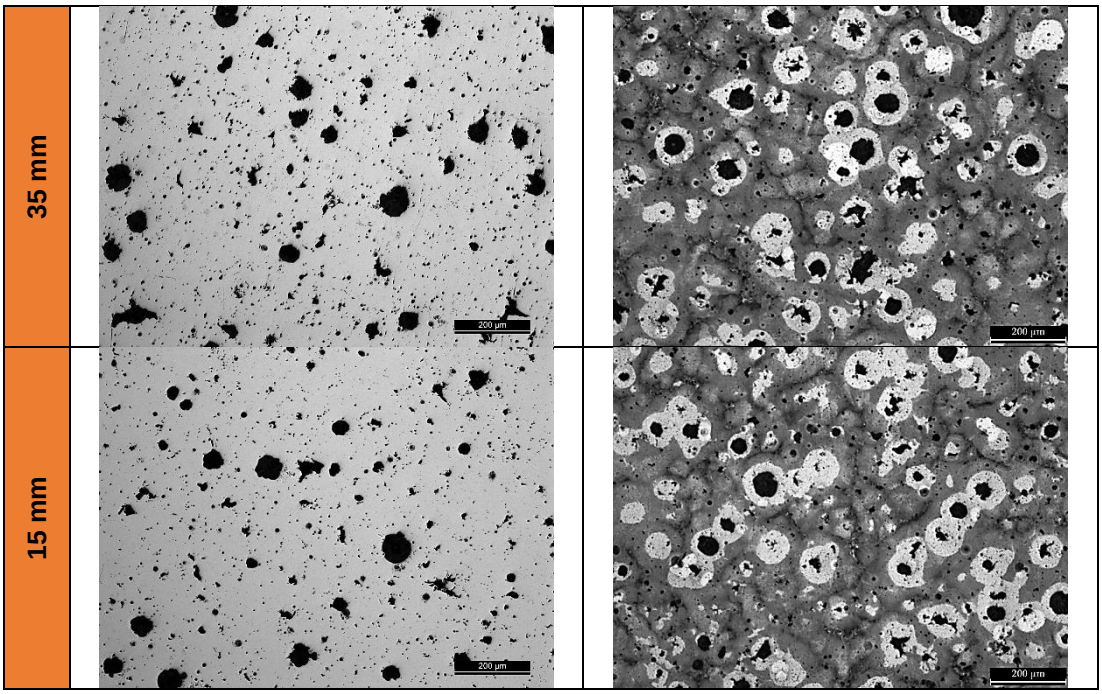
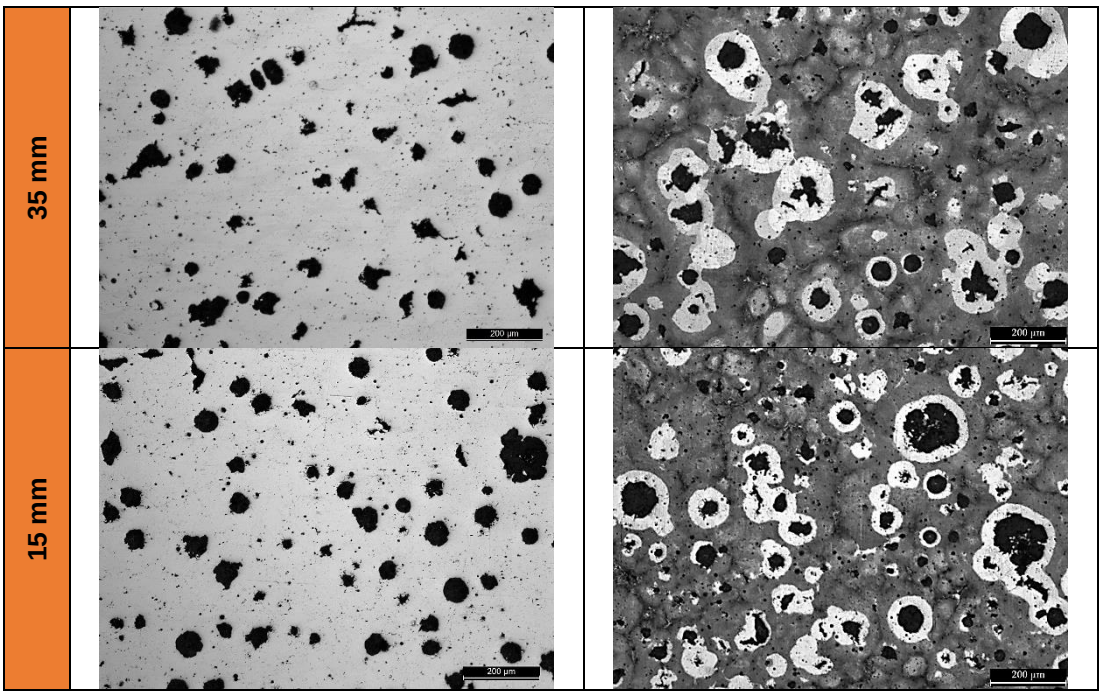


Figure B. 6. LOM micrographs of the Co + Ce (x0.5)-alloyed SGI, for the 35 and 15 mm section thicknesses.

Table B. 14. Results of the tests performed on the Co + Ce (x1)-alloyed SGI samples from the fine approach experiments

Section thickness (mm)	**15**	**35**
Damping capacity	0.000239	0.000254
Relative variation (%)	21	27
CV estimated (%)	*± 1*	
Fundamental flexural frequency (Hz)	4254	4245
Relative variation (%)	1	0
CV estimated (%)	*± 0.004*	
Young's modulus (GPa)	178	178
Relative variation (%)	2	0
CV estimated (%)	*± 1.1*	*± 1.4*
Shear modulus (GPa)	70	70
Relative variation (%)	1	– 1
CV estimated (%)	*± 0.4*	*± 0.7*
Poisson's ratio	0.271	0.267
Relative variation (%)	3	2
CV estimated (%)	*± 0.06*	
Ultimate tensile strength (MPa)	707	673
Relative variation (%)	– 6	– 6
CV estimated (%)	*± 7*	
0.2% offset yield strength (MPa)	442	424
Relative variation (%)	3	3
CV estimated (%)	*± 6*	
Elongation (%)	8.6	7.8
Relative variation (%)	20	14
CV estimated (%)	*± 6*	
Hardness (HBW 2.5/187.5)	233	224
Relative variation (%)	– 2	– 1
CV estimated (%)	*± 5*	
Pearlite (%)	60	55
Graphite (%)	8.6	9.2
Nodularity (%)	45	41
Nodule count (particles/mm^2)	164	252
Convex perimeter (µm)	70	54
Graphite form-III (%)	30.2	34.5



Before etching After etching

Figure B. 7. LOM micrographs of the Co + Ce (x1)-alloyed SGI, for the 15 and 35 mm section thicknesses.

B.2.4. Al (x5)-alloyed SGI

Table B. 15. Results of the tests performed on the Al (x5)-alloyed SGI sample from the fine approach experiments

Section thickness (mm)	15
Hardness (HBW 2.5/187.5)	407
Relative variation (%)	67
CV estimated (%)	± 5
Density	6.4
Relative variation (%)	~ 10

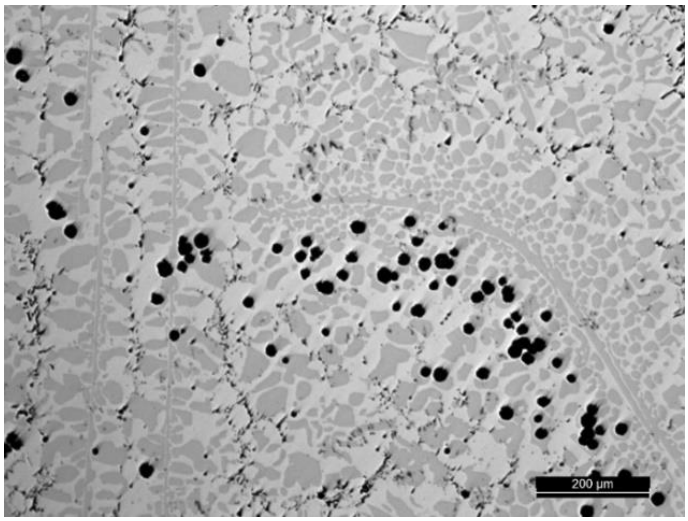
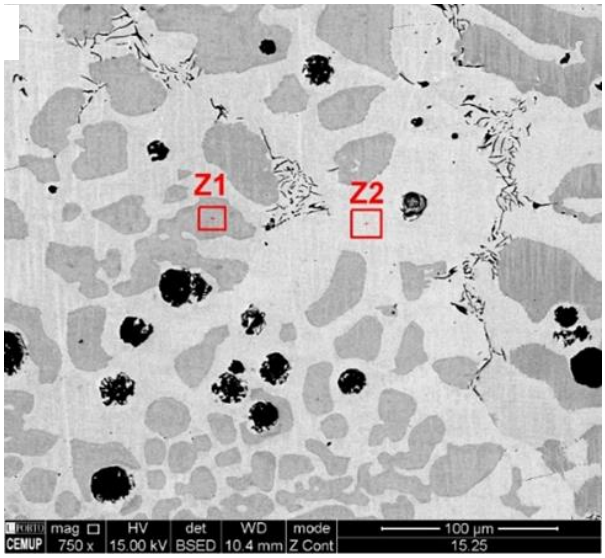
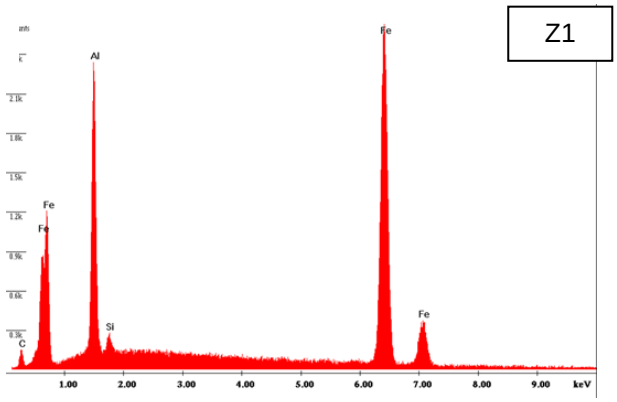


Figure B. 8. LOM micrographs of the Al (x5)-alloyed SGI, for the 15 mm section thickness.

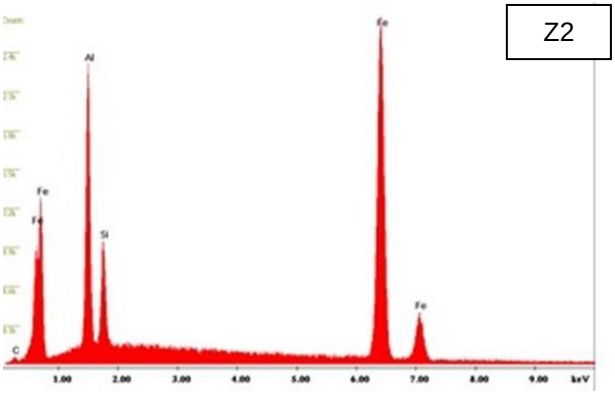
a)



b)



c)



d)

		wt. %	at. %
Z1	Al	12.54	20.92
	Si	0.76	1.22
Z2	Al	11.90	20.47
	Si	4.64	7.66

Figure B. 9. a) SEM micrograph of the Al (x5)-alloyed SGI, for the 15 mm section thickness; b) and c) X-ray spectra of Z1 and Z2 zones, respectively; d) EDS semi-quantitative analysis of Z1 and Z2 zones.

Annexe C: Model proposed for estimating the damping capacity

A model that considers only ferritic SGIs (pearlite ≤ 25%) was developed to verify the influence of nodularity in damping capacity instead of the fraction of the III-form graphite. The analysis resulted in a statistical model [$p < 0.001$; $R^2 = 0.730$], with a high correlation, indicating that damping is estimated in 73% by the set of predictor variables: % ferrite ($\beta = 0.636$; $p < 0.001$), convex perimeter ($\beta = 0.603$; $p < 0.001$) and nodularity ($\beta = -0.277$; $p = 0.002$). The analysis of the multiple linear regression of the results shows that the assumptions are fulfilled (Table C. 1), according to sub-chapter 3.1.4.7.

Table C. 1. Analysis of the multiple linear regression assumptions

Assumption	Results	
1	44 cases per independent variable	Fulfilled
2	Ferrite: Tolerance = 0.982 and VIF = 1.018 *Convex* Perimeter: Tolerance = 0.980 and VIF = 1.020 Nodularity: Tolerance = 0.998 and VIF = 1.002	Fulfilled
3	Standard predicted value: -2.431 to 2.199 Standard residual: -1.773 to 2.825	Fulfilled
4	Acceptable fitting (Figure C. 1 and Figure C. 2)	Fulfilled
5	Values randomly scattered (Figure C. 3)	Fulfilled
6	Residuals randomly scattered around 0 (Figure C. 3)	Fulfilled

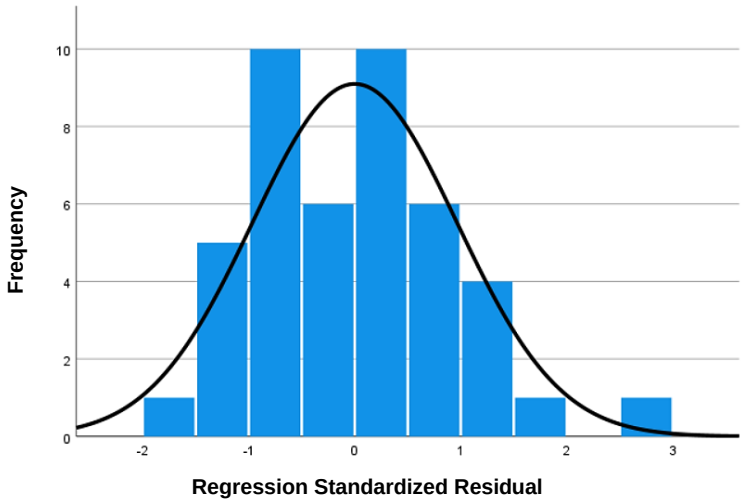


Figure C. 1. Residuals' histogram.

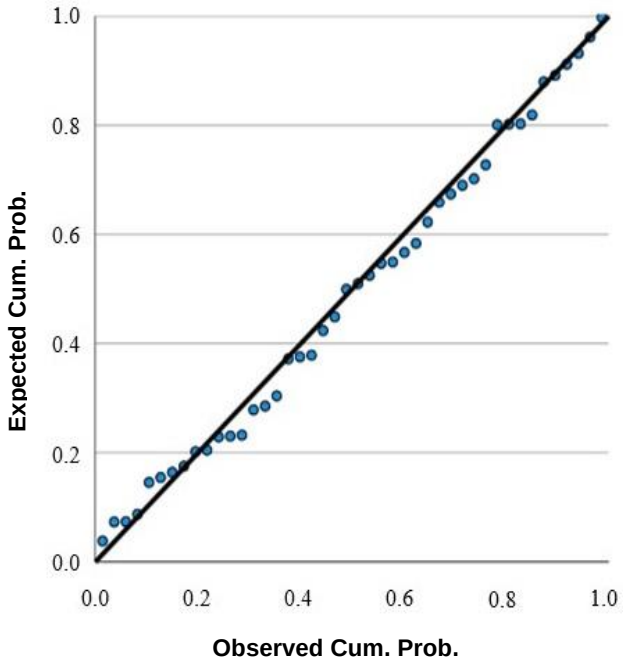


Figure C. 2. Plot of the predicted probability (P-P) for residuals.

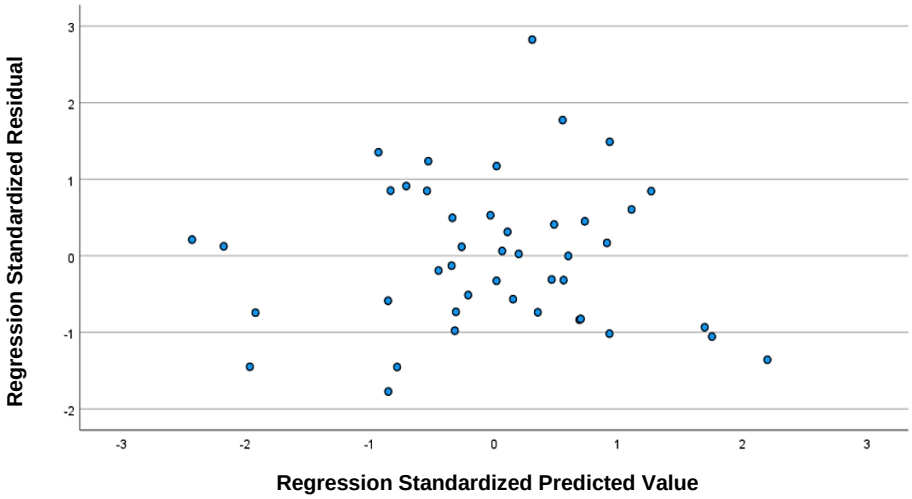


Figure C. 3. Residuals' scattering.